UNIVERSITY OF BERGEN


Department of Physics and Technology

Master thesis in Ocean Technology

Acoustics

---

# Triangulation method for measurement of fisheries echosounder two-way equivalent beam solid angle, $\psi$

---

*Robert Løland*

June 2023

# Acknowledgment

This work in this thesis was conducted as a master project at the University of Bergen (UiB), Faculty of Mathematics and Natural Sciences, Department of Physics and Technology in collaboration with the Norwegian Institute of Marine Research (IMR) and as a part of the CRIMAC project.

I would like to thank my supervisors for the help along the way; Per Lunde (UiB), Audun Oppedal Pedersen (UiB) and Rolf Korneliussen (IMR). I also want to thank the staff members at the Mechanical workshop at the Department of Physics and Technology for machining the parts necessary for this work.

# Abstract

The objective of this thesis is to investigate a method for calibration of the two-way equivalent beam solid angle of scientific echosounders used on the research vessels used by IMR. These echosounders are used to estimate the abundance of fish in in the North-sea and having them be correctly calibrated is important. The echosounder properties obtained during calibration are directly involved in calculating the fish abundance estimations. Meaning any error or inaccuracy in echosounder properties will cause inaccuracies in the final estimation of fish stock.

These estimations of fish stock abundance constitute a key part in national and international regulations regarding marine resources. Fish abundance measurements are based on echo integration and rely on power budget equations and calibrated echosounder systems. These power budget equations involve echosounder properties corresponding to the characteristics of the echosounders being used. These properties include the two-way equivalent beam solid angle, $\psi$, a measure of the directivity of the transducer. The volume backscattering coefficient, $s_v$, used to estimate fish stock abundance is directly, inversely proportional to $\psi$ [1]. Having an accurate value for $\psi$ is therefore of importance.

The current value for the two-way beam solid angle is obtained from the transducer manufacturer [1]. The transducers used in scientific echosounders are all calibrated in a controlled environment, a freshwater pool, by the manufacturer. The characteristics of the transducers, like the beam pattern and $\psi$ are then measured using a hydrophone. These characteristics are recorded in the datasheet for the instrument. This is the value for $\psi$ currently in use when calculating abundance of fish stock. This value might not be accurate when the transducers are mounted on the research vessel. When $\psi$ is measured by the manufacturer the transducer is in free field, meaning it has no baffle. These calibrations are also done in fresh water at different temperatures than IMR operate them in. All these factors will affect the value of $\psi$ when the transducers are baffled on a keel and used in sea water. The severity of the change is not known and is part of why a method for determining the true value for $\psi$ is desired.

Throughout his thesis a methodology for $\psi$-estimation using triangulation with several transducers is proposed and its potential problems discussed, including a sensitivity analysis. Some phenomena observed along the way that may interfere with the estimation are also investigated. The method presented shows promise in its ability to accurately estimate $\psi$ for scientific echosounders.

# Contents

# 1 Introduction

## 1.1 Background and motivation

Echosounder measurements are used in many fields of research and in the industry. The precision required may vary but getting the most accurate results possible is always a goal. Almost all echosounder measurements are indirect, meaning the direct measurements will be used to calculate the desired value via formulae, extrapolations, or other means. Such formulae often include properties of the echosounder such as its directivity or frequency. Knowing these echosounder properties for each transducer to achieve an accurate result is therefore important. This is the purpose of calibration.

Acquiring these parameters are done in many different ways depending on the field in question. Some parameters may be measured on site while others require special equipment or set-ups to measure and are therefore only done occasionally. Many such parameters also change with environmental changes such as temperature and salinity. Other parameters might only be known theoretically, and the validity of its value may be hard to determine. Some parameters used are tabulated or found by the manufacturer of the equipment or part in question.

Developing Reliable ways to calibrate the echosounder parameters under the conditions they are used in will help ensure the accuracy of any estimates calculated using echosounder measurements.

## 1.2 Problem description

This study aims to investigate the possibility of using triangulation methodology to calibrate the two-way equivalent beam solid angle, $\psi$, for scientific echosounders as part of already routine calibrations. Using three of the transducers part of the echosounder on board a research vessel to triangulate the position and target strength of a calibration sphere suspended beneath the vessel, each transducer's beam pattern can be mapped and used to estimate $\psi$. The potential problems and factors playing into the accuracy of the estimations will also be investigated.

## 1.3 Related Work

The background to the power budget equations used to estimate fish stock abundance is described by Lunde *et al* [1]. Finding a target's direction via split-beam phase differential is described by Simmonds & MacLennan [2] its application in fish stock abundance is discussed in [3] and. Using several transducers to triangulate the position of fish was investigated by Skerritt at Newcastle university [4]. The procedures and methodology used in modern echosounder calibrations, which much of this thesis is based on, is described by ICES in their cooperative report [5].

## 1.4 Objectives

This thesis will mainly focus on the work done to develop and implement a method of target location detection via acoustic triangulation in a controlled environment as a basis for further implementation in the field of fisheries acoustics. The triangulation methodology is further used as a basis for transducer beam pattern estimation, which in turn is used to estimate the transducers two-way equivalent beam solid angle $\psi$. The viability and accuracy of the methodology will be discussed as well as potential problems with implementation in the field.

On-ship calibrations of the echosounder systems are done regularly and developing a method for calibrating $\psi$ during these routine calibrations is the aim of this study. This would ensure the validity of the abundance estimations. The accuracy and viability of the method developed will also be investigated. Other challenges and potential difficulties with using such a method are discussed, as several unexpected phenomena occurred during the development of this study.

To do this the beam pattern of the transducers involved needs to be found. This can be done by placing a hydrophone in various positions relative to the transducer, taking measurements and mapping the beam pattern one point at a time. Alternatively, one can use an object with known backscattering properties, placing it in various positions relative to the transducers and using the transducers themselves to record the echo from the object. For this method to work, the position of the object needs to be known at each measurement. Its position can be triangulated using the delay between the sending and the reception of the signals from three transducers. This way a hydrophone does not need to be used, and its position doesn't need to be tracked. With the position of the object relative to the transducers, the beam patterns can be filled in by measuring the strength of the received signal at various angles relative to the transducer in question. By using a heavy metal ball, the strength of the returned signal should be consistent and simple to calculate. By knowing how much sound is expected to backscatter from such a ball, the strength of the signal sent by the transducer can be calculated, and with enough samples from different angles, the beam pattern of the transducer will emerge.

This method has been used by IMR prior [5], however the method of locating the target object was done using the quadrants of a single split-beam transducer for triangulation, as opposed to using several individual transducers. The close proximity of the quadrants may affect the accuracy of the position of the object and therefore may affect the accuracy of the resulting beam pattern.

## 1.5 Outline

Chapter 2 covers the theory behind the work done in this thesis, with focus on the scattering of sound and the method for acoustic triangulation. Chapter 3 presents the experimental set-up, equipment as well as signal detection and positioning methods. In chapter 4 the results of the experiments done are

presented, including directivity, sound speed and system delay measurements. The results from the triangulation experiments with their resulting $\psi$-estimates are also presented here, as well as some other phenomena observed during this study. Chapter 5 contains the discussion of the results and the suggestions for further work. Finally, the appendices include the most important MATLAB-scripts used for acoustic measurements as well as for signal processing and simulations.

# 2 Theory

This chapter will present the necessary theoretical background for the experiments, calculations and simulations in this thesis. Explanations of the various methods, variables and terminology will be included.

## 2.1 Scattering of sound

Acoustic measurements are common in the field of marine research as it provides a reliable method for object detection and identification. The fundamentals of the propagation of sound in water is well understood as well as the scattering of sound from objects. This knowledge makes it possible to decern properties of objects by reflecting sound off them. The reflected sound, or echo, can then be compared to the transmitted sound and the results can tell us about the objects size, shape, material and speed.

Wave scattering occurs when a propagating wave encounters a change in acoustic impedance in the medium it is propagating in. The acoustic impedance is denominated $Z = \rho c$, and is a product of the medium's density and sound speed. Changes in acoustic impedance can happen gradually, like in the water column of the ocean, or instantly like at the boundary layer between water and an object like a fish, the sea floor or a piece of metal.

### 2.1.1 Scattering

The following theory is based on the work done by Clay, C. S. and Medwin [6]. Below is presented an equation describing the scattering of sound from an arbitrary object. The situation described by this equation contains some important assumptions. Both the scattering object and the sound transmitter is in each other's far fields, the sound speed in the medium remains constant and any absorption is disregarded. The incoming wave is a plane wave while the scattered wave will be spherical with its centre at the scattering object.

$$I_s = \frac{I_p}{r^2} S\left(\theta_p, \varphi_p, \theta, \varphi, f\right) A(\theta_p, \varphi_p) \tag{2.1}$$

Where $I_s$ is the acoustic intensity of the scattered wave and $I_p$ is the acoustic intensity of the incident plane wave. $S\left(\theta_p, \varphi_p, \theta, \varphi, f\right)$ denotes a function known as the scattering function and is dimensionless. $S\left(\theta_p, \varphi_p, \theta, \varphi, f\right)$ describes how much intensity is scattered in any given direction $(\theta, \varphi,)$, scatter angle, from an incoming plane wave coming from any given direction $\left(\theta_p, \varphi_p\right)$, incident angle. The amount of reflected intensity also depends on the incident wave's frequency $f$. $A(\theta_p, \varphi_p)$ is a measure of the cross-sectional area of the reflection object as seen from the direction of the

incoming wave. Since the scattered wave is spherical in this scenario, its intensity is dependent on the distance with the relationship $\frac{1}{r^2}$.

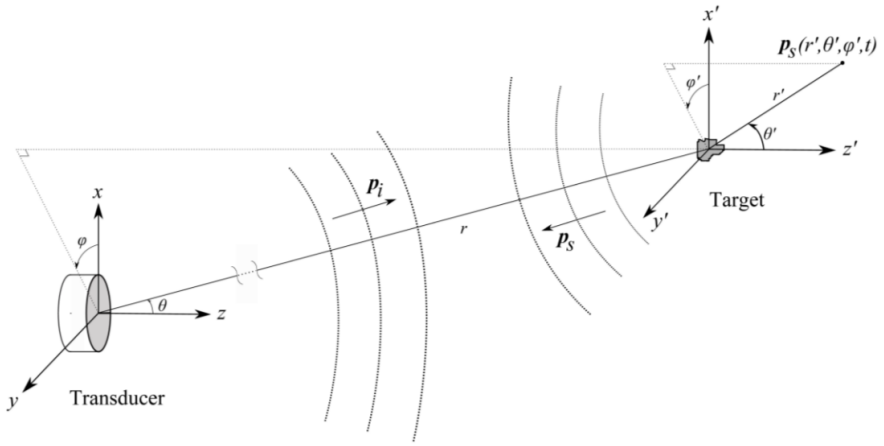


*Figure 2.1: Single target backscattering sketch [1].*

### 2.1.2 Backscattering

When the scattered wave after a scattering incident is scattered back towards the angle of incidence, it is referred to as backscattering. This case is of interest in fisheries acoustics as it makes it possible to transmit and receive a signal at the same location, which is practical. Knowing the properties of the backscattered wave is therefore important. Looking at equation 2.1, a backscattering angle would mean $\theta = \theta_p + 180°$ and $\varphi = \varphi_p$. In this special case a new term is introduced, $\sigma_{bs}$, backscattering cross-section. This is an area describing the ratio between incident and reflected intensity by a given object in the direction of the transmitter.

$$\sigma_{bs} = S_{bs} A = r^2 \frac{I_{bs}}{I_p} \tag{2.2}$$

Where $S_{bs}$ is the dimensionless scattering function given backscattering. The relationship between the intensity of the incident and backscattered wave can then be expressed as

$$I_{bs} = \frac{I_p}{r^2} \sigma_{bs} \tag{2.3}$$

#### *2.1.2.1 Target strength*

In acoustics it is often practical to denote magnitudes in decibels. A decibel equivalent of the backscattering cross-section is therefore defined, known as target strength.

$$TS = 10 \log_{10}\left(\frac{\sigma_{bs}}{A_r}\right) = 10 \log_{10}\left(\frac{I_{bs} r^2}{I_p r_r^2}\right) = 20 \log_{10}\left(\frac{P_{bs} r}{P_p r_r}\right) \tag{2.4}$$

Where $A_r$ is a reference area of 1 m$^2$, making $r_r$ a reference distance and $P = \sqrt{I}$ is the pressure.

#### *2.1.2.2 Volume backscattering*

It is often the case that when measuring backscattering in fisheries acoustics, that not just one target is responsible for the measured echo. As the sound burst transmitted, known as a ping, will cover a volume in the water, within which all targets' echoes may arrive at the same time. The combined intensity is then a measure of the total biomass in that volume [2]. This makes it practical to define a volume backscattering coefficient

$$s_V = \sum \sigma_{bs/V} \tag{2.5}$$

being the sum of the backscattering cross-section of all targets within a volume $V$. Similarly to target strength, volume backscattering can be given in decibels and is referred to as volume backscattering strength [2]

$$S_V = 10 \log_{10} \left( \frac{s_v}{1\ m^{-1}} \right) \tag{2.6}$$

### 2.1.3 Scattering from spheres

In this section the scattering and backscattering of spheres will be discussed. This is especially relevant as IMR and others use spheres as a reference object when calibration echosounders. Knowing the properties of the scattering from spheres is there important.

#### *2.1.3.1 Rigid sphere*

One of the simplest cases of reflection is from a uniform, rigid sphere as it has no internal waves and no absorption of energy. All of the incident wave's intensity is reflected and in predictable directions as the sphere's geometry is simple. The pressure from a scattered wave off a rigid sphere is described by Morse & Ingard [7] and will not be included here.

#### *2.1.3.2 Elastic sphere*

In the real world, no such thing as a rigid sphere exists. Calibrations spheres used in fishery acoustics are often made from hard metals, like tungsten carbide, in order to achieve a rigidity as a high as possible. The effects of their elasticity do nevertheless need to be taken into account when calculating the expected scattering from such spheres.

The assumptions and calculations needed to reach an expression for the backscattering from an elastic sphere has been done by McLennan [8] and involve knowing the frequencies, material properties of the medium and elastic sphere, as well as sphere size being used and will not be recalled here.

### 2.1.4 Power budget equations

The power budget equations are a set of equations used in fisheries acoustics to determine both single target backscattering cross-section and multi-target volume backscattering. Using the values from the measurement of a target as well as echosounder properties found during calibration, the backscattering can be found. The equations are derived by Lunde et al – Fisken & Havet [1].

$$\sigma_{bs} = \frac{16\pi^2 \, r^4 \, e^{4\alpha r} \, \Pi_R}{G^2(\theta, \varphi) \, \lambda^2 \, F_\Pi \, \Pi_T}$$

*2.7*

$$s_v = \frac{32\pi^2 \, r^2 \, e^{4\alpha r} \, \Pi_R}{G_0^2 \, \psi \, \lambda c_0 \, \tau_p \, F_\Pi \, \Pi_T}$$

*2.8*

Where $\alpha$ is the absorption coefficient in the water [Np/m], $\Pi$ denotes the transmitted and received electric power. $F_\Pi$ is the electric impedance factor and $\psi$ is the two-way equivalent beam solid angle. $G_0$ is the on-axis gain while $G$ is the angle dependant gain. $\tau_p$ is the ping time duration.

Using these two equations, the abundance of fish stock can be estimated. It is therefore important that the calibrated parameters that go into the equations are accurate, this includes the value for $\psi$.

## 2.2 Piston model

The directivity of a circular disk transducer, such as the ones used in this study, can be approximated using the piston model. The piston model proposes a plane circular disc as the source of sound. If the disc moves uniformly back and forth, the pressure at any point in front of the disc can be found by dividing the disc into an infinite number of individual sound sources and adding up their contributions. As described by Kinsler & Frey [9], the pressure at any given point in front of is given as.

$$p(r, \theta, t) = j\rho_0 c \frac{U_0}{\lambda} \int_S \frac{1}{r'} e^{j(\omega t - kr')} dS$$

*( 1 )*

Where r is the distance from the centre of the disc to the target point, $\theta$ is the angle between the sound axis z and the vector stretching the distance r and t is the time. $\rho_0$ is the equilibrium density of the medium, c is the sound speed in the medium and $U_0$ is the top speed of the moving disc face. $\lambda$ is the wavelength of the sound, $\omega$ is the angular frequency and k is the wavenumber. S is the surface of the disc and dS is an infinitesimally small area on the disc.

A few assumptions can be made to simplify the equation for our use. We don't care about the absolute value of the pressure, only the relative value compared to the pressure on the sound axis at the same

distance, as long as we are in the far field. Comparing the pressure to the axial pressure also leaves out the time dependency. The resulting pressure is then.

$$|p(r,\theta)| = P_{ax}(r)H(\theta)$$

*2.9*

$$H(\theta) = \left|\frac{2J_1(v)}{v}\right| \qquad v = ka\ sin\theta$$

*2.10*

Where $P_{ax}$ is the axial pressure and $J_1$ is a Bessel function of the first kind, order 1. Since the we only care about the relative pressure, we can divide $p$ by $P_{ax}$ to find the pressure as a function of the angle $\theta$. $p$ would then be equal to $H(\theta)$.

## 2.3 Echosounder calibration

An integral part of the usage of any instrument is the procedure of instrument calibration. No measurement done via an instrument may be trusted unless the instrument has been properly calibrated. This is then also true for echosounders. This section describes some of the theory involved in echosounder calibration as well as methodology.

### 2.3.1 Calibration theory

The calibration of echosounders is described in depth in the research report "Calibration of acoustic instruments" by The International Council for Exploration of the Sea (ICES) [5].

When calibrating echosounders, many variables can be set. For the purposes of this work two are of interest, as they are involved in the power budget equations [10]. These being the gain $G_{0,eff}$, and $\psi$.

#### *2.3.1.1 Gain*

Gain is defined as the acoustic intensity of a transmitter in a given direction divided by the acoustic intensity of a theoretical lossless omnidirectional transmitter.

$$G(\theta,\varphi) = \frac{I(\theta,\varphi)}{I_o} = G_0 B(\theta,\varphi)$$

*2.11*

Where $g_0$ is the gain of the transmitter on the sound axis and $b(\theta,\varphi)$ is the normalized directivity of the transmitter [1]

$$B(\theta,\varphi) = \frac{p(r,\theta,\varphi)}{p(r,0,0)}$$

*2.12*

In calibration, $g_0$ is found by measuring the backscattering cross-section of the calibration sphere and comparing it to the theoretical value of backscattering cross-section for the calibration sphere in question. This is then multiplied by the uncalibrated on axis gain $\hat{G}_0$.

$$G_0 = \hat{G}_0 \sqrt{\frac{\sigma_{bs}}{\sigma_{bs}^t}}$$

*2.13*

#### *2.3.1.2 Two-way equivalent beam solid angle*

The two-way equivalent beam solid angle, $\psi$, is a 3-dimensional angle which is a function of a transducer's beam pattern. The solid angle subtended by an ideal conical beam that would produce the same volume integral as the square of the normalized transducer directivity [5]. This angle will vary greatly as a function of transducer properties. From the piston model, the ka number of the transducer determines the width of the beam solid angle, the effects of which are be presented in section 4.1.

The current value used for $\psi$ in the power budget equations is the value found by the manufacturer of the transmitters via directivity measurements using a hydrophone in a freshwater pool [10]. This is problematic as during calibration transmitter is not baffled, not operating in sea water and at a different temperature than when operating on a research vessel like G.O. Sars. This may change the value of $\psi$, which is why it is of interest to be able to calibrate it on ship.

Finding $\psi$ is a question of integrating over the Normalized directivity of the transducer [2].

$$\psi = \int_0^{\pi} \int_0^{2\pi} b^4(\theta, \varphi)\, sin(\varphi)\, d\theta d\varphi$$

*2.14*

Where $d\Omega$ is a small element of the total solid angle $\Omega$ and $b$ is the beam pattern of the transducer. $\theta$ is the azimuth angle and $\varphi$ is the angle from the sound axis. Knowing the directivity of the transducer can then be used to calculate the two-way equivalent beam solid angle.

### 2.3.2 Calibration sphere method

Using calibration spheres for echosounder calibrations is common and its methodology well described [11]. The spheres used are often made from metals such as copper or tungsten carbide and range in sizes so to be able to accommodate several frequencies and measurement distances. The spheres have resonance frequencies around which their target strengths dip severely [5]. These frequencies vary from sphere material and size and must be avoided as the resulting readings will be affected.

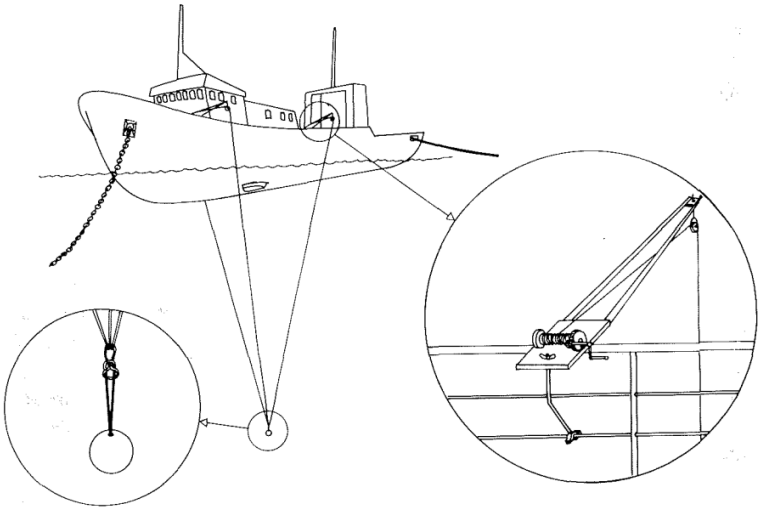

*Figure 2.2: Rigging of research vessel for calibration [11].*

During the calibration procedure, the sphere is suspended by three suspension lines at three different locations on the ship making an inverted tripod, “Three-outrigger method” [5]. The suspension line is often chosen to be thin fishing line as it has a similar acoustic impedance as sea water and will therefore appear as “invisible” to the echosounder as possible, the degree of its “invisibility” is discussed in this thesis. Making sure the sphere and the echosounder are in each other’s far field is important as well as the spheres physical size being small compared to the width of the main lobe of the transducer [5]. The sphere being small compared to the main lobe makes sure the measurement of it target strength is as little affected by covering an area of the beam pattern and not just one point.

The calibration sphere is then moved to different angles in the echosounder beam pattern by either pulling or releasing suspension line, or by its natural sway due to waves and current [5]. The angle to the calibration sphere is found by using a split beam transducer, discussed in section 2.5.1. The target strength of the calibration sphere at various angles from the sound axis can be found. The value can also be found without knowing the spheres location as it will be the highest value recorded, if the sphere location covers the sound axis at high enough resolution. Making sure to compensate for the distance of the sphere as it may change during the calibration procedure.

Using broad band transducers, one more thing has to be taken into account. The sonar equations are frequency dependant and so is the target strength of calibration spheres [5]. Due to the material and size of the calibration spheres, they have resonance frequencies where their target strength drop significantly. Several spheres then may be used to cover a wide band of frequencies to avoid any minimums in target strength as the spheres can cover different parts of the band that don’t contain TS-minimums.

If one then compares the target strengths of the calibration sphere with the theoretically expected value from such a sphere, $G_0$ can be found via equation 2.13.

## 2.4 Beam solid angle $\psi$

### 2.4.1 Estimating Psi

The true value of $\psi$ can only be measured if the entire beam pattern of the transducer is mapped. However, this is challenging and time consuming. Therefore, it is desired to know how much of the beam pattern needs to be mapped before an estimate for the beam pattern can be determined. Assuming the beam pattern is measured from the sound axis and out in all directions, how many degrees, or equivalently, how many decibel drop in intensity needs to be mapped to reach a desired level of accuracy.

In section 4.1, is presented the results of the calculations done to find an estimation for $\psi$ at different degrees of precision. The model used to calculate the beam patterns is the piston model, presented in section 2.2. These calculations give an idea of how wide the beam pattern of each echosounder transducers needs to be mapped in order to get a good estimation of the beam solid angle. The piston model is, of course, an estimation and is used here to give perspective and explain the concepts behind $\psi$ and the measurement of it. As well as giving an idea of the needed width of measurements that might be required. For more accurate results the measured beam patterns for the transducer may be used to find a better estimation of the required beam pattern mapping.

## 2.5 Triangulation

It is possible to find the location of an object, the target, by knowing it distance from other objects with knows positions, hereby referred to as locators. Doing this is known as triangulation and is used in technologies such as GPS to locate places or personnel on earth using several satellites. If the distances from four or more such locators to a target is known, the position of the target can be known precisely. If only three objects are used, then the location of the target can only be known to be either one of two locations in space, mirrored over the plane defined by the three locators. Finding these two locations involves solving the equations

$$(x - x_1)^2 + (y - y_1)^2 + (z - z_1)^2 = d_1^2 \tag{2.15}$$

$$(x - x_2)^2 + (y - y_2)^2 + (z - z_2)^2 = d_2^2 \tag{2.16}$$

$$(x - x_3)^2 + (y - y_3)^2 + (z - z_3)^2 = d_3^2 \tag{2.17}$$

where $x$, $y$ and $z$ are the coordinates of the target while $x$, $y$ and $z$ with subscripts are the coordinates of the three locators. $d$ denotes the distances from each known object to the target object. A physical interpretation of these equations is imagining a sphere of radius $d$ being located with its centre at each of the corresponding locators. Meaning a sphere of radius $d_1$ is located at coordinates $(x_1, y_1, z_1)$ and so on. These three spheres will intersect at two points in space. These points correspond to the solutions to the set of equations.

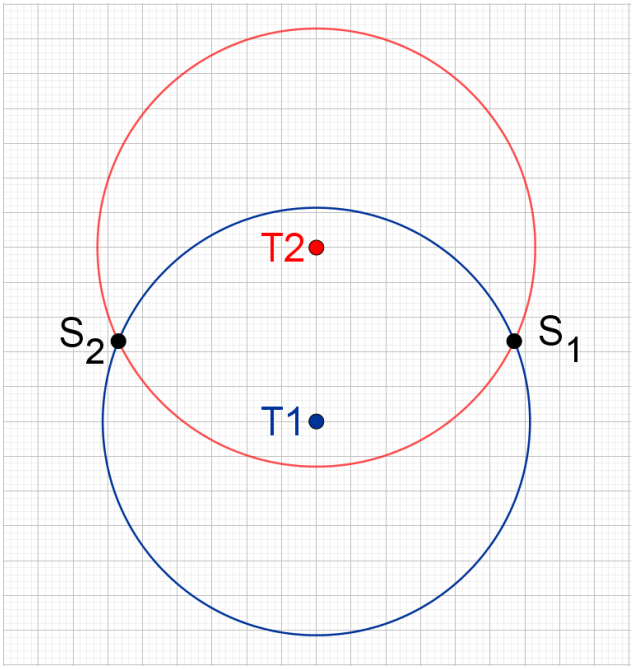


*Figure 2.3: 2D triangulation example showing the two possible answers.*

Figure 2.3 shows an example of triangulation in 2D-space. Intersections of the circles centred at the points T1 and T2, are the solutions to the set of 2 triangulation equations. The points labelled S are the solutions to these triangulation equations.

When in 3d-space the solutions to these equations give two points where the target can be located. It may be possible to rule out one of these solutions depending on the situation, making triangulation with just three objects and not four, a viable option. This is possible in the case studied in this thesis. The plane defined by the three transducers in use for the triangulation calculations, both on ship and in the tank experiment, make it so that the two solutions to the equations equate to one point in front of the plane and one behind. In all cases the direction of the target relative to the transducer plane is known and ruling out the other solution is possible. In the case of measurements on ship, one of the solutions would project the target to be above sea level, which is known to be false.

Solving these equations involve either simplifications or using a solving tool such as MATLAB, or both. To simplify the equations, some assumptions can be made. Since the positions of the locators are known and therefore only the position of the target relative to the transducers is desired, the

coordinate system can be chosen as seen fit. If the origin point of this new coordinate system is chosen to be at locator 1, and all three locators define the z-plane, the equations are simplified. These simplifications give the new locator coordinates

$$L_1 = (0,0,0), L_2 = (x_1, y_1, 0), L_3 = (x_3, y_3, 0)$$

*2.18*

Which reduces the set of equations to:

$$x^2 + y^2 + z^2 = d_1^2$$

*2.19*

$$(x - x_2)^2 + (y - y_2)^2 + z^2 = d_2^2$$

*2.20*

$$(x - x_3)^2 + (y - y_3)^2 + z^2 = d_3^2$$

*2.21*

Solving this set of equations gives symbolic expressions for the solution to the coordinates of the target $(x, y, z)$ and can be written as

$$x = \frac{x_2^2 y_3 - x_3^2 y_2 + y_2^2 y_3 - y_2 y_3^2 - y_2 d_1^2 + y_2 d_3^2 + y_3 d_1^2 - y_3 d_2^2}{2(x_2 y_3 - x_3 y_2)}$$

*2.22*

$$y = \frac{x_2 x_3^2 - x_2^2 x_3 + x_2 y_3^2 + x_2 d_1^2 - x_2 d_3^2 - x_3 y_2^2 - x_3 d_1^2 + x_3 d_2^2}{2(x_2 y_3 - x_3 y_2)}$$

*2.23*

$$z = \pm\sqrt{d_1^2 - x^2 - y^2}$$

*2.24*

These simplifications might not always be needed. As is the case on research vessels like G.O. Sars, the positions of the transducers on board are already defined through the ships coordinate system, as can be seen in Figure 2.4. As one can calculate the target coordinates in any coordinate system by using the set of simplified equations without the need for any coordinate system change. Although simplifying the equations this way might be beneficial in regard to computation time, as doing them reduces the size of the expressions for the target coordinates significantly. The symbolic expressions for the solutions to these equation without any simplification, as they stand in equations 2.15 - 2.17, is so expansive it will not be presented here. These six symbolic expressions, two sets of three coordinates, may be calculated exactly using the MATLAB-script in appendix A.5.

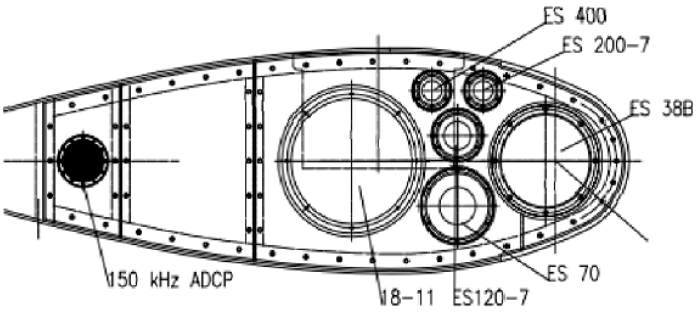


| PTS DROP KEEL | | | |
|---|---|---|---|
| POINT | X | Y | Z |
| ES 38B | 8,579 | -0,473 | 6,169 |
| ES 200-7 | 8,331 | -0,740 | 6,172 |
| ES 400 | 8,144 | -0,799 | 6,174 |
| ES 120-7 | 8,177 | -0,578 | 6,176 |
| ES 70 | 8,179 | -0,275 | 6,182 |
| 18-11 | 7,703 | -0,472 | 6,190 |
| 150 KHZ ADCP | 6,546 | -0,467 | 6,220 |

*Figure 2.4: Discontinued echosounder set-up on G.O. Sars with coordinates for the transducers [12].*

The same principle applies when the distance is measured acoustically, with for instance transducers. By sending a sound signal at a scattering object and recording the time delay before receiving the echo, the distance to the object can be known if the sound speed in the medium is known. From there the equations presented above can be used to find the location of the target.

### 2.5.1 Split beam triangulation

Split-beam transducers are split into quadrants which can detect signals separately. This can be used to calculate a targets direction by comparing the phase differences of the returning signal on the four sections of the transducer [2]. This is currently how the beam pattern of scientific echosounder at IMR are measured, by using split-beam transducers to find the angle to the target and plotting the measured target strength at that angle [5].

Knowing the propagation time then also gives the distance to the target from each quadrant, which can be used in equations 2.15 - 2.17 to determine the targets exact position in space. A problem with this approach is the potential inaccuracy from having the locators' placed so close together. The effects of the distance between locators is explored in section 4.6.1.2.1.

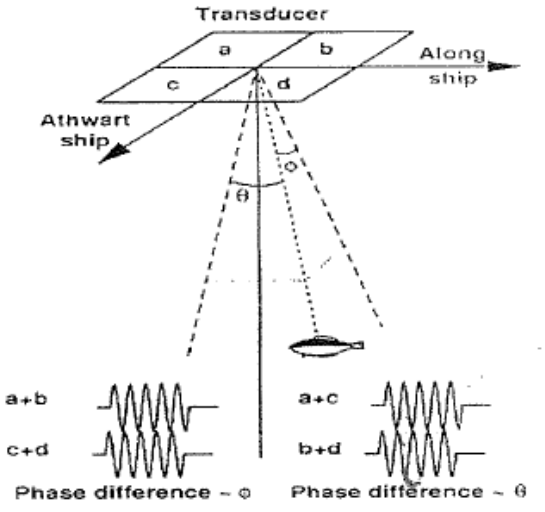


*Figure 2.5: Principles of a split-beam echosounder [2]*

# 3 Experimental set-up and methods

This section described the experimental set-up and methodologies used during this study. The Experiment tank and its functionality is presented, a list of equipment is given in Table 3.1, the algorithms used in the signal processing is described, as well as the methods for detecting transducer positioning in the tank and the signal amplitude measurement method.

## 3.1 Laboratory

All experiments performed in this study were conducted at the acoustics laboratory at The Department of Physics and Technology at UiB.

### 3.1.1 Experimental tank set-up

The laboratory has a tank of water designed for acoustic experiments. The tank has an internal length of 4 meters while it has a height and width of 1 meter with an open top, containing about 4000 litres of fresh water. A panoramic view of the tank is shown in Figure 3.1. All axis directions in this study will is based on the axis defined on the experiment tank. Figure 3.2 shows the defined axis-directions. The defined directions are, the X-direction is down into the water column, Y is parallel with the shorter end walls of the tank and Z in parallel with the longer side walls of the tank. These directions will be referred to throughout the thesis and were chosen to emulate the directions on board research vessels, were z is the direction of transducer transmission.

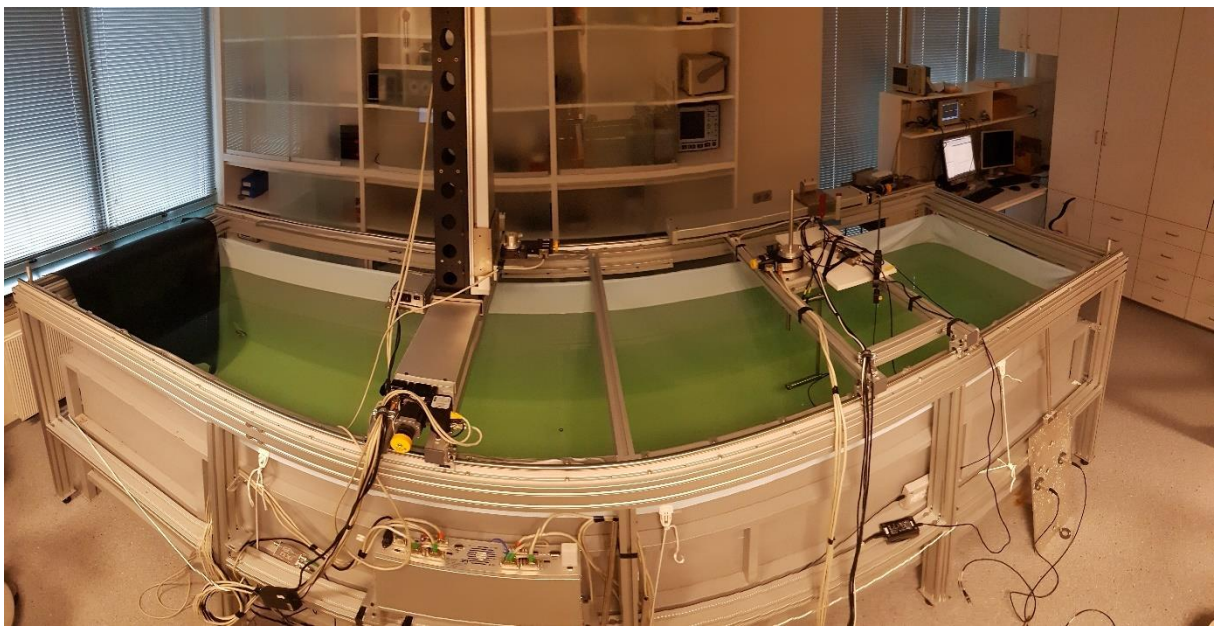

*Figure 3.1: Panoramic view of the experiment tank and its translation system.*

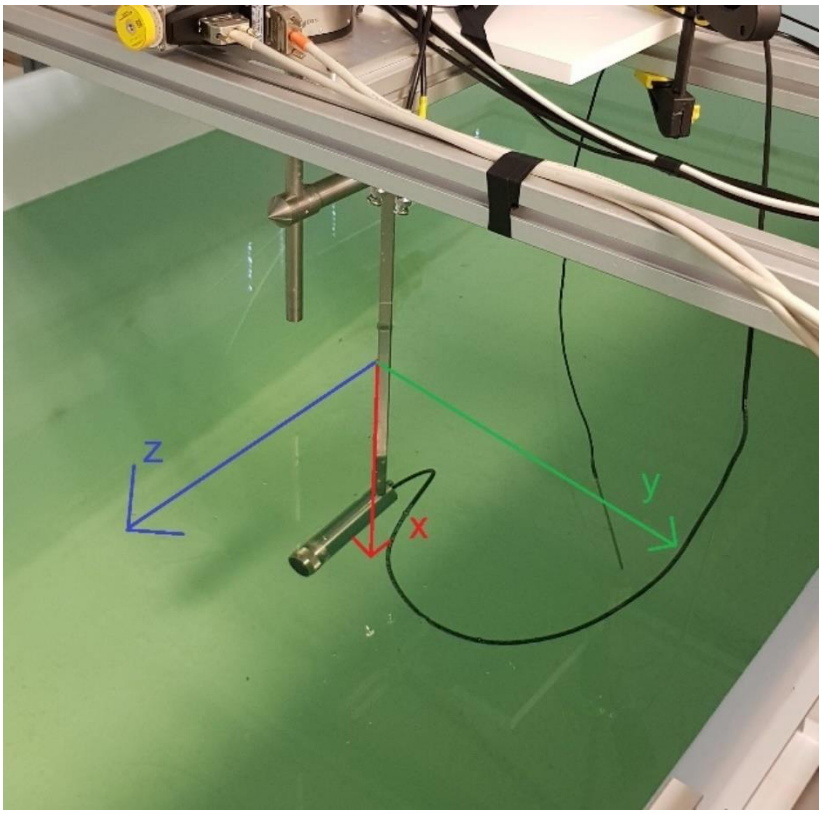


*Figure 3.2: x, y and z-directions defined in the tank.*

#### *3.1.1.1 Translation system*

The experiment tank is fitted with a precise translation system that is capable of holding, moving and rotating objects above or inside the tank. The system has several parts making for the different movements. Figure 3.3 presents the parts as viewed from above the tank and each part is explained below.

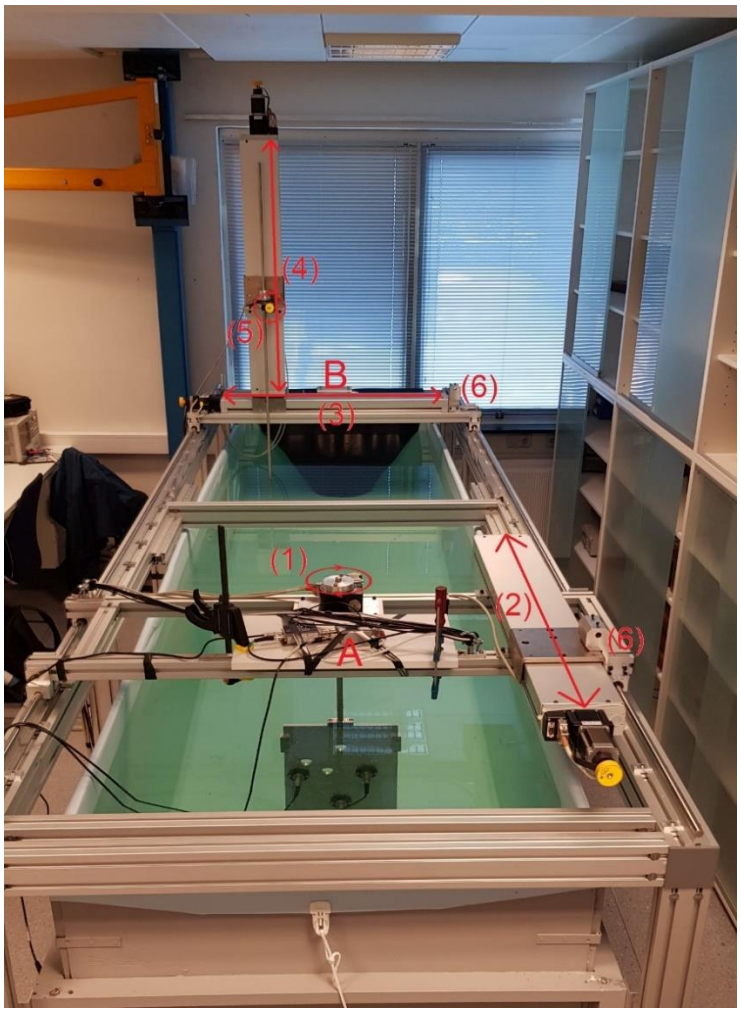


*Figure 3.3: The tank's translation system.*

The translation system is mounted on two gantries, referred to as "stages", labelled A and B in Figure 3.3. These stages are mounted to railings which are attached to the metal "skeleton" surrounding the tank, making it possible for them to easily slide up and down the length of the tank. This makes it possible to adjust the distance between any to objects mounted to the stages. All parts of the translation system is controlled by the user on the PC via MATLAB and all current positions of all assemblies is known.

The numbered labels on Figure 3.3 are explained here:

(1) Refers to the stage A's rotation system, controlled by a stepper motor which can rotate an object mounted through its 16 mm diameter mounting hole. In Figure 3.3, a transducer mounting plate is seen mounted to the assembly and could be rotated about the x-axis. The direction and amount of rotation is controlled by the user and the current absolute position of rotation is known and has a range of [0, 360°]

(2) Is a stepper motor-controlled translation assembly, in the Z-direction of the tank and has a range of 800 mm. By mounting a metal rod in both the mounts labelled (6), the two stages A

and B are now connected and the distance between them can be changed by moving the assembly. Moving the assembly 400 mm results in a change in distance between the two stages of 400 mm. When such translation is performed, one of the stages is fastened to the railing such that only one of the stages moves when the translation assembly is being used.

(3) Is stage B's translation assembly in the tanks y-direction. Similarly, to (2) this assembly is controlled by a stepper motor and has a range of 800 mm and can move an attached object in the tank's y-direction.

(4) On top of assembly (3) is mounted a translation assembly in the x-direction, for moving objects through the water column. The range of movement is 800 mm.

(5) Mounted to assembly (4) is stage B's rotation assembly, letting the user control the rotation of the mounted object about the x-axis in the range [0, 360°].

(6) Are the mounting points for a metal rod used when translating one of the stages in the z-direction.

Through these assemblies, controlled relative movement in space between two objects is possible, as well as rotation about the x-axis. This is the basis for all movement done in the experiment tank in this thesis and all positions will be expressed in the coordinate system defined by the tanks translation system, unless otherwise specified. Meaning assembly (3) defines the y-axis and its dimensions. Same principle applies for assembly (2) & (4), making the possible positions for the object mounted to stage B

$$x = [0, 0.8], \qquad y = [0, 0.8], \qquad z = [0, 0.8].$$

With this set-up it is possible to mount a transmitter, such as a transducer, and a target, such as a hydrophone or calibration sphere, to each of the two stages in the tank. The current position of any given stepper motor is known at any given time. Making it possible to know the position of the target with high precision. The current angle of the transducer is also known. The directivity of the transducers used can then be found, as well as determining the sound speed in the medium and verifying the accuracy of the triangulation calculations.

#### *3.1.1.2 Acoustic measurement set-up*

While doing experiments in the tank either of two acoustic measurement set-ups were in use. Either the target was a hydrophone or a calibrations sphere making it necessary to adjust the setup accordingly. For both set-ups, the signal generator sends a burst to both the transducer for transmission and the oscilloscope for comparing with the received signal during cross-correlation. The transmitted signal from the transducer is then either picked up by a hydrophone or scattered off a calibration sphere and then received by the transducer again. In both cases the received signal is sent

to an analogue filter to improve the signal to noise ratio before arriving at the oscilloscope for observation. Any information gather via the oscilloscope can be saved to the PC via ethernet. The signal generator can also be controlled from the PC or manually.

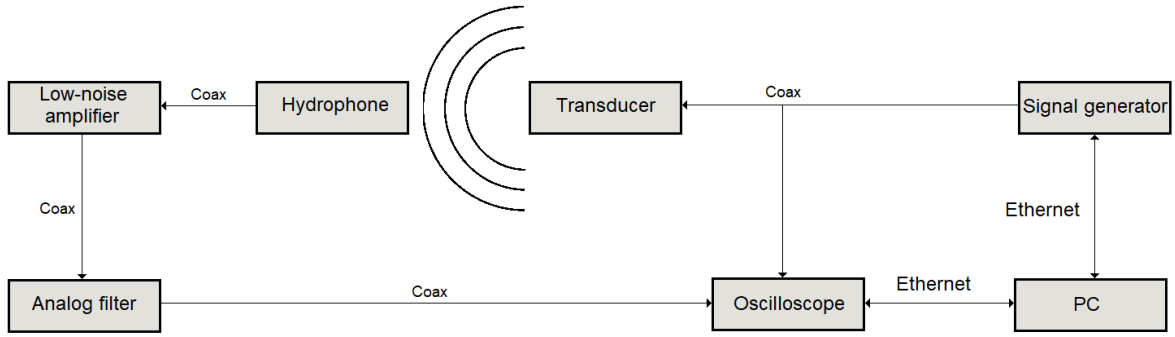


*Figure 3.4: Acoustic measurement set-up for hydrophone experiments.*

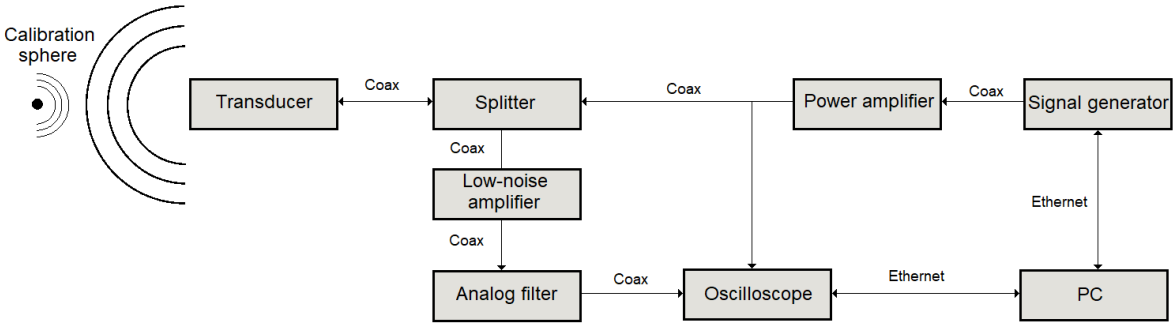


*Figure 3.5: Acoustic measurement set-up for calibration sphere experiments.*

As can be seen in Figure 3.5, the calibration sphere setup uses a component labelled “splitter”, this in an in-house component built to be ample to both send and receive signals from a transducer with the help of diodes. The splitter and its circuit-schematic can be seen in Figure 3.6. The low-noise amplifier used to amplify the signal before reaching the analogue filter is shown in Figure 3.7.

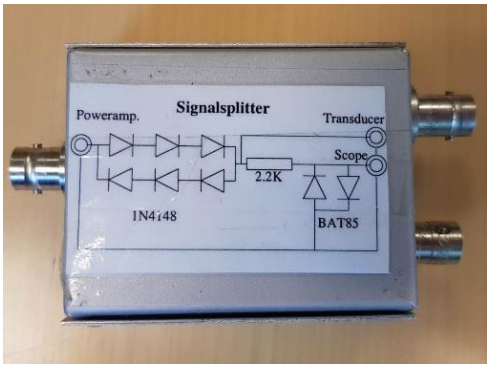


*Figure 3.6: Signal splitter.*

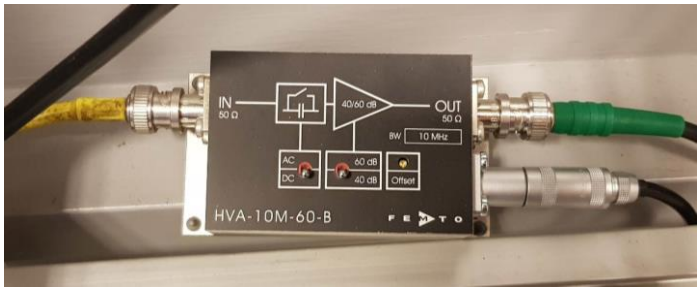


*Figure 3.7: Low-noise amplifier.*

#### 3.1.1.2.1 Amplification

Before reaching the oscilloscope, the received signal gets amplified by several different sources, including the analogue filter and low-noise amplifier. The exact amount of amplification will not be kept track of for the purpose of this study as all signal amplitudes will only be compared to the other signal amplitudes measured using the same setup, meaning the amount of amplification cancels out, meaning all amplitude comparison in this study are relative and not absolute.

During the hydrophone tests, a 10 V peak-to-peak signal was transmitted by the signal generator. The power amplifier was used during the calibration sphere setup to increase signal to noise ratio as the echo received from certain angles was too weak to discern from the background noise without amplifying the input signal to the transducer. A 222 mV signal was then amplified to 92 V peak-to-peak signal before reaching the transducer.

Checking for non-linear effects during this setup reveals no issues. The signal shown in Figure 3.8 is the received echo from a calibration sphere at 2 meters with a 92 V peak-to-peak input signal on the transducer. The echo shows no signs of non-linear effects as its shape is almost identical to a sine wave with the same amplitude and frequency.

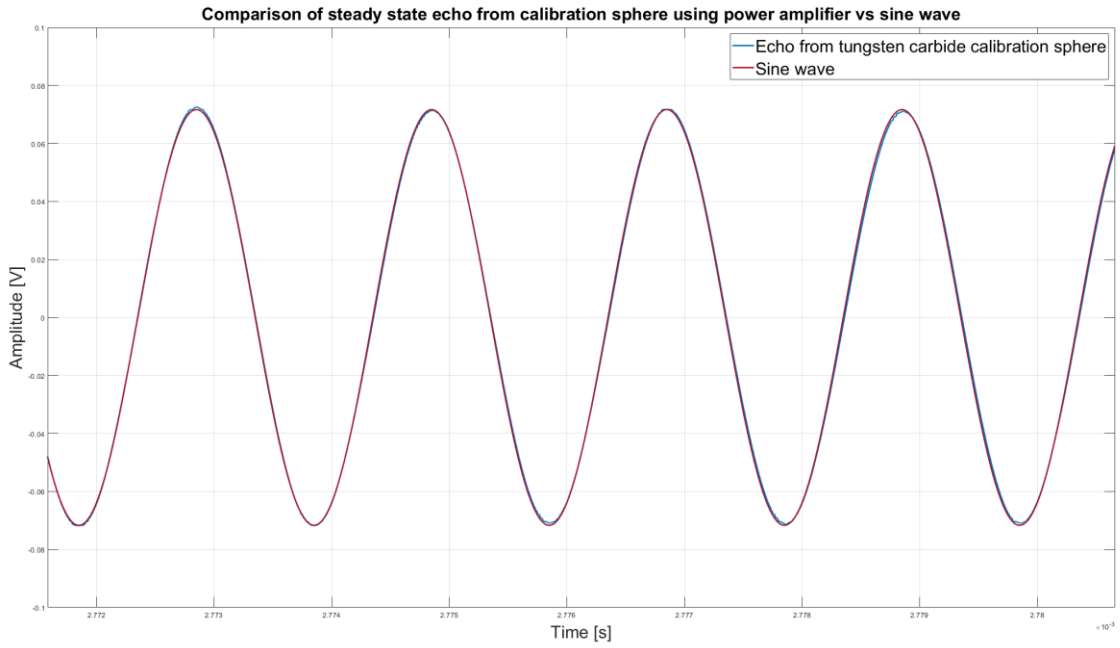


*Figure 3.8: Echo from calibration sphere when using power amplifier compared to a sine wave with the same amplitude and frequency showing no non-linear effects.*

## 3.2 Equipment

The list of equipment used for the experiments done in this thesis is given in the table below:

| Brand/name | Equipment type | Serial number |
|---|---|---|
| Tektronix TBS 2000B | Digital oscilloscope | C020387 |
| KROHN-HITE MODEL 3940 | Analogue filter | S.N:LR2721R |
| | Signal generator | MY59001919 |
| 22 mm Tungsten carbide sphere | Calibration Sphere | IMR 070 |
| 20 mm Steel sphere | Calibration Sphere | - |
| 16 mm Copper sphere | Calibration Sphere | - |
| Olympus V301-SU 25mm | 500 kHz Transducer α | 654055 |
| Olympus V301-SU 25mm | 500 kHz Transducer β | 654220 |
| Olympus V301-SU 25mm | 500 kHz Transducer γ | 1380089 |
| Olympus V302-SU 25mm | 1 MHz transducer | 653462 |
| Precision acoustics | Ultrasonic Hydrophone | 2705 |
| SMC-hydro | Translation system | 7160-9-605 |
| Electronics and innovation 2100L | RF Power amplifier | 1048 |
| Femto HVA-10M-60-B | Low-noise amplifier | 05-03-340 |
| Pico PT104 data logger | Data logger | JY892/154 |
| Pico SE012 | PT100 resistance thermometer | - |

*Table 3.1: Equipment*

*Figure 3.9: The three calibration spheres used, 22 mm tungsten carbide (left), 16 mm copper (centre) & 20 mm steel (right).*

*Figure 3.10: The four transducers used in this study, 500 kHz (left) & 1 MHz (right), all with a 25mm face diameter.*

### 3.2.1 Machined parts

Before and during the experiment stage it was realized that it would be desirable to have parts produced to help in the experiment process. Some of these pieces were planned out before any experiments were conducted, while some were found to be useful while doing testing and were commissioned then. The work in this study was done at the UiB Department of Physics and Technology, where there is a machining workshop where parts needed by employees or students at the faculty can be commissioned and made quickly and to specifications. All the parts discussed in this segment were produced in this workshop.

#### *3.2.1.1 Transducer mounting plate*

In order to mimic the relative placements of the transducers used by the Institute of Marine Research on the research ship G.O. Sars, a mounting plate was needed. Firstly, the positions of the transducers composing the echosounder were acquired from IMR and their positions relative to each other found. The exact positions of the transducers were known for an earlier transducer configuration on the keel, no longer in place on G.O. Sars, but the current set-up's transducer positions were not acquired, but some of the transducers on the keel are still positioned as they were and since the distances between them stayed the same, they could therefore be known by the schematics for the previously used set-up. The rest of the transducers' positions could then be found by using an updated image of the current set-up configurations and measured the distances between them using an image editing software, shown in **Feil! Fant ikke referansekilden.**. The number of pixels could then be multiplied by the ratio

between the known distance between two unmoved transducers and the number of pixels over that known distance. The bottom part of the Figure shows the old configuration with the old coordinates for each transducer, while the top shows the new configuration with the measured distances.

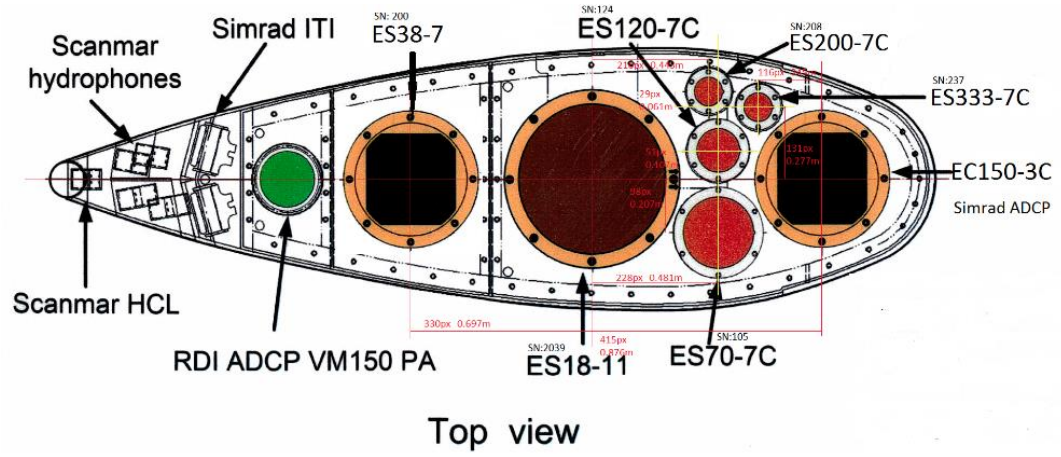


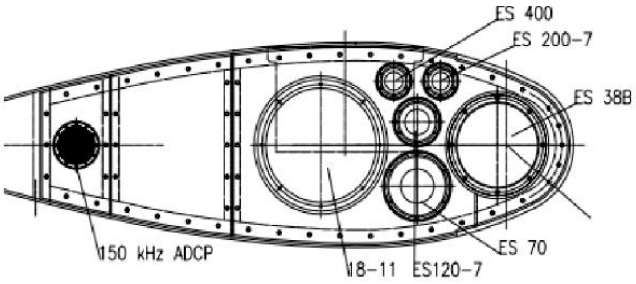


| PTS DROP KEEL | | | |
|---|---|---|---|
| POINT | X | Y | Z |
| ES 38B | 8,579 | -0,473 | 6,169 |
| ES 200-7 | 8,331 | -0,740 | 6,172 |
| ES 400 | 8,144 | -0,799 | 6,174 |
| ES 120-7 | 8,177 | -0,578 | 6,176 |
| ES 70 | 8,179 | -0,275 | 6,182 |
| 18-11 | 7,703 | -0,472 | 6,190 |
| 150 KHZ ADCP | 6,546 | -0,467 | 6,220 |

*Figure 3.11: New and old schematic of transducer set-up on keel on G.O. Sars [12].*

*Figure 3.12: Transducer mounting plate.*

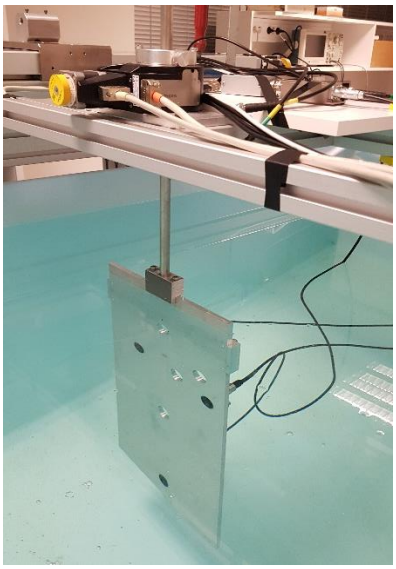

*Figure 3.13: Transducer mounting plate during experimentation.*

When the positions were found, a cad model of the mounting plate was designed. It was decided that the plate would be made of aluminium and be 1 cm thick and contain the seven holes necessary to emulate all combinations of transducers possible on G.O. Sars. For the experiment tank set-up to be able to hold the plate underwater, the plate needed a rod of diameter 1.6 cm so that it could be secured to the rotation motor mounted on one of the stages through its mounting hole.

The transducers then needed to be secured in their mounting holes without interfering with the signal and still be flush with the plate surface. This was achieved by taking advantage of the existing lip present on all the transducers being used in the experimenting. A schematic is shown in Figure 3.14: Transducer mounting cross-section and pictures of the mounting hole is shown in Figure 3.15. All the transducers used has a lip giving the transducer a larger diameter at certain heights, making it possible to cut a hole through the plate in the desired location with the smallest diameter of the transducer as well as a larger diameter hole going about halfway through the plate. The transducers would then fit in the hole, including the lip, while sitting flush with the plate on the front of the transducer. On the back of the plate a plastic ring with an identical hole shape to the mounting hole in the plate was placed around the back of the transducer enclosing the lip and keeping the transducer from moving. This plastic piece will then be able to be fastened to the plate securing the transducer by screwing some bolts through the plastic ring and into the plate.

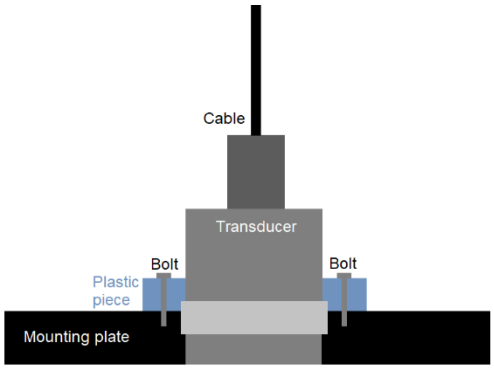


*Figure 3.14: Transducer mounting cross-section.*

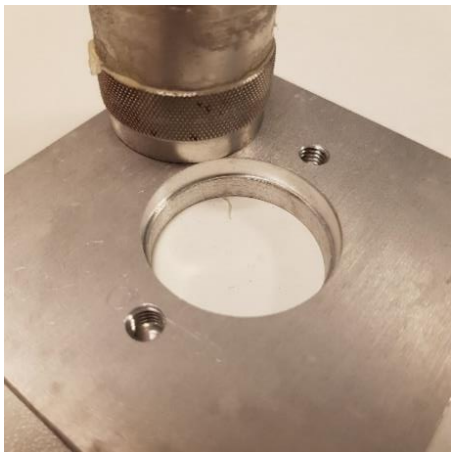

*Figure 3.15: Transducer mounting hole close-up.*

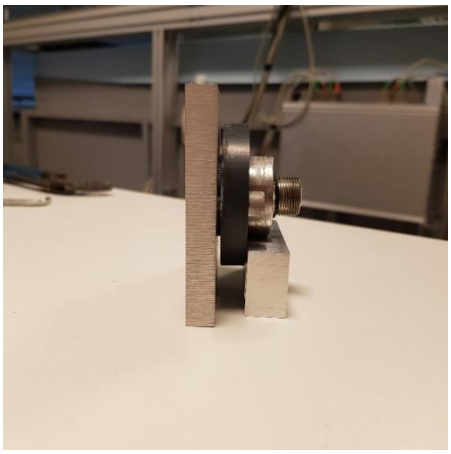

*Figure 3.16: Mounted transducer side-view.*

### *3.2.1.2 Free field transducer mount*

In order to test a transducer in controlled conditions, it needs to be placed in a free field with no baffle and no object close which can interfere with its signals. This is especially important when the directivity of a transducer is measured. To do this a mount which can hold a transducer without any of its parts being in front of, next to or even close to the face of the transducers was needed. One of these mounts already existed in the laboratory and had already been machined at the workshop, this could then be copied and machined again. It is very important that the rod that is mounted to the rotation motor points straight at and is parallel to the face of the transducer such that the position of the centre of the transducer face does not move as the whole mount is rotated while doing experiments. This is to prevent the distances from the transducer and the target to change during directivity measurements which relies on the amplitude of the signal, which changes as a function of distance. Other precautions were also taken to reduce interference, such as shaping the vertical rod as a right angle as opposed to being circular in order to reflect sound away more effectively.

*Figure 3.17: Free field transducer mount.*

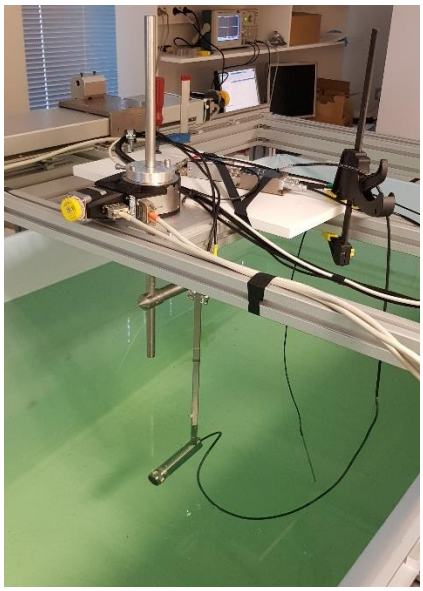

*Figure 3.18: Free field transducer mount during experimentation.*

### *3.2.1.3 Baffles*

To investigate the effects of bafflement on transducer directivity it was desirable to have a controlled way to measure the directivity pattern with and without a baffle. Three baffles designed in the same way as the mounting plate, were made in different sizes. All the baffles are square plates of aluminium with a transducer fastened to and flush with the plate. The sizes of the plates produced were 8, 12 and 30 cm along each side. The fastening mechanism is the same as shown in Figure 3.14. The baffle can then be mounted around a transducer which can then be mounted on the free field mount. The same directivity measurements can then be done with and without a baffle. The 8 cm baffle was later scrapped and not used in experimentation.

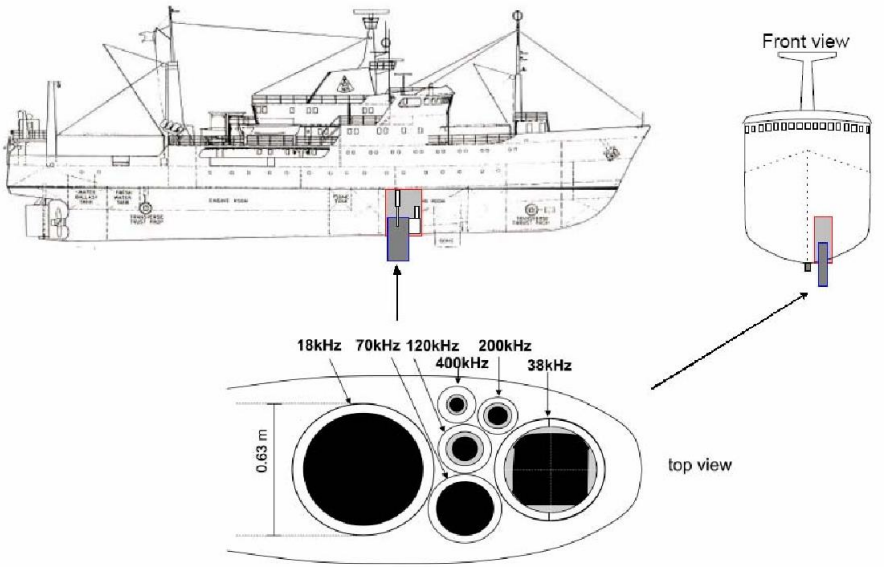


*Figure 3.19: Transducer mounting on the drop keel of research vessel G.O.Sars [13].*

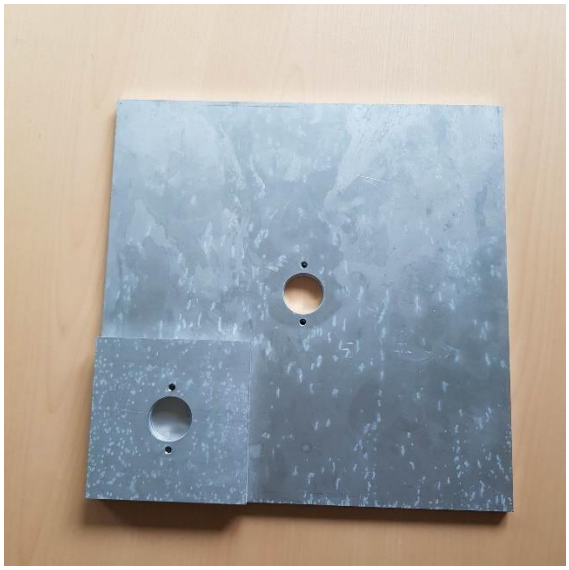

*Figure 3.20: The two machined baffles.*

### *3.2.1.4 Echo dampening rubber panels*

When performing measurements using a calibration sphere at larger angles relative to the sound axis of the transducer, the echo received may be so weak that it cannot be discerned from the background noise. In order to increase the signal to noise ratio, a higher voltage input can be applied to the transducer, producing higher amplitude waves, making the echo also stronger. An unwanted side effect of this is that the echoes coming from the walls of the tank will now last much longer, meaning the time between bursts needs to be extended so that echoes from previous burst have time to die out and not interfere with the current measurement. Under conditions where these old echoes die away quickly, a burst delay of around 10 ms can be used. Not all echoes will have disappeared by then, but it will be possible to find timespans of silence between these old echoes, making it possible to do

accurate measurements without wall echo interference at a high burst frequency. It is desirable to have a low time delay between signal bursts, as while averaging over many such bursts may take a long time if this delay is long. Taking the average of 512 samples for instance, with a 100 ms time delay between bursts would take, at least 51.2 seconds to perform and needs to be done many times in order to remove as much noise as possible during all measurements. Having to wait up to 100 ms in order to find a quiet enough span of time free from “rogue” echoes so that a new burst can be sent, and then averaging over 512 bursts and doing this at 1000 different positions takes a long time. Cutting down on the time delay between burst is therefore important, so that more experiments can be done in a reasonable timeframe. The solution to this problem was to dampen the echoes coming from the walls of the tank. This has been done on one of the smaller tanks in the laboratory by hanging panels of rubber over the walls that are normal to the sound axis. This was also done on the larger tank. Reduction in echo duration was substantial, and the delay could now be set much lower, saving time and generally improving signal to noise ratio for all measurements in the tank.

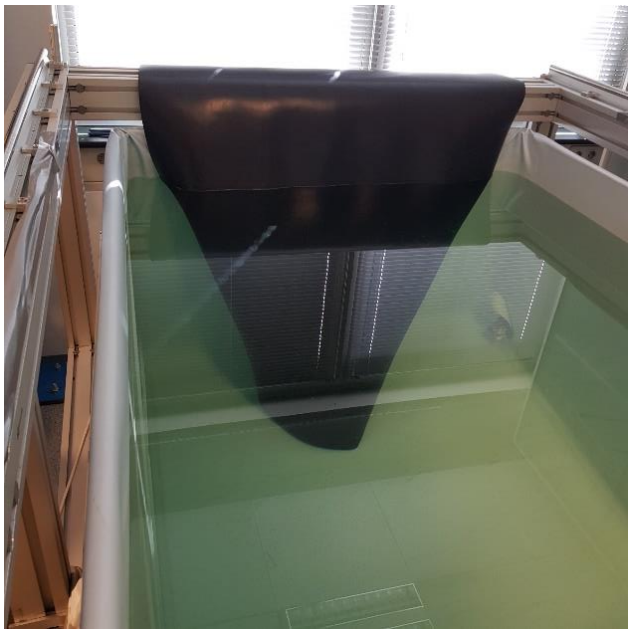

*Figure 3.21: Rubber panel for echo dampening in tank.*

## 3.3 Experiments, measurements and methodology

This section presents the methods used for signal detection, amplitude determination and other general methods and settings used when performing experiments in this study.

### 3.3.1 Signal Detection Method

Several methods for signal detection were used during this study, for signal arrival detection as well as signal amplitude measurements. This section presents and describes the methods used and their advantages and disadvantages.

#### *3.3.1.1 Cursor method*

The cursor method involves using the built-in cursors functionality on the oscilloscope and manually selecting a time window where one thinks the steady state of the signal starts and ends. This method gives a lot of freedom to choose what counts as the signal, making the user the signal detection algorithm. It is also therefore very subjective and detecting the same point on two different signals will be virtually impossible. This method was primarily used when doing directivity measurments as the distance form transducer to target, and therefore arrival time of the received signal did not change throughout the experiment, making the cursor method viable.

Using the cursors to detect a signal with an arbitrary arrival time however cannot be done with this method. If the distance from transmitter to receiver is not known, a different method needs to be used.

#### *3.3.1.2 Threshold method*

Using an amplitude threshold to detect a signal can be a simple and consistent method of detecting both the beginning of a signal and its stable part. Detecting the start of a signal this way was done by finding the maximum amplitude of the signal and then finding the first instance where the received voltage exceeds a certain percentage of the maximum voltage. The chose percentage varies from case to case to avoid noise breaching the threshold. This method is simple and easy to implement but works best at high signal to noise ratios as it is not very robust.

#### *3.3.1.3 Envelope method*

This method is similar to the threshold method but instead of using the raw voltage measured, one can use the envelope of the voltage. The envelope function of the signal will behave more regularly even at lower signal to noise ratios, making it easier to detect the signal of interest. Using the same principle as the threshold method but using the envelope as the detection function instead gives better results, especially at detecting the end of the signal which the threshold method was poor at. The envelope of a function was be found using MATLAB's built-in envelope function. The function can take

in parameters such as the length of the Hilbert filter used which will alter the envelope. These parameters were changed depending on the experiment conditions.

The envelope detection MATLAB-script is available in appendix A.6.

#### *3.3.1.4 Cross-correlation Method*

Using the correlation between the transmitted signal and the received signal is a consistent method for detecting the start and end of a signal. The received signal is cross correlated with the signal transmitted by the signal generator to the transducer, giving a cross-correlation function. The maximum value of which corresponds to the largest overlay of the two signal. This timestamp was selected as the start of the received signal. The same can be done to find the end of the signal by comparing the reversed received signal with the transmitted one.

The cross-correlation detection MATLAB-script is available in appendix A.2.

### 3.3.2 Finding transducer positions in experiment tank

In order to verify the results from the triangulation experiments as well as knowing the sound measurement experiment is valid, one needs to be able to know the location of one or more of the transducers used in the experiment. The mounting plate that hosts the transducers does have known measurements between mounting holes, but the angle of the plate in the x, y and z directions are unknown during experimentation. It is therefore useful to be able to find the exact positions of all transducers via a different method.

The chosen method involves measuring the delays between signal sending and reception by a hydrophone or reception of the echo from a calibration sphere by the sending transducer. The experimental set-up in the tank allows for the movement of a target in the XY-plane, and by measuring the time delays at several points on this plane, which is proportional to the distance, the closest point to the sound source on this plane can be found. This point will be referred to as the centre point. Each transducer has a centre point on the XY-plane in which the target can move. Using this plane as the reference for our coordinate system, the X and Y coordinates of the target when located at the centre point will then necessarily be the same X and Y coordinates as the transducer has. Finding the X coordinate is then only a question of finding the distances from the centre point to the transducer in question. Doing this only requires that the target is placed at the centre point and the propagation time between transducer and target is measured and multiplied by the sound speed in the water. A signal detection algorithm can be used, together with a measured sound speed, to find the distance which also gives the transducer's Z-coordinate.

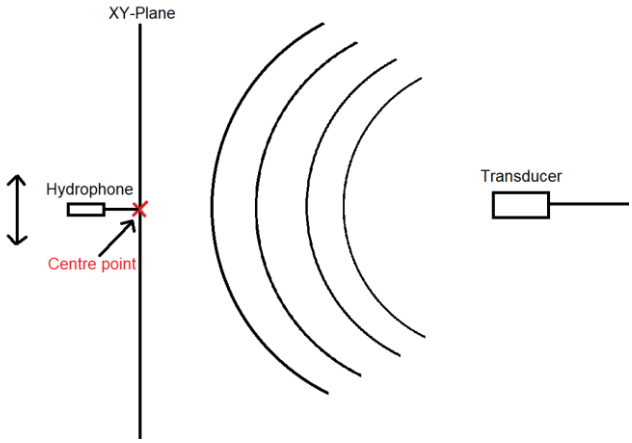


*Figure 3.22: Schematic of transducer location method.*

This can be done for all three transducers, finding their position in space relative to the ZY plane of the target. This coordinate system can then be shifted so that any point is the origin. Using one of the transducers as the origin is often preferable as discussed in section 2.5.

### 3.3.3 Signal amplitude determination

In order to determine the strength of a signal and by extension the target strength of any object the amplitude of a detected signal needs to be determined. For this study all amplitude measurements were done through a Fourier transform with the built-in MATLAB function *fft*, Fast Fourier Transform. After detecting and isolating the steady-state part of the received signal, the amplitude of the signal is given as

$$W(t) \rightarrow FFT \rightarrow W(f) \tag{3.1}$$

$$W_{amplitude} = 2 \times \frac{W(f_{input})}{n} \tag{3.2}$$

where $W$ is the steady-state part of the received signal, $f_{input}$ is the frequency of the transmitted signal and n is the number of samples in $W$. In this study $W$ was zero-padded to increase its length by a factor of 64 which is then compensated for in $n$.

As only half the energy in a signal in the time domain is contained in the positive frequencies [14], the value of $\frac{W(f_{input})}{n}$ is only half the story as the amplitude spectrum is mirrored for the negative frequencies. $\frac{W(f_{input})}{n}$ is then doubled to account for the equal amount of energy present in the frequency $-f_{input}$.

For the plots of amplitude spectrums shown in this study, the value of $W_{amplitude}$ as a function of frequency is displayed giving a direct reading of the voltage amplitude of every frequency present in the $W$.

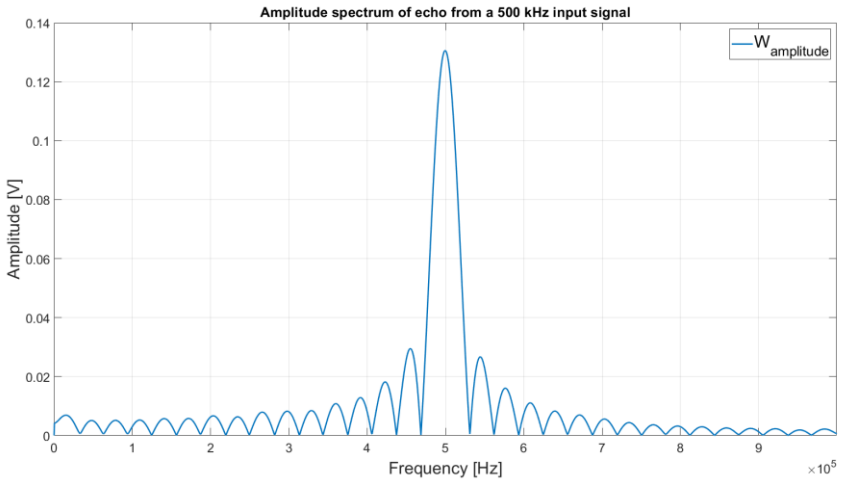


*Figure 3.23: Example amplitude spectrum.*

In Figure 3.3 a signal containing a 0.13 Volt amplitude, 500 kHz frequency has been fourier transformed and its amplitude spectrum is shown. The plot gives a direct reading of the amplitude as the calculation in equation 3.2 have already been done.

### 3.3.4 Signal averaging

Throughout this study the importance of signal to noise ratio is stated. One method used to increase signal to noise ratio is by signal averaging. By performing the same transmission and reception process several times and taking the average of all the measured signal, the noise will be averaged away. It is assumed that the unwanted noise is random and has a mean value of zero, meaning that if averaged long enough will become zero, leaving just the signal of interest. Doing this process can increase signal to noise ratio greatly and make it possible to detect signals otherwise berried in noise.

Noise bilde?

The oscilloscope used in this study, Tektronix TBS 2000B, has an in-built automatic averaging function. The user can choose how many replicant signal, or samples, to average over, from 2 to 512, denoted N. The oscilloscope then average n number of samples until it reached the desired value N [15]. Until this happens the signal are averaged using a stable averaging algorithm, which can be expressed as

$$A_n = A_{n-1} + \frac{X_n - A_{n-1}}{n} \tag{3.3}$$

where $A_n$ is the average of n samples and $X$ is is the next sample to be part of the average. When the number of samples averaged reaches the desired number N, an exponential averaging algorithm takes over from there:

$$A_n = A_{n-1} + \frac{X_n - A_{n-1}}{N} \tag{3.4}$$

As can be seen in the equation above, the average value $A_n$ keeps improving after N has been reached, meaning that even after N signals have been averaged, waiting even longer will still improve the signal to noise ratio. Due to this fact during this study, all measurements will be taken with N set to 512 and a total of 60 seconds will elapse before the averaged signal is saved in order to reach a the highest signal to noise ratio practical.

### 3.3.5 General measurement setup settings

Here is stated the settings used under all experiment done in this thesis. During all experiments the signal generator is used to generate the input signal to the transducer, while using a hydrophone the amplitude of the signal is set to 10 V peak-to-peak, while when using a calibration sphere the power amplifier is used to amplify the 222 mV signal from the generator in achieve 92 V peak-to-peak. The time delay between burst is dynamic throughout the study as finding a time window free from "old" echoes is crucial. Each set-up requires a slightly different burst delay as not to interfere with the next measurement as its echo is still present in the tank. The burst delay is set between 10 and 50 ms depending on the set-up. The dampening rubber panel is also always used to dampen any echo reflected off the back wall. The number of cycles used also depends on the experiment and is either set at around 20 or 45 cycles in order to achieve a long steady state part of the signal. All received signals are filtered through the analogue filter. During all experiments using 500 kHz signal the filter is set to a band-pass filter with cut-off frequencies of 144 kHz and 1 MHz and during experiments with the 1 MHz transducer the filter was set to band-pass with cut-offs at 500 kHz and 2MHz, which was experienced to give the best signal to noise ratio.

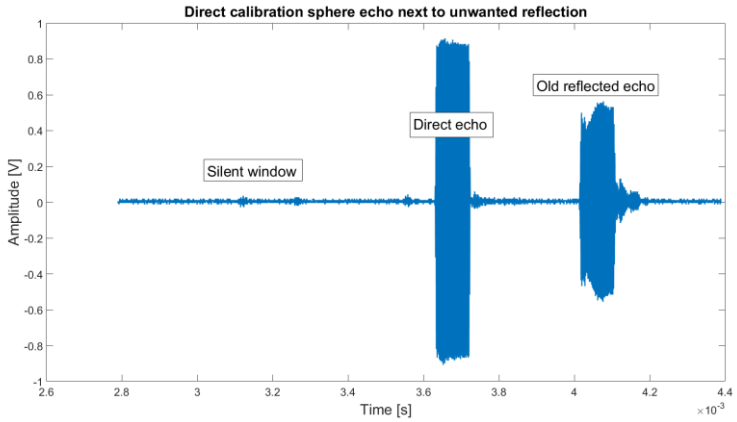


*Figure 3.24: Direct echo from calibration sphere next to echo from back wall from previous burst.*

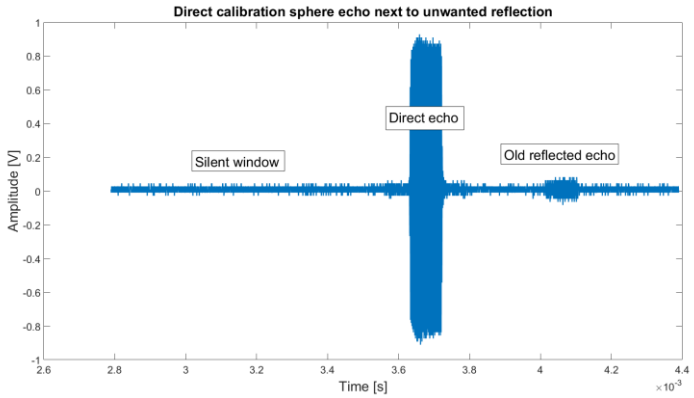


*Figure 3.25: Direct echo from calibration sphere next to echo from back wall from previous burst with dampening rubber panel installed.*

When using a calibration sphere, the sphere's resonance frequency was investigated to ensure the transducers used did not operate close to those frequencies to avoid dips in sphere's target strength interfering with the measurements. The discussion of which is in section 4.7.1.

All experiments were conducted in the far field of the transducers in use. The Rayleigh distance was used to estimate start of the far field [9]. Using the area of the transducer face and the wavelength of the transmitted signal, the Rayleigh distance is

$$d_r = \frac{\pi a^2}{\lambda} = 0.165\ m \tag{3.5}$$

For the 500 kHz transducer, and $2d_r$ for the 1 MHz transducer.

When using the transducer mounting plate for triangulation the positions of the transducers on the plate refer to the positions shown in Figure 3.26.


*Figure 3.26: Positions on transducer mounting plate.*

# 4 Results and discussion

This section presents the experiments done, their results and discussions on their meaning, significance to the objective and accuracy.

## 4.1 Simulated $\psi$-estimates

To get an idea of some expected values of $\psi$ and how the beam pattern affects it, some simulations using MATLAB were done. The code used can be found in appendix A.3. All calculations done in this section will be based on the piston model for transducer beam patterns. Firstly, some beam patterns of transducers with different characteristics were calculated. As seen in equation 4.1, the parameter affecting a transducer's beam pattern is, using the piston model, the $ka$-number. Some beam patterns resulting from different $ka$-numbers are plotted in Figure 4.1 using the equations acquired from the piston model presented in section 2.2. From the piston model we have

$$H(\alpha) = \left|\frac{2J_1(v)}{v}\right| \qquad v = ka\ sin(\alpha) \tag{4.1}$$

where H is the transducers beam pattern and $\alpha$ is the angle from the sound axis.

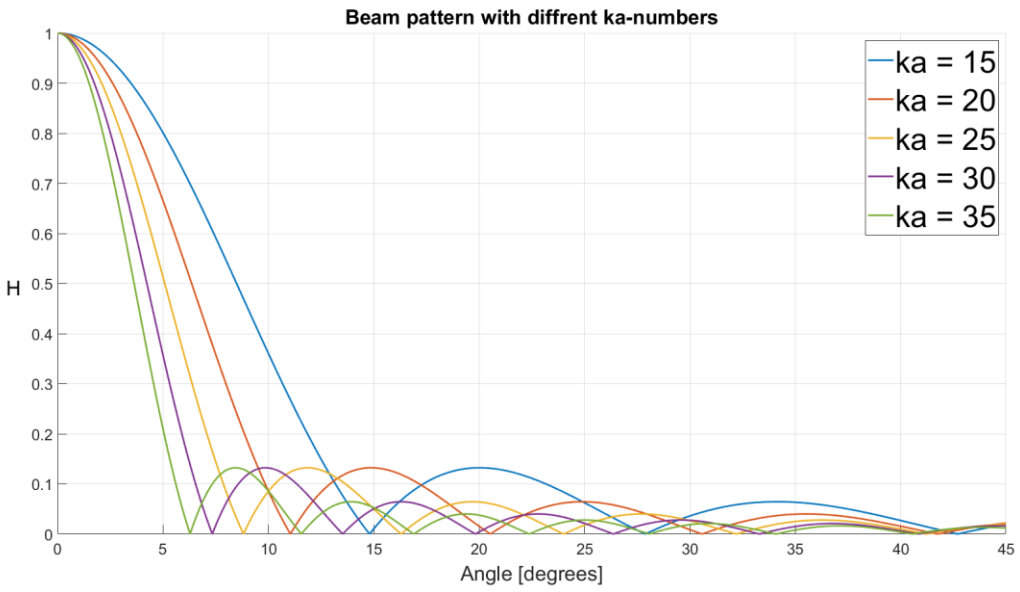


*Figure 4.1: Beam pattern with different ka-numbers using piston model.*

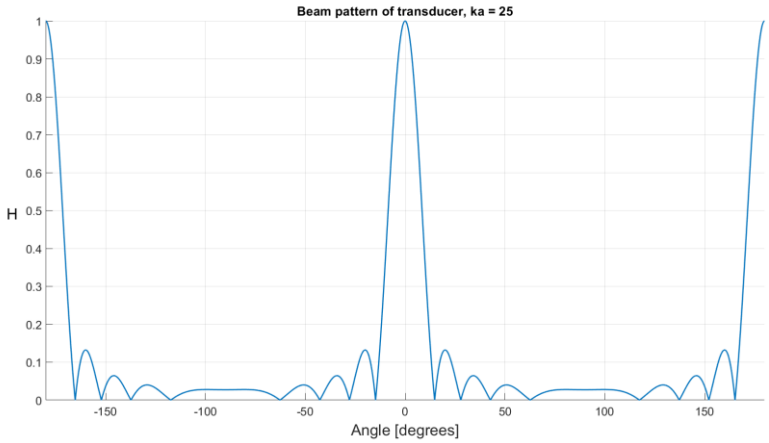


*Figure 4.2: Full beam pattern from piston model, ka = 25.*

Calculating the two-way equivalent beam solid angle is then a matter of integrating the beam pattern over all angles. Figure 4.1 & Figure 4.2 only shows a cross sections of the true beam patterns as it is 3-dimentional, and will, in this thesis, be assumed to be independent of the azimuth angle. Meaning the function H is effectively rotated about the sound axis at 0° to form the 3-dimensional beam pattern. Under the assumptions of the piston model, the beam pattern of a transducer is equal in opposite directions, shown in Figure 4.2. This is usually not the case with immersion transducers such as the ones used in this study as well as the ones used in fisheries acoustics [5]. As the piezoelectric element in these transducers are encased, almost all of the energy in the beam pattern is directed forward. The piston model doesn't give a good representation of the beam pattern of transducers used in practice outside of 90°. For this thesis it is assumed that almost all the energy and therefore contribution to $\psi$, lies within the first 90° of the beam patterns. Any further contribution can be compensated for as seen fit, depending on the circumstances. This "half-integrated" estimated value for $\psi$ will be denoted $\psi_h$. Based on equation 2.14, the expression for the estimation of $\psi_h$ can be written as

$$\psi_h = \int_0^{\pi/2} \int_0^{2\pi} H^4(\theta, \varphi)\, sin(\varphi)\, d\theta d\varphi \tag{4.2}$$

where $\psi_h$ is the two-way equivalent beam solid angle integrated over the hemisphere cantered at the sound axis, which is assumed to contain close to all acoustic energy coming transmitted by the transducer. $\psi_h$ is a function of the transducers $ka$-number and is plotted as a function of the $ka$-number in Figure 4.3.

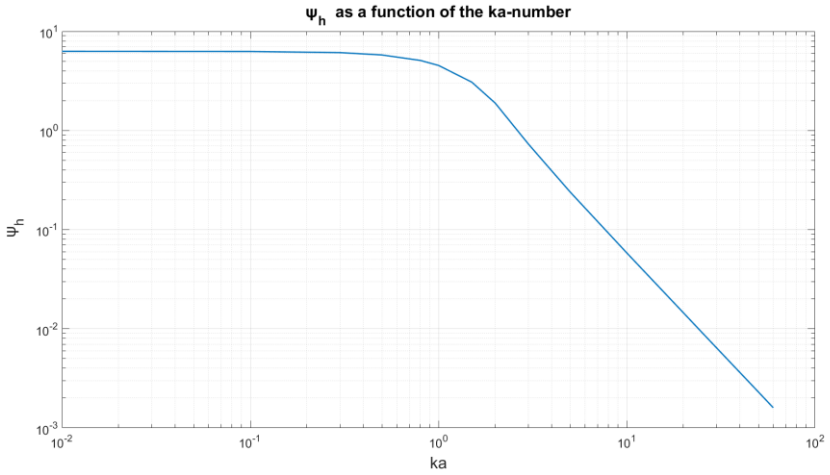


*Figure 4.3: $\psi_h$ as a function of the ka-number of the transducer, using piston model.*

### 4.1.1 Cumulative $\psi$

As seen in equation *4.2*, $\psi_h$ is a function of both the azimuth angle $\theta$ and the angle from the sound axis $\varphi$. In order to get the true value for $\psi_h$, all angles need to be integrated over, meaning $\theta = [0, 2\pi]$ and $\varphi = [0, \pi]$. As discussed in the section above, $\psi \cong \psi_h$, is assumed. The cumulated value of $\psi_h$, referred to as $\psi_c$ can then be plotted as a function of the angles integrated over, $\theta = [0, \hat{\theta}]$ and more interestingly $\varphi = [0, \hat{\varphi}]$. The relationship between $\psi_c$, as a percentage of $\psi_h$, as a function of $\hat{\varphi}$ is plotted in Figure 4.4. The wave number and face radius is chosen to be the same as for the 500 kHz transducers used in this study with a sound speed of $c = 1485\ m/s$,

$$ka = \frac{f \times 2\pi}{c} a = 26.44 \qquad 4.3$$

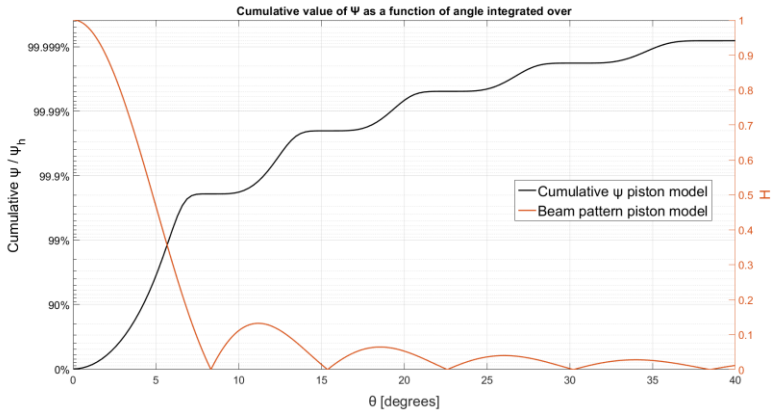


*Figure 4.4: Cumulative value of $\psi$ as a function of angle integrated over.*

As $\hat{\varphi}$ goes to 90°, the cumulated value $\psi_c$ approaches $\psi_h$. When $ka = 26.44$ most of the value of $\psi_h$ has been cumulated when only integrating over the main lobe, around 8°. In fact, 99.8 % of $\psi_h$ has been reached once $\hat{\varphi}$ is equal to the first zero. The first side lobe then contributes a further 0.018 %

and the second side lobe contributes 0.00015 % and so on. This growth of $\psi_c$ depends on the $ka$-number. The value of $\psi_c$ is plotted with several other values for $ka$ in Figure 4.5-Figure 4.9.

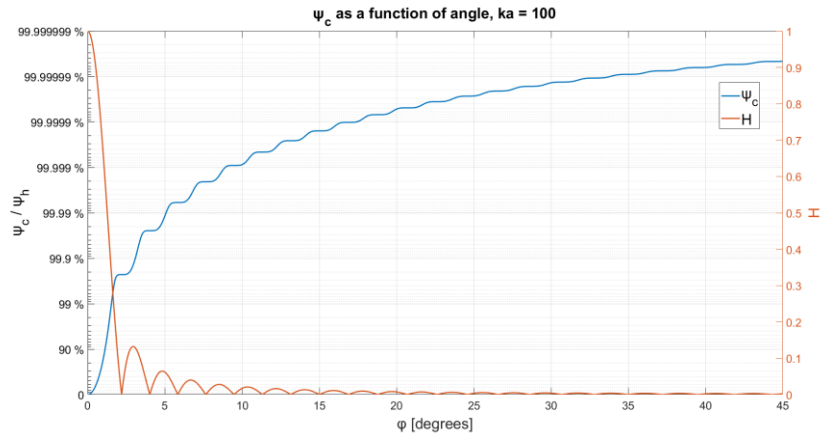


*Figure 4.5: $\psi_c$ as a function of angle integrated over, piston model, ka = 100.*

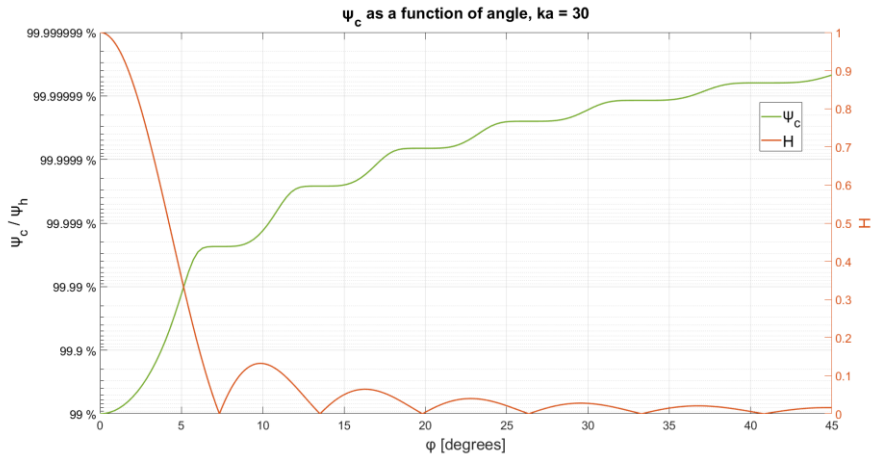


*Figure 4.6: $\psi_c$ as a function of angle integrated over, piston model, ka = 30.*

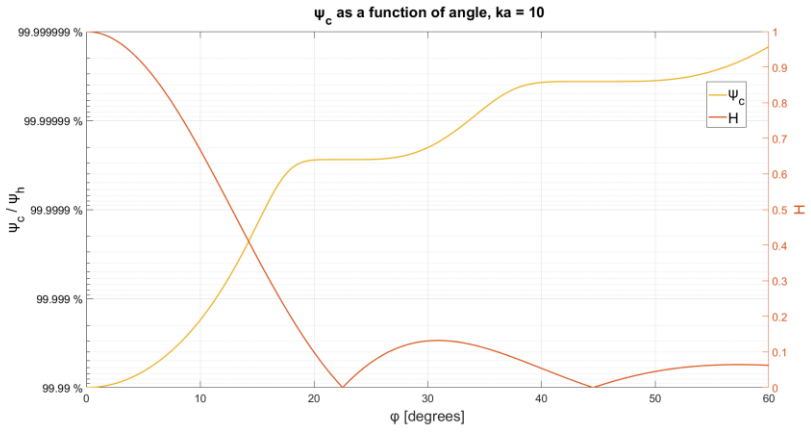


*Figure 4.7: $\psi_c$ as a function of angle integrated over, piston model, ka = 10.*

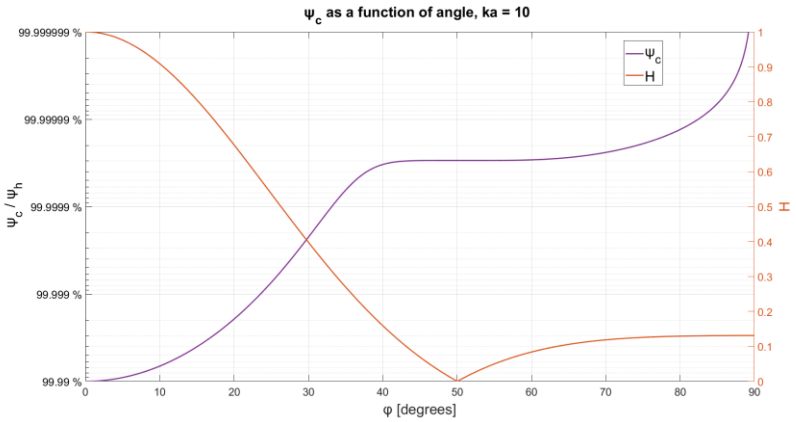


*Figure 4.8: $\psi_c$ as a function of angle integrated over, piston model, ka = 5.*

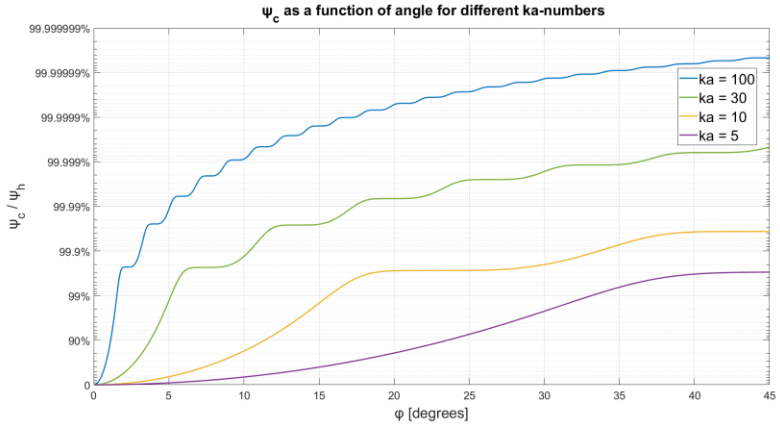


*Figure 4.9: $\psi_c$ as a function of angle integrated over, piston model, ka = 100, 30, 10 & 5.*

In the Figures above, the cumulative $\psi_c$ is plotted besides the corresponding beam pattern both found via the piston model. All plots of $\psi_c$ plateau when reaching the angle $\hat{\varphi}$ where the first zero of the beam pattern is located, this makes sense as when the beam pattern is close to zero, the contribution towards $\psi_c$ is also close to zero. Every following side lobe then contributes less and less toward $\psi_c$. As can be seen in Figure 4.9, the percentage value of $\psi_h$ when the main lobe in integrated over stays almost the same for all $ka$-numbers. Meaning the main lobe's contribution towards $\psi_h$ is about the same regardless of the $ka$-number, any discrepancy may only be due to the limited resolution when integrating using MATLABs "trapz" function. The angle required to integrate over does however become smaller as $ka$ increases. A similar plot Is shown in Figure 4.10, the x-axis represents the decibel drop in the beam pattern integrated over. As you move to higher angles $\hat{\varphi}$, the amplitude of the beam pattern drops and the plot shows how many dB drop needs to be integrated over to achieve a certain percentage of $\psi_h$. Since every lobe contributes the same percentage towards the total $\psi_h$ regardless of $ka$-number, the plot is the same regardless of $ka$-number.

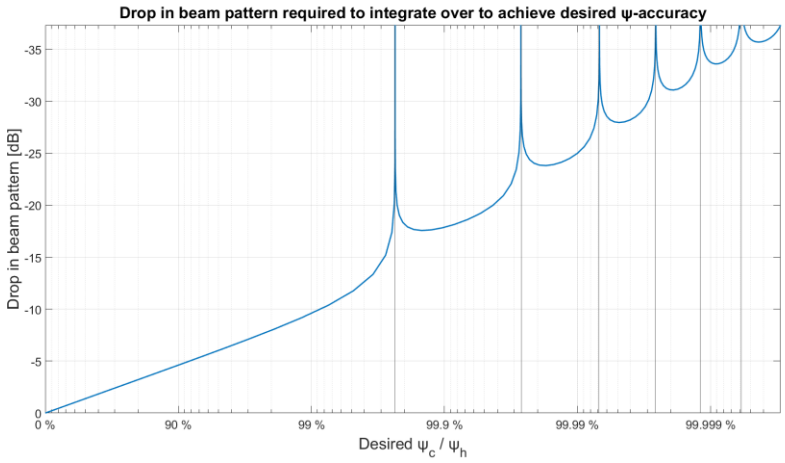


*Figure 4.10: dB drop in beam pattern reached when integrating over φ to achieve desired ψ-accuracy.*

Each asymptote represents the zero-points between lobes in the beam pattern and the percentage of $\psi_h$ achieved by integrating to that angel. As seen on the plot, if 99.9 % of $\psi_h$ is desired, $\psi_c$ needs to be integrated from 0 to just past the angle of the peak of the first side lobe, at 18 dB drop in amplitude. If 99 % is desired Integrating to when the beam pattern has dropped by 9.6 dB is sufficient, and if only the angle corresponding to a 3 dB is integrated over then the resulting $\psi_c$ will only be 78.8 % of $\psi_h$.

As suspected, when using the piston model to calculate $\psi_h$, almost the entire contribution comes from the main lobe and the amount of contribution does not seem to be affected by the $ka$-number of the transducer in question. Integrating over the entire beam patterns may not be necessary, as one can just as easily add the missing amount after integrating over just the main lobe to compensate.

## 4.2 Boundary reflection consideration

The possibility of reflections from the side walls or water surface interfering with the desired direct echo when using a calibration sphere is here investigated. If the burst is long enough and the delay between the direct path and the surface reflection path is short enough the two signals may overlap upon arrival back at the transducer again. Assuming a single burst of frequency 500 kHz, specular reflection off all surfaces, a water sound speed of 1485 m/s and omnidirectional scattering from the target sphere, the time delay between a direct echo and an echo reflected of a single surface was found. A short program was written to calculate the delay and the results are shown in Figure 4.11.

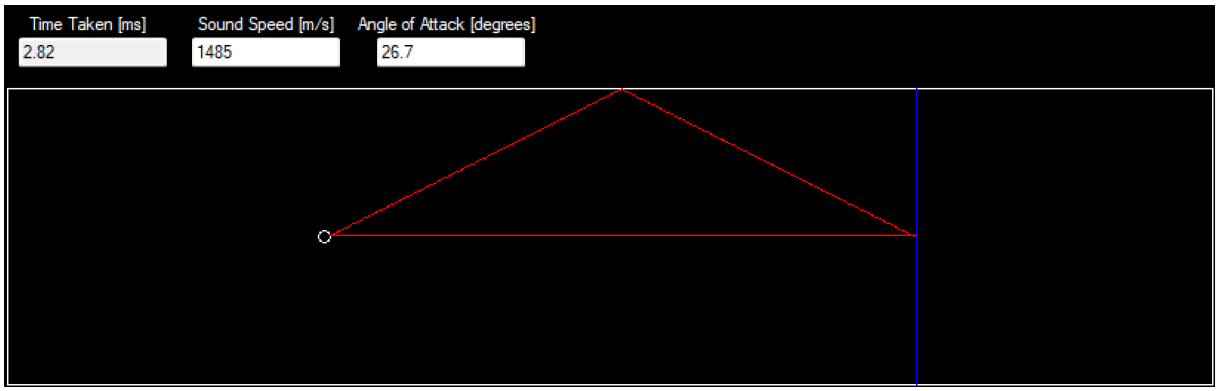


*Figure 4.11: Simulated ray reflected of calibration sphere in experiment tank to calculate delay between direct echo of surface reflected echoes.*

The white rectangle represents the experiment tank seen from above, the side or underneath. The blue line is the transducer plane, place 1 meter from the end wall and the white circle is a calibration sphere also placed 1 meter from the end wall, leaving 2 meters between them. The red line is a sound ray traveling from the transducer plane to the sphere and being reflected back, with one reflection of the wall, either on its way to the sphere or back. This is the shortest path involving surface reflections and therefore gives a lower limit to the time between direct and reflected echoes. At an angle of attack of 26.7°, the ray strikes the sphere and reflects back to the transducer, taking $t_r = 2.82\ ms$ to do so. The direct path takes the sound wave

$$t_d = \frac{4\ m}{c} = 2.69\ ms$$

to traverse, making the delay between the two arrivals

$$\Delta t = t_r - t_d = 2.82\ ms - 2.69\ ms = 0.13\ ms.$$

This delay gives room to send a burst containing

$$n = 0.00013\ s\ \times 500\ 000\ Hz = 65\ cycles$$

before any surface reflected echo might interfere with the direct echo. Closing the distance between the transducer and sphere results in a larger time delay. Since no experiment in this study is performed at a distance much further than 2 meters, 65 cycles will not be exceeded as a burst length. Any side wall or water surface reflected wave will also be subject to the transducers directivity at making the signal significantly weaker than the direct signal.

## 4.3 Directivity

Before conducting experiments, it is important to know the characteristics of the equipment used. In this work, one hydrophone and four transducers are used during various experiments. Knowing the directivity of these is crucial as it will serve as a reference to compare the results of the experiments

to. The hydrophone used is omnidirectional and therefore has no bias in its directivity. This is practical as it is therefore not necessary to account for its directivity in the experimentation. The transducers, however, do have directivity in both sending and receiving of acoustical signals. For this work it is assumed that the directivity function is the same for both of these operations.

### 4.3.1 Theoretical directivity

Using the principles of the piston model, presented in section 2.2, the theoretical directivities of various transducers can be calculated. In this section the theoretical beam patterns for the transducers used in this study will be presented and compared to the measured beam patterns.

Using the radius of the transducers used in this study, their operating frequency of 500 kHz, as well as an estimation of the sound speed in water of 1485 m/s, the value for $ka = \frac{2\pi}{\frac{1485}{500000}} \frac{0.025}{2} = 26.44\, m^{-1}$ and plotting H. The same can be done for the 1MHz transducer which is of the same size. Then, $ka = 52.88\, m^{-1}$.

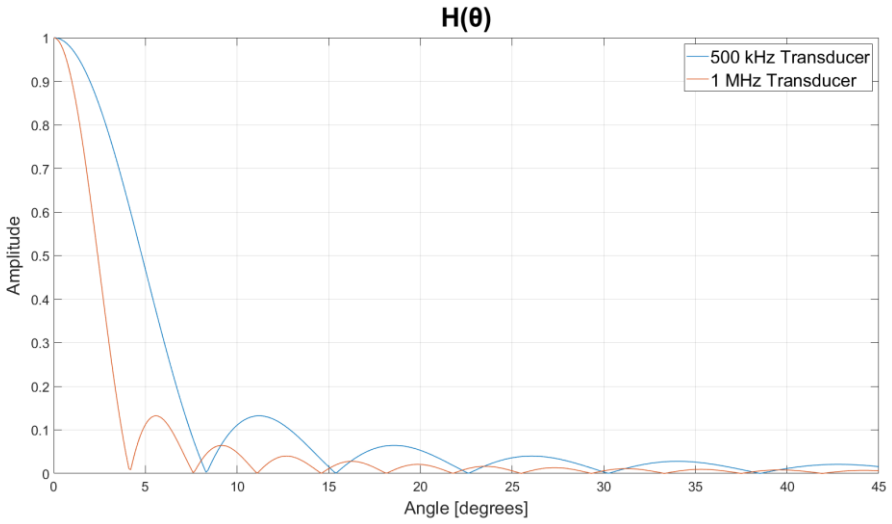


*Figure 4.12: Piston model directivity estimating 1 MHz and 500 kHz transducers beam pattern.*

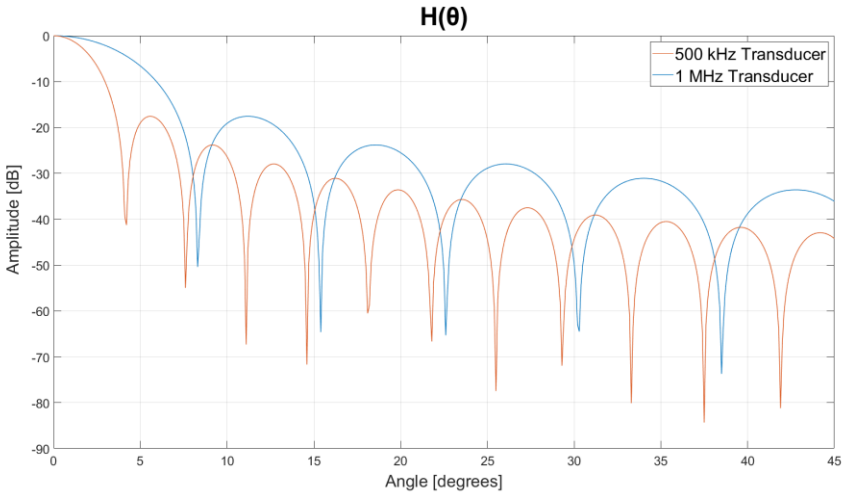


*Figure 4.13: Piston model directivity estimating 1 MHz and 500 kHz transducers beam pattern in decibel.*

An estimate for the directivity of the two transducers used in this study has now been found. Keeping in mind that this represents the one-way directivity. It is still of interest to measure the directivity of all four transducers to see how well the piston model fits, as well as comparing the transducers to each other. Any difference or anomaly in the directivity of any of the transducers should be noted.

### 4.3.2 Measuring transducer directivity

In order to measure the directivity, the transducers need to be placed in the tank without any baffle or other scattering objects near it. The transducers also need to be rotatable about the middle of its front face, such that only the angle to the target is changed and not the distance. This was achieved with the machined free field mount described in section 3.1.3.2.

The transducer is attached to the bottom of the free field mount, facing in the z-direction, while the mount itself is mounted to one of the stages which is able to rotate the free field mount, and therefore also the transducer, in the horizontal plane. If the transducer is rotated to a known angle while emitting a signal through the water at a target, such as a hydrophone, the strength of this signal can be measured. This can be done a range of angles. The strength of the signal received by the hydrophone can then be plotted against the angle measured at. If all the amplitudes are then divided by the maximum amplitude measured, the directivity of the transducer can be found. This method finds the directivity of the transducer on a plane and not the complete 3-dimensional directivity. It is, during this part of the study, assumed that the 2-dimensional directivity measured on with this method is representative of the complete directivity. During all directivity measurements the hydrophone in placed at 1 meter from the transducer.

Since the temporal position of the received signal does not change as the angle changes, the part of the signal chosen as the steady state can be the same for all signal measured at all angles. Meaning that a constant window in time was chosen as the part of the signal used to extract the amplitude from, using the cursor method. In these experiments, the signal supplied to the transducer was 500 kHz, 10 V peak to peak, and 22 cycles. The window used to find the amplitude is chosen manually before running the experiment. Below is plotted the signal measured at the top of the main lobe, on the sound axis of the transducer, and the signal received at one on the zero-points between lobes (here at 8.3°). Both signals have been normalized to make it easier to see where the window cuts the signal. The signal at the zero-point is much weaker than the one on the sound axis.

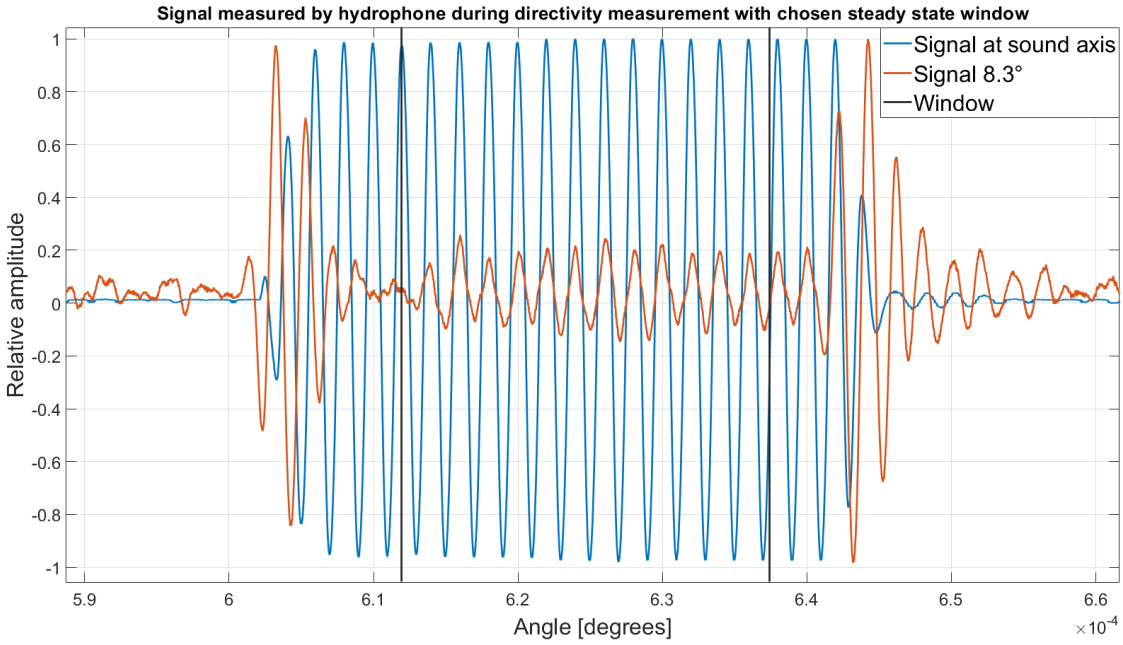


*Figure 4.14: Signals recorded by hydrophone during directivity measurement at 1 meter using 500 kHz.*

### 4.3.3 Free Field

All three directivities of the 500 kHz transducers used in the study were measured and are plotted below, as well as a comparison between transducer $\beta$ and the theoretical piston model. This is plotted both in relative amplitude and in decibel. All this is also done for the one 1 MHz transducer.

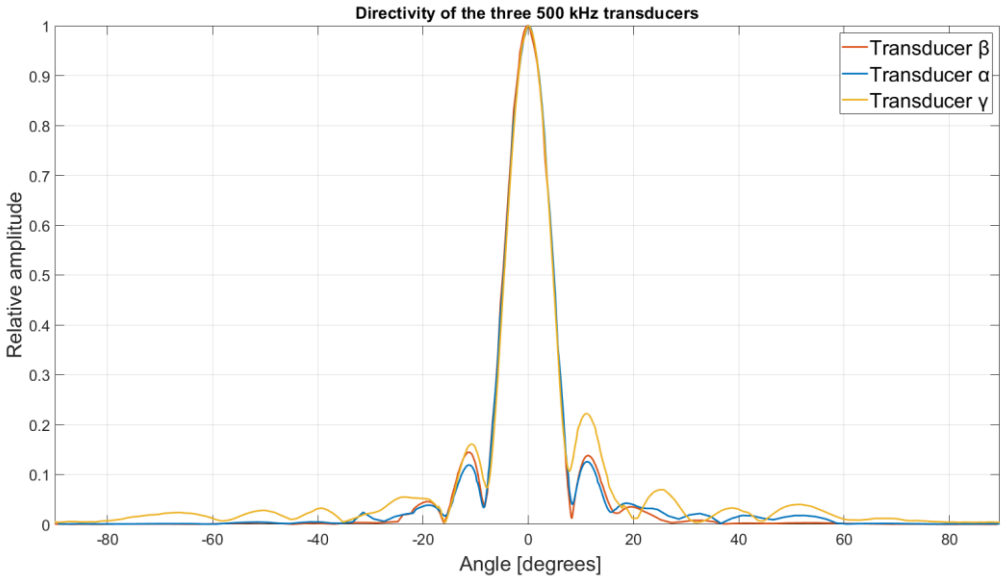


*Figure 4.15: Directivity of the three 500 kHz transducers as measured by hydrophone.*

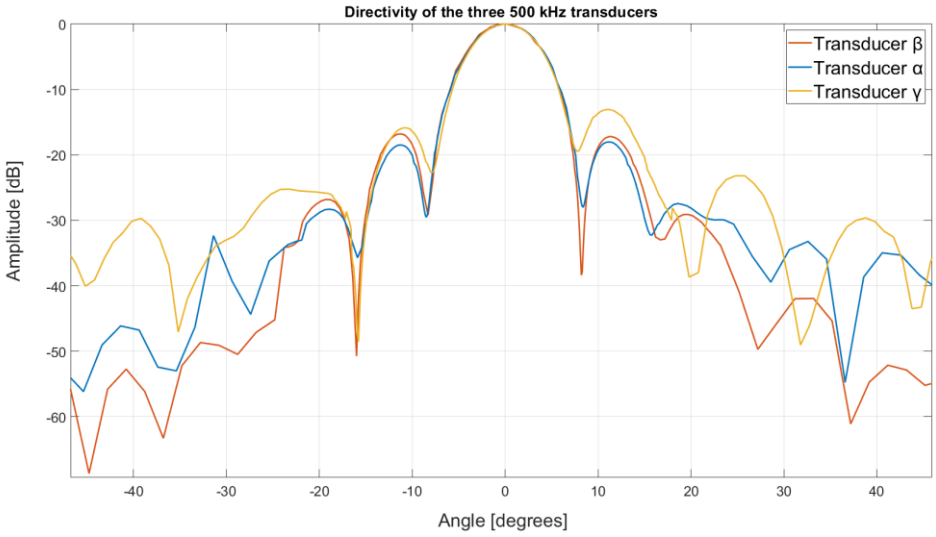


*Figure 4.16: Directivity of the three 500 kHz transducers as measured by hydrophone in decibel.*

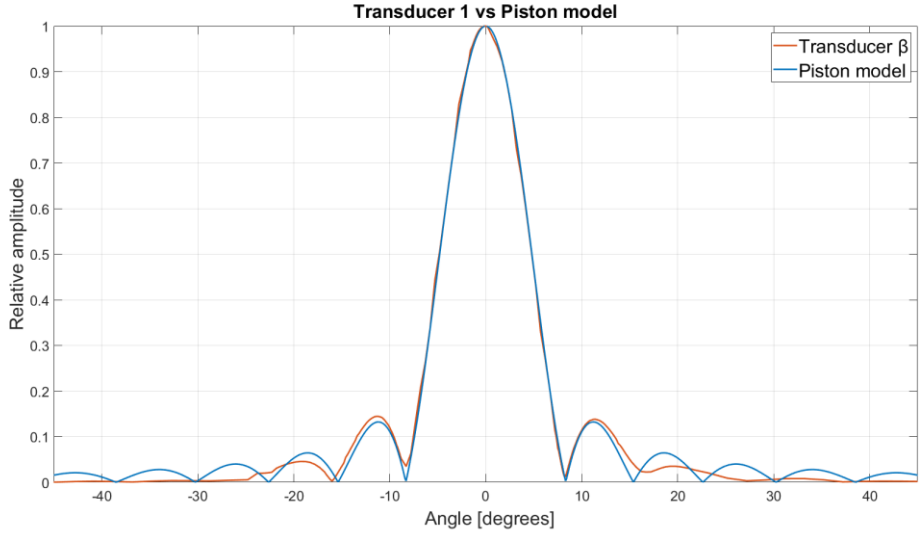


*Figure 4.17: Directivity of transducer β compared to piston model.*

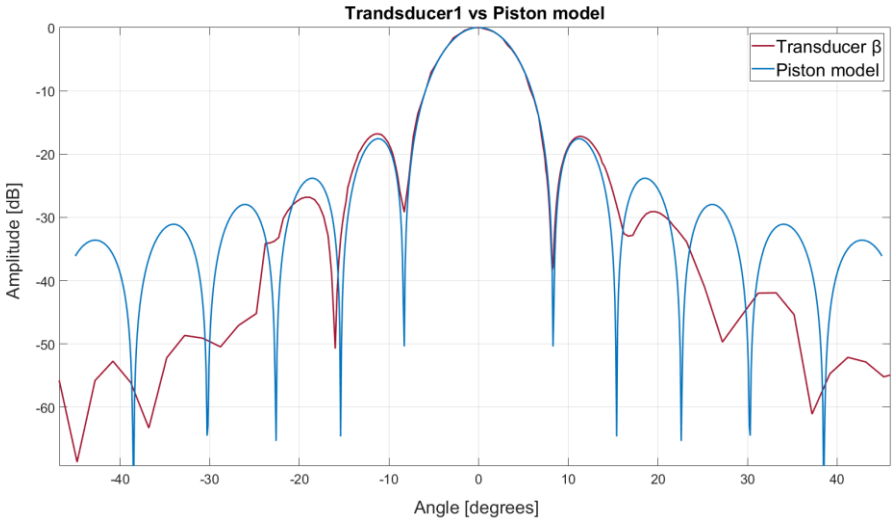


*Figure 4.18: Directivity of transducer β compared to piston model in decibel.*

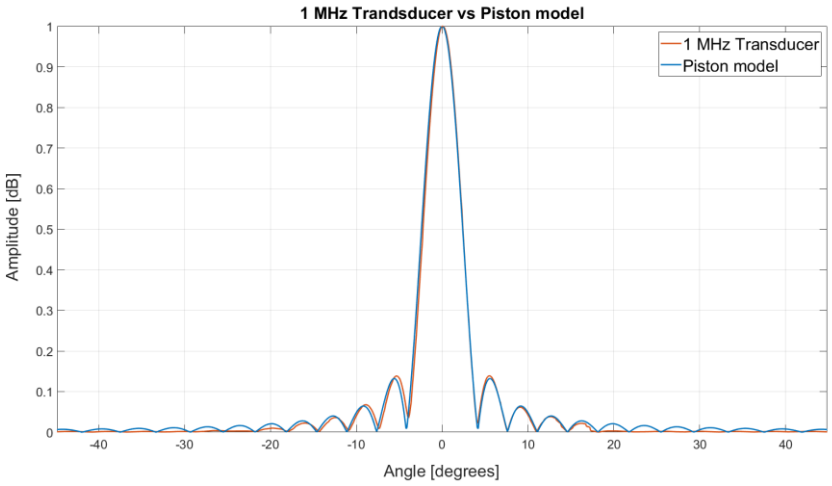


*Figure 4.19: Directivity of 1 MHz transducer compared to piston model.*

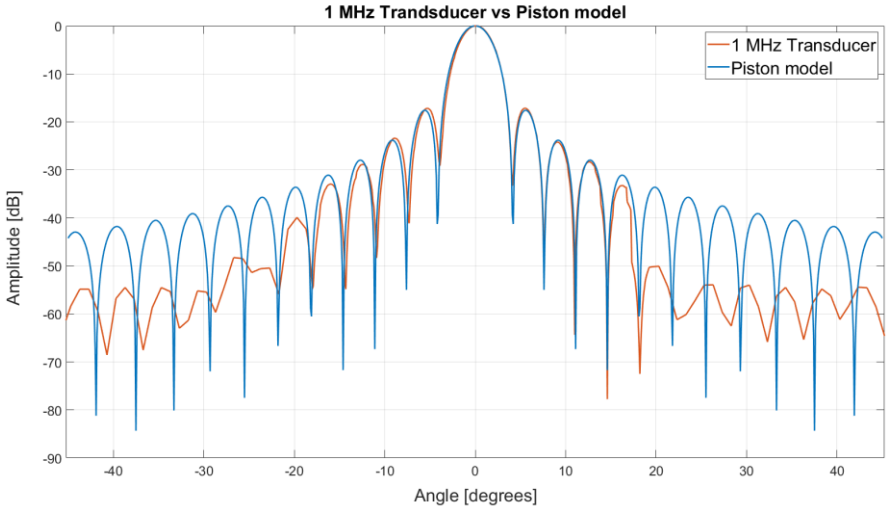


*Figure 4.20: Directivity of 1 MHz transducer compared to piston model in decibel.*

All the measured directivities have been centred around their maximum measured value, choosing it as the sound axis. Aliasing at the top of the main lobe may shift the directivity slightly to one side as the true peak might not be captured due to it being between measurement angles.

The conclusion to these measurements is that the transducers in use in this study have directivities that closely resemble the one derived by the piston method. They also have symmetrical directivities with even heights for both side lobes. The -3 dB angles as well as the zero-points line up with the expected values as well as being equal on both sides and between transducers of the same frequency.

These statements are true for all but one of the transducers. The transducer labelled “Transducer $\gamma$” seems somewhat of an anomaly. Having both higher peaks and lower troughs around at the side lobes, and even having a significant difference in amplitude between the two side lobes on either side of the sound axis, and both being higher than that of the other transducers with the same frequency. The reason for this discrepancy is not known. The only known difference between the three transducers is

that transducer $\gamma$ is completely new and was bought for this study, while the two other transducers were already present at the laboratory and had seen some use in previous projects. The first two transducers were also measured with the exact same set-up over the span of a few days, the 1 MHz transducer was also measured at this time. While the newer transducer, $\gamma$, was measured later on a set-up made to mimic the set-up used for the other transducers. Although nothing apparent was different between the two set-ups, this might be part of the explanation for the discrepancy in directivity between the transducers.

A quick check to see if the signal from the two side lobes of transducer $\gamma$ really have such different amplitudes was performed, to see if there was no fault in the amplitude calculation method. The signals received by the hydrophone when placed at the two angles corresponding to the peaks of the side lobes are plotted in Figure 4.21. The two signals do indeed have different amplitudes and the reason why remains unknown.

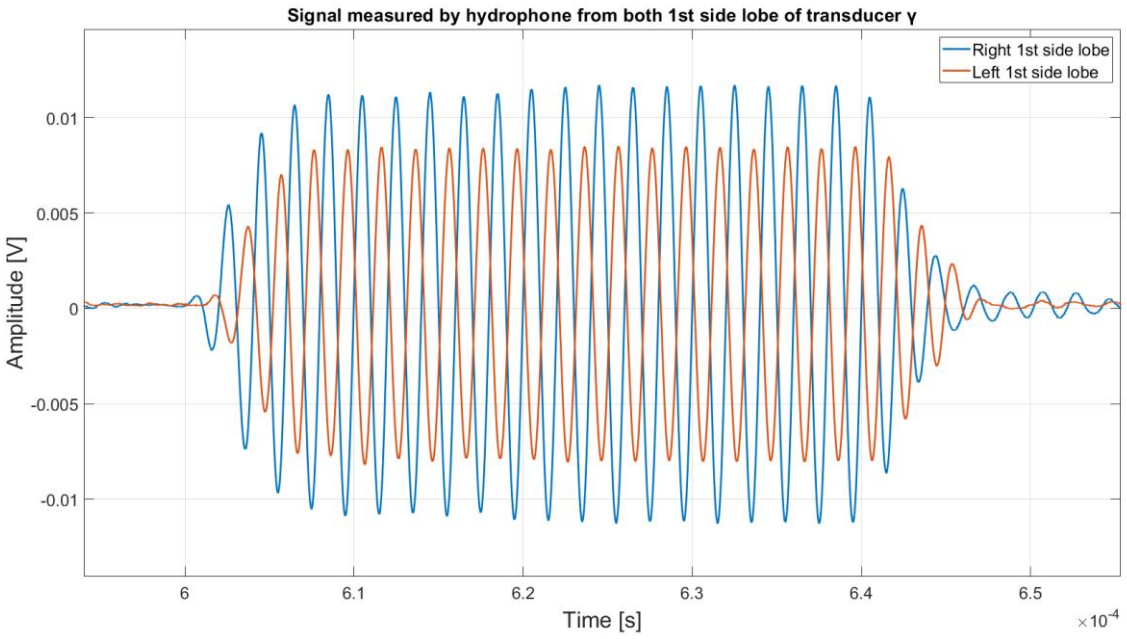


*Figure 4.21: Signal recorded at both sides of the first side lobe of transducer $\gamma$.*

### 4.3.4 Baffled

Since the transducers used by IMR have their value for $\psi$ measured by the manufacturer in free field, meaning the transducer is not baffled, the resulting value may be different to what it is in reality when the same transducer is placed in a keel and baffled. A short investigation into the effects of bafflement on transducers were conducted in order to see if the directivity and therefore the value for $\psi$ changes when a transducer is baffled. Three parts where machined for use in this experiment, these are described in section 3.1.3.3. The two baffles where mounted to Transducers $\beta$ and the resulting directivity measured using the free field mount. The resulting directivities as well as a free field control directivity of the same transducer at the same distance is plotted below. Only one side of the directivity

was measured for the sake of time. All Measurements were done at a distance of 1 meter, using a signal of 500 kHz, 10 Volts peak to peak and with 22 cycles.

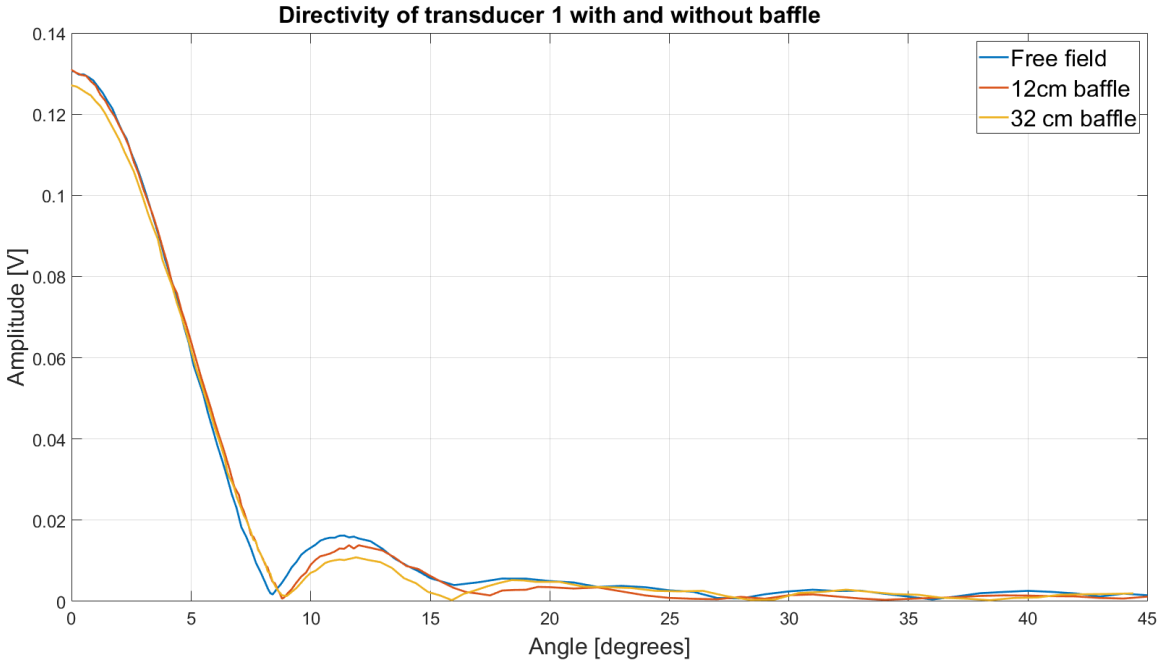


*Figure 4.22: Directivity of transducer β with and without a baffle, 500 kHz.*

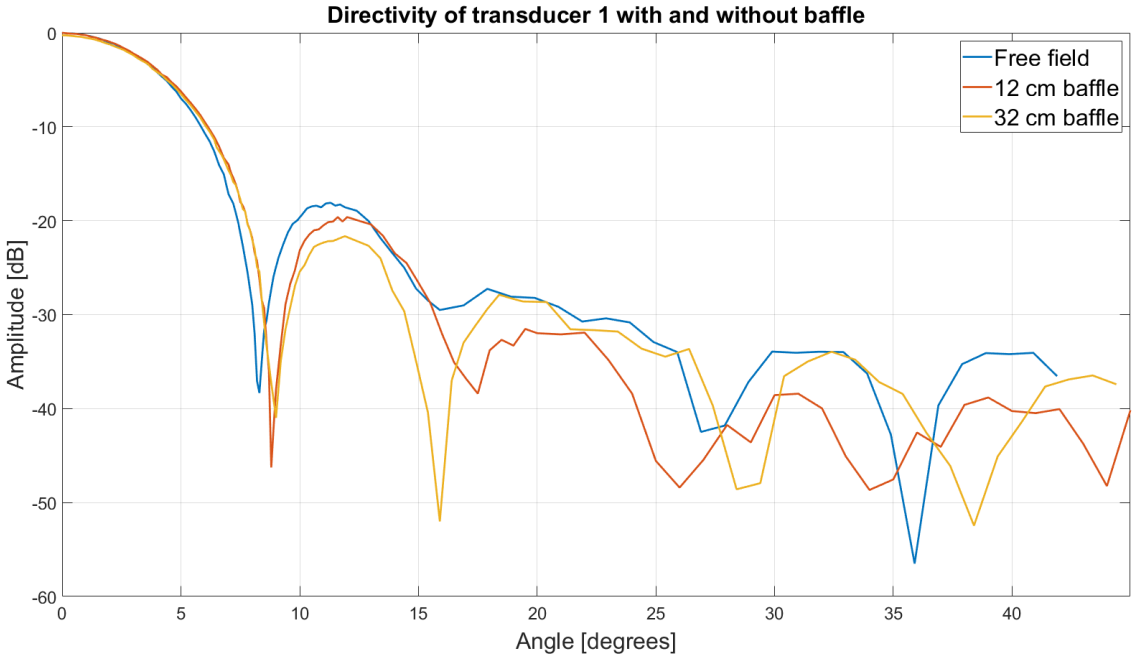


*Figure 4.23: Directivity of transducer β with and without a baffle in decibel, 500 kHz.*

The results seem to indicate that the amplitude of the main lobe is not affected much, at least not with a baffle as small as 12 cm. The 32 cm baffle seems to have lowered the amplitude at the sound axis somewhat. The main lobe has been widened by using a baffle, the first zero-point has moved from occurring at around 8.3 degrees for free field to being at around 8.8 degrees for the 12 cm baffle and

9 degrees for the 32 cm baffle. The amplitude of the signals in the first side lobe have been dampened, somewhat when using the 12 cm baffle and more so using the 32 cm baffle. More of the energy seems to be placed in its main lobe, widening it, while dampening the side lobes.

Below is plotted the amplitude spectrum for all three cases at both the sound axis and at the first zero-points, 8.3°, 8.8° and 9°.

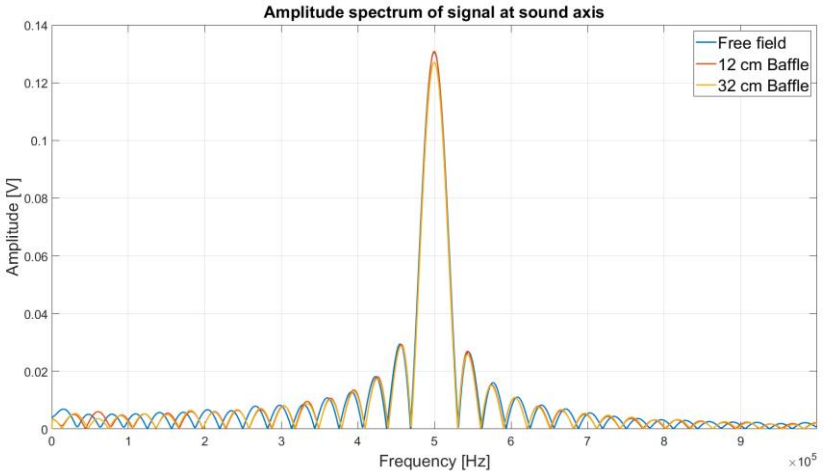


*Figure 4.24: Amplitude spectrum of signal received by transducer β at the sound with different sizes of baffle.*

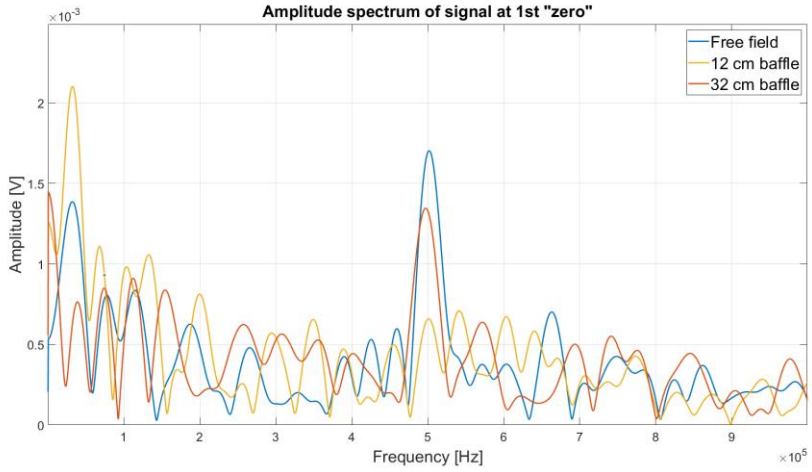


*Figure 4.25: Amplitude spectrum of signal received by transducer β at first "zero" with different sizes of baffle.*

## 4.4 Sound speed

In acoustic experimentation, knowing the sound speed in the medium used is crucial. In the case of this study, the accuracy triangulation method heavily relies on the accuracy of the sound speed in the medium, as it directly affects the distances used for calculating the target position. If the sound speed, and therefore the distances used, are faulty, the results of the triangulation calculation will be faulty. Using faulty target positions will result in an inaccurate or wrong directivity estimate for the transducers and the estimate for the two-way beam solid angle will then be faulty. Measuring the sound speed in the medium used is therefore of high importance. In the case of this study, the medium

used is fresh water in room temperature. The water is presumed to be clean and free from bubbles. Some build-up of algae has been experienced over time, however. It is unknown if this will affect the sound speed. Both a theoretical and a measured value for the sound speed is found in this study. These values can be compared to see if perhaps algae or other factors may affect the speed. Calculating a theoretical sound speed involves measuring some of the water's properties.

### 4.4.1 Water temperature

Water temperature is not as easy to calculate from known factors and also affects the sound speed much more. Using a temperature that is off by only one degree Celsius will change the outcome by almost 3 m/s at normal room temperatures. For this reason, it is important to measure the water temperature directly. This was done using a Pico SE012 PT100 resistance thermometer, which has an accuracy of $\pm 0.03$ °C @ 0 °C [16]. The Thermometer was first used in the air while testing, then placed in the water, behind the transducers to prevent interference. Measurements were taken and saved every 10 minutes.

After configuring the PT100 Resistance thermometer it was placed on the desk in the laboratory on the 10th of March to see the value and the fluctuations of the air temperature. The thermometer was left over the weekend. The same weekend a set of long-lasting acoustic experiments were conducted in the tank. These experiments required the power amplifier to be turned on throughout the experiment's duration. This amplifier, along with the signal generator, analogue filter, computer and monitor all produce low to moderate amounts of heat. Since the thermometer was placed on the same desk as all these instruments, the change in temperature can be seen. The weekend of the experiment, when the temperature was high, as well as the following days where temperatures went back to normal, as well as some spikes from short uses of the amplifier at certain times during the week.

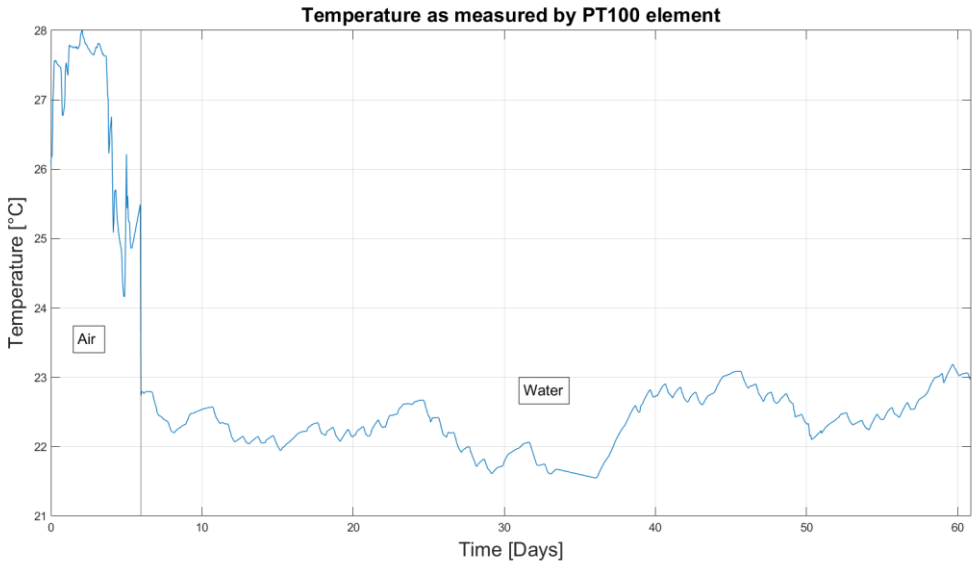


*Figure 4.26: Temperature measured by PT100 resistance thermometer*

After almost a week of air temperature measurements the sensor was placed in the water. The moments this happened can be seen on the graph in Figure 19, as the temperature suddenly drops almost three degrees Celsius. As expected, the temperature of the water stays a lot more constant than in the air due to the waters higher specific heat capacity as well as lack of circulation. The average of the temperature in the water was 22.39 °C and had a standard deviation of 0.36 °C. The small peaks in the temperature seen throughout the measurements under water, are exactly 24 hours apart, showing the temperature swings over this period. Temperature difference over course of a day seems to be about 0.2 °C or less. There seems to be larger fluctuations that last over much larger periods of time. It is worth noting that the measurement instrument was moved slightly on day 36, to a shallower depth in the tank. The temperature seems to have risen slightly due to this, indicating a temperature gradient in the water column.

### 4.4.2 Theoretical sound speed

In this case we will compare the experimental results to the sound speed model for distilled water found in Kinsler and Frey [9]:

$$C(t) = 1402.7 + 488t - 482t^2 + 135t^3 + (15.9 + 2.8t + 2.4t^2)(\wp_G/100) \quad 4.4$$

where $t = T/100$, $T$ being temperature in Celsius, and $\wp_G$ is the Gauge pressure in bar. The model is accurate to within 0.05 % for temperatures between 0 and 100 degrees Celsius [9]. The gauge pressure can be approximated sufficiently by subtracting normal atmospheric pressure from the absolute pressure at the measurement depth. This will be sufficient as a change in calculated sound speed from using surface pressure, and using 1 meter water depth is less than 0.02 m/s. Since the tank is only 1 meter deep and the measurements were taken at about halfway deep, measuring as apos to calculating the gauge pressure won't affect the end result in any meaningful way. The gauge pressure $\wp_G$ is set to that of the middle of the experiment tank, that is, about 50 cm below the water surface. At this depth the gauge pressure is

$$\wp_G = \rho g h \quad 4.5$$

Using a water density of $\rho = 1000\ \frac{kg}{m^3}$, gravitational acceleration of $g = 9.81\ \frac{m}{s^2}$ and a height of $h = 0.5\ m$. The resulting gauge pressure is 4905 pascals, or 0.04905 bar. The sound speed can then be plotted using the temperature in the water as the variable.

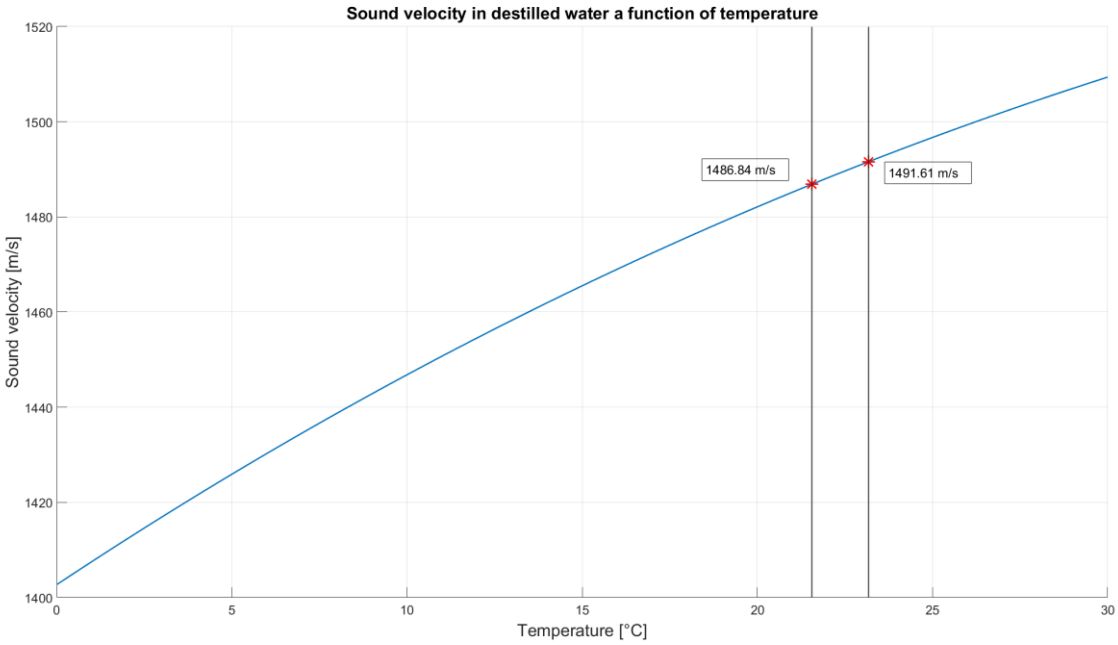


*Figure 4.27: Theoretical sound speed in water as a function of temperature.*

The calculated sound velocities at minimum and maximum measured temperatures in the water are labelled on the plot. These being 21.55 and 23.18 degrees Celsius. The calculated sound speed for in the water lies somewhere between 1486.84 and 1491.61 m/s, depending on the temperature of the water. The average value of the water temperature of 22.39 degrees gives a sound speed value of 1489.32 m/s.

### 4.4.3 Measured sound speed

The method used to find the sound speed in the water was to measure the time delay between sending and receiving at two different distances. Taking the Difference between these two delays eliminates any other factor than the actual propagation time, which then can be used to find the sound speed. The set-up involves using a transducer to send a signal and a hydrophone to receive it, as well as the tanks translation system so that an exact distance difference can be known.

#### 4.4.3.1 Set-up

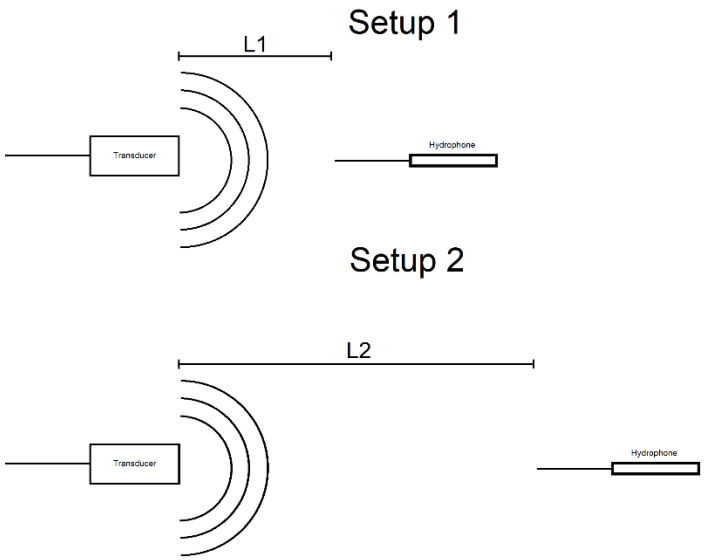


*Figure 4.28: Sound speed experimental set-up.*

The time delay in the two cases can be written as.

$$t_1 = \frac{L1}{c} + t_s \qquad t_2 = \frac{L2}{c} + t_s \tag{4.6}$$

$$t_2 - t_1 = \frac{L2 - L1}{c} \qquad c = \frac{\Delta L}{\Delta t} \tag{4.7}$$

Where $t_1$ and $t_2$ are the time delays measured in set-up 1 and 2 respectively. L1 and L2 are the distances in these two set-ups, $c$ is the sound speed and $t_s$ is the system delay. Doing this at two known distances, the system delay cancels out and the sound speed can be calculated.

These set-ups can be achieved by using the translation system present on the experimental tank. This translation system allows for translation between the two stages on the tank in the direction parallel to the side walls of the tank, the same way as sound propagation in this experiment. This is the x-direction in the tank.

In order to be able to use the translation system for this experiment, the hydrophone needs to be placed at the closest point to the transducer on the XY-plane. The reason this is important is that the distance difference L2-L1 can only be known if the translation happens in the same direction as the line between the transducer and the hydrophone. If this line is not parallel to the translation direction,

or z-axis, then the difference in distance will not be equal to the distance translated by the translation system.

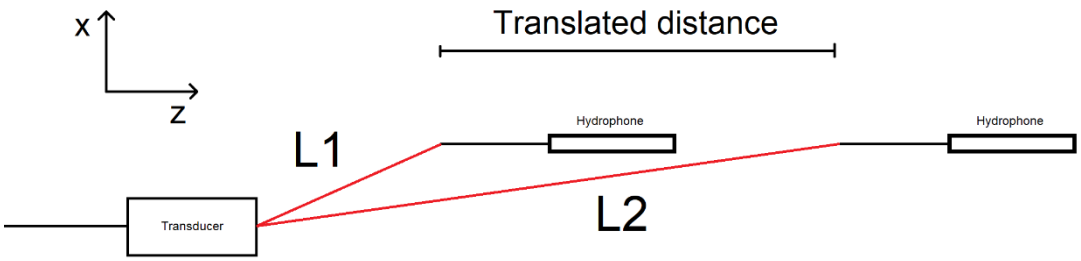


*Figure 4.29: Importance of translation direction. The difference between L1 and L2 is not the same distance as the translated distance, which could cause faulty measurements.*

In Figure 4.29 the distance L1 and L2 are labelled, these will be the two distances we measure. However, the translation distance, which is in the z-direction, is not the same distance as the difference between L2 and L1. Since we don't know the distances L1 and L2 and only know the translated distance, they need to be the same value in order to be able to calculate the sound speed. The x- and y-coordinates of the hydrophone therefore need to be the same as the transducer.

The method used to find the start of the received signal is important to mention as this value is directly involved in calculating the sound speed and can also be found via many methods resulting in different values. For this experiment the only important thing is the difference between the starts of the two signals received at the two measurement distances. This means that the start of the signal is not necessarily the part needed to be timestamped. As long as the same part of both the signals is the detected with accuracy, the relative difference will be the same. The method chosen to detect the signals was the cross-correlation method, described in section 3.3.1.4. This was chosen for its consistency in signal start detection time. The same part of the signal was detected every time with very little variation.

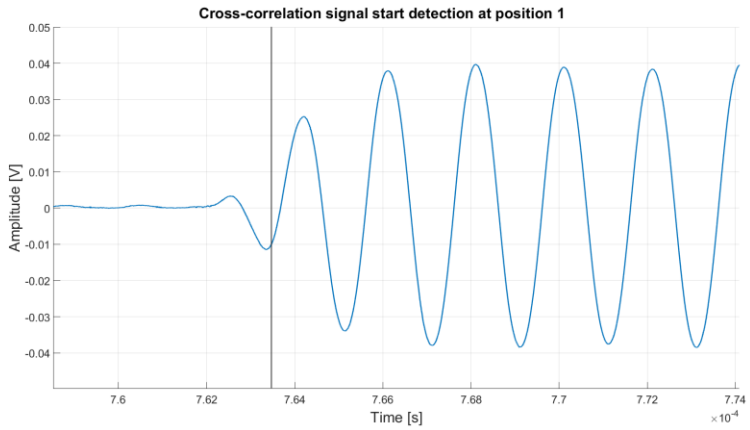


*Figure 4.30: Signal start detection at position 1.*

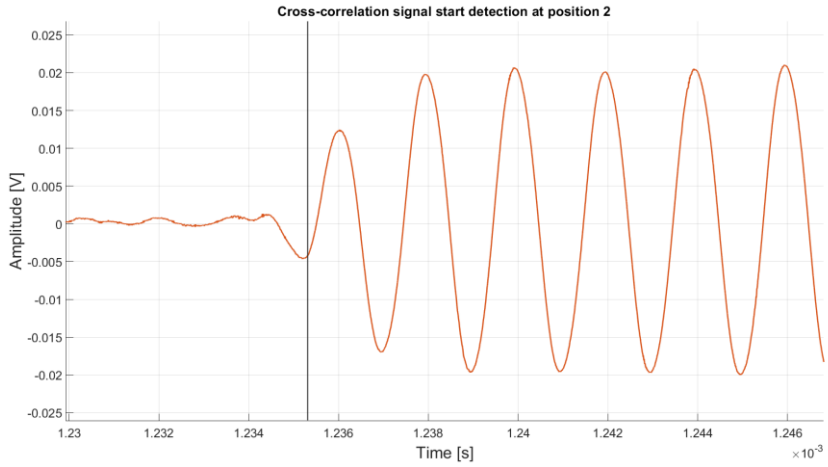


*Figure 4.31: Signal start detection at position 2.*

### *4.4.3.2 Stage offset*

Since the Translation system is fastened to the two stages with a metal rod and placed over one of the rails on the side of the tank, the force pushing or pulling the stages apart or closer will be concentrated on only one of the railings. This results in stage being moved to be slightly offset as its railed "legs" are being pushed while the other lags behind.

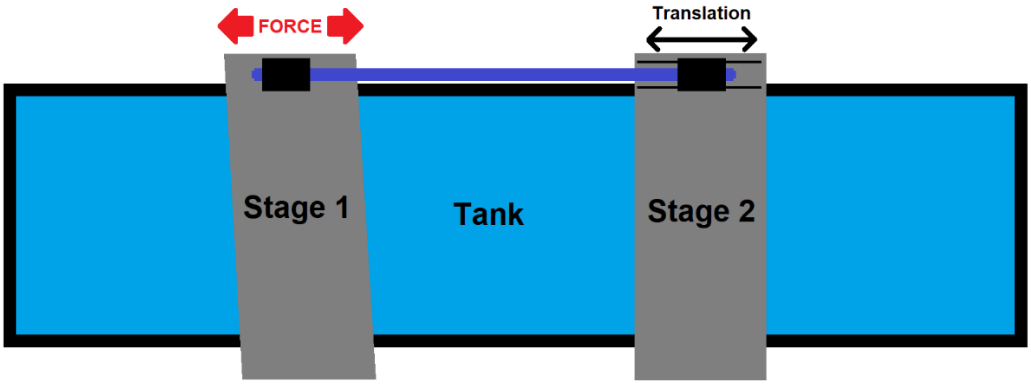


*Figure 4.32: Stage 1 lag during translation.*

Because the hydrophone is mounted to stage 1 and the transducer is mounted to stage 2, both in the centre, the distance between them might not be the same as the distance moved by the translation system. This is because the part of stage 1 close to the translation system mounting point will be moved smoothly on the rails, while the opposing part will only start moving when the stiffness of the stage itself forces it to move, causing hysteresis when translating. This can be prevented by always approaching a desired position from the same side, always cause the same amount of lag and therefore cancelling it out. This is why during the experimentation the stages were moved only 700 mm when the translation system is capable of 800 mm. In order to approach from the same side, the translation first needed to overshoot the desired position and come back. The order of positions and measurements were then, move to 0 mm and measure the delay, then move to 800 mm, then back to 700 mm and measure the second delay. Repeating this pattern makes it possible to take several measurements while ensuring the amount of lag stays the same. The exact magnitude of the lag was not measured but was noticeable by eye and probably on the order of magnitude of a few millimetres.

#### *4.4.3.3 Experiment and results*

The closest point to the transducer in the XY-Plane of the hydrophone was found using the method described in section 3.3.2. The delay was measured, the hydrophone translated 700 mm and measured again. This was done 10 times to see if the set-up was consistent and to get a better estimate of the speed by averaging.

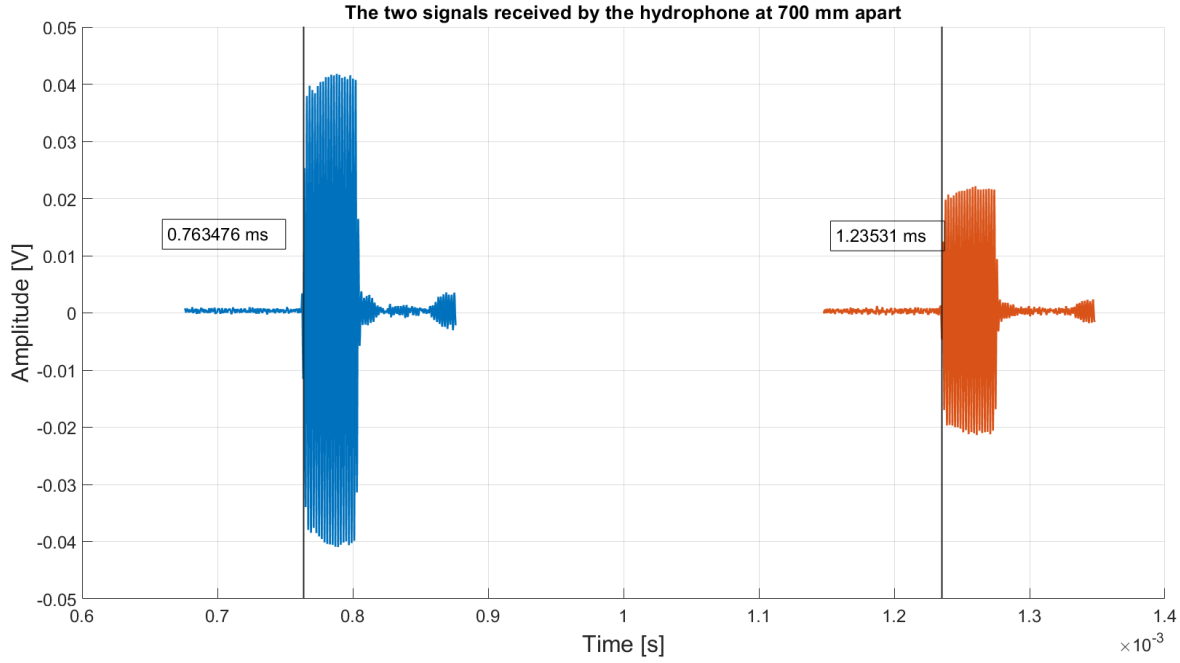


*Figure 4.33: Signal received by hydrophone at two distances.*

Above in Figure 4.33 is shown one of two of the measurements done by hydrophone. These were done with a translation of 700 mm apart. Using cross-correlation to find the start of each signal the

difference can then be found. The average timestamp for the first position and second positions are labelled and were $0.763476 \times 10^{-3}$ and $1.23531 \times 10^{-3}$ seconds respectively. Finding the sound speed is then only a matter of dividing the known translated distance by the difference in in signal arrival times.

$$c \approx \frac{0.7\ m}{(1.23531 - 0.763476) \times 10^{-3}\ s} \approx 1483.57\ m/s$$

*4.8*

*4.4.3.4 Diffraction correction*

When describing the factors involved in the delay between sending and receiving in formulae 12 and 13, a detail was left out. Other factors than the system delay may influence the measured time delay. A time correction term $t^c$ is therefore introduced.

$$t = \frac{L}{c} + t_s + t^c$$

*4.9*

This time correction factor includes effects of internal transducer reflections $t^{int}$, thermal and viscous boundary layers at reflection surface $t^{tv}$ and delay effects due to diffraction $t^{diff}$. For the purposes of this study, $t^{int}$ and $t^{tv}$ will be assumed to be negligible. The effects of $t^{diff}$ will however be investigated and is based on the work done in [17].

In the case of this experiment, diffraction of the sound wave in water results in a phase shift between the actual sound wave and a hypothetical plane wave. This shift in phase may result in a short time delay independent of the propagation time. If an accurate value for the sound speed is to be found, this needs to be corrected for. The adjusted formulae for the sound speed including the delay caused by diffraction is then:

$$t_1 = \frac{L1}{c} + t_s + t_1^{diff} \qquad t_2 = \frac{L2}{c} + t_s + t_2^{diff}$$

*4.10*

$$t_2 - t_1 = \frac{L2 - L1}{c} + (t_2^{diff} - t_1^{diff}) \qquad c = \frac{\Delta L}{\Delta t - \Delta t^{diff}}$$

*4.11*

The diffraction correction as defined by Khimunin [18] as

$$H^{diff} = \frac{\langle p \rangle}{p^{plane}}$$

*4.12*

Where $\langle p \rangle$ is the average pressure over the measurement are at a distance z in absence of the receiver, and $p^{plane}$ is the plane wave pressure at the same distance. This is a complex quantity with an amplitude and a phase. The phase of this quantity corresponds to the diffraction time shift, $t^{diff}$. Calculating this time shift will make it possible to correct for it in the sound speed calculations to get a more accurate measurement of the sound speed. The differential time shift is given by

$$t^{diff} = \frac{\angle H^{diff}}{\omega}$$

*4.13*

Where $\angle H^{diff}$ is the phase of the diffraction correction and $\omega = 2\pi f$ is the angular frequency of the sound wave.

Several models exist for calculating the diffraction correction. For this study the on-axis point receiver (piston model) [9] will be used, as it assumes a small measurement area such as a needle hydrophone on the sound axis, which is what this study uses. The expression can be written as

$$H^{diff}(ka, S) = 2sin\left[\frac{(ka)^2 S}{4\pi}\left(\sqrt{1+\left(\frac{4\pi}{Ska}\right)^2} - 1\right)\right] \times exp\left[i\left(\frac{\pi}{2} - \frac{(ka)^2 S}{4\pi}\left(\sqrt{1+\left(\frac{4\pi}{Ska}\right)^2} - 1\right)\right)\right]$$

*4.14*

Where $ka = \frac{\omega}{c}a$, $a$ is the radius of the transmitter and $c$ is the speed of speed. $S = \frac{z\lambda}{a^2}$, is a dimensionless quantity dependent on $\lambda = \frac{2\pi}{k}$, the radius $a$ and the distance between the transmitter and he receiver. Since the diffraction time shift is only dependant on the phase of $H^{diff}$, the rest of the equation will not be considered in this study. The time shift is then expressed as

$$t^{diff} = \frac{\frac{\pi}{2} - \frac{(ka)^2 S}{4\pi}\left(\sqrt{1+\left(\frac{4\pi}{Ska}\right)^2} - 1\right)}{\omega}$$

*4.15*

The phase shift, $\angle H^{diff}$, is plotted below up to 4 meters, the length of the tank. The values for the variables used in this study were, $a = 12.5\ mm$ , $f = 500\ kHz$, $c = 1483.57\ m/s$.

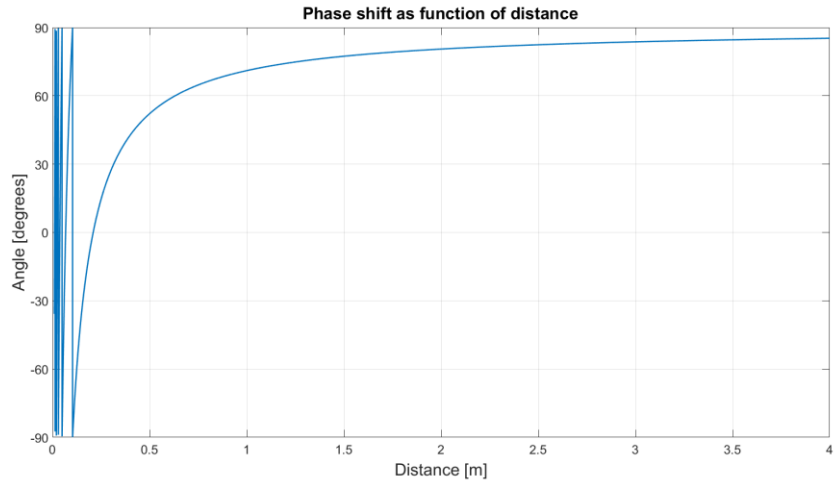


*Figure 4.34: Diffraction correction phase shift.*

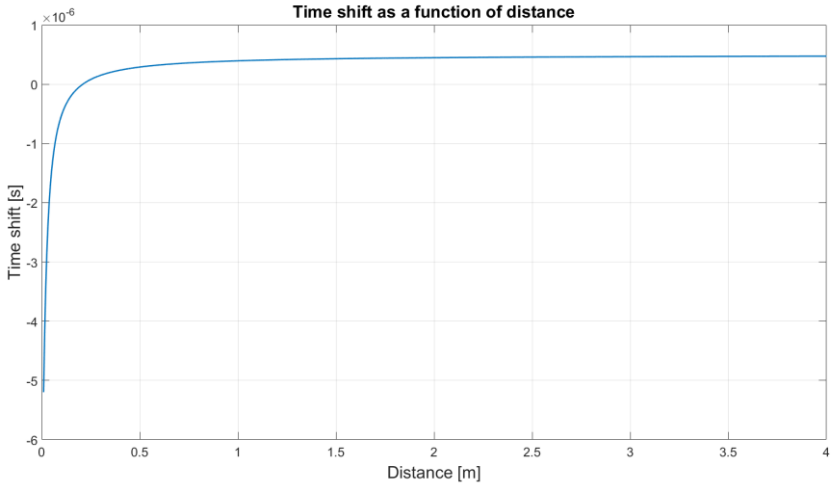


*Figure 4.35: Diffraction time shift.*

The phase shift close to the transmitter is more than ± 90°, making it wrap around. Both the phase and the time shift flatten out as the distance increases and go towards a final value. These values being 90° and $5 \times 10^{-7}$ seconds respectively.

An issue arises when considering the fact that the value for the time shift found is used to estimate the value of the sound speed in the medium, when one of the values need to calculate the time shift was the sound speed in the medium, $c$. This can be taken into account, but the contribution of $c$ to the magnitude of the time shift is very small. Changing $c$ from 1485 to 1500 m/s, changes the time shift at 1 meter from $3.948 \times 10^{-7}$ to $3.958 \times 10^{-7}$ seconds. a 0.35 % relative difference and a negligible absolute difference. Doing a hypothetical scenario where the sound speed is assumed to be of 1500 m/s and used to calculate the time shifts and having measuring points at z = 1 meter and z = 1.7 meters, the final value for $c$ after correcting for the newly calculated time shifts would be 0.0014 m/s lower

than if 1485 m/s was used instead. The magnitude of $c$ in the calculation of the time shift for the purposes of correcting the value of $c$ is negligible.

Finding $\Delta t^{diff}$ is now only a question of finding the time shift at the two distances the sound speed was measured at. Again, using $c$ to find an estimate for the absolute distance of the measuring points. Using $c = 1483.57\ m/s$, and the average timestamps found in section 4.3.2.2, the distances measured at were approximately:

$$z_2 \approx ct_1 = 1.1327\ m \qquad z_2 \approx ct_2 = 1.8327\ m$$

The respective time shifts are therefore:

$$t_1^{diff} = 3.947\ \times 10^{-7}\ s \qquad t_1^{diff} = 4.3805\ \times 10^{-7}\ s$$

And the final diffraction corrected value for the sound speed is:

$$c = \frac{\Delta L}{\Delta t - \Delta t^{diff}} = \frac{0.7\ m}{(4.7183 - 0.00043354) \times 10^{-4} s} = 1483.71\ m/s$$

*4.16*

*4.4.3.5 Discussion of sound speed*

Comparing the final value of the measured sound speed for the water in the experimental tank shows a significant difference in their values. The theoretical value being 1489.32 m/s at the average measured temperature of the water, and the measured value, after correcting for diffraction being 1483.71 m/s. The difference between them being 5.61 m/s or 0.38 %. The discrepancy may have several explanations, some are discussed here. In the calculation of the theoretical sound speed, a few assumptions were made. Their possible effects on the value of $c$ are investigated. All values connected to the gauge pressure $\wp_G$, those being the gravitational acceleration g, the depth under water h and the density of the water ρ, play a very little part in the end result for c. Omitting $\wp_G$ entirely from equation only changes the final value by 0.01 m/s. Investigating the possible effect of using the true density of water at 22.39 degrees Celsius, instead of 1000 kg/m$^3$, using a more accurate value for g at the experiments longitude and latitude, instead of 9.81 m/s and measuring the exact depth of the hydrophone in the water column is not necessary as the changes are negligible. The other assumption made was that the water was distilled, which the water in the experiment tank is not. The water is fresh water from the buildings water supply. The water also accumulates algae, dust, rust and other particles over time. The algae in particular become visually noticeable after a few months. The water is therefore changed once a year or so. The algae may play a large role in making the sound speed slower than theoretically expected. It is also worth noting that the sound speed experiments were done in February, shortly before the water temperature was monitored. The temperature of the water might have been slightly lower at this point due to the time of year. A water temperature of around 20.5 degrees Celsius would result in a theoretical sound speed comparable to the measured one.

Although the laboratory's temperature should be kept stable by the buildings temperature regulation systems. No clear indication of a rising temperature in the water can be seen by the measurements done in the time after the sound speed experiment. There may also have been oversight regarding the translation system, or the offset mentioned in section 4.3.3.2, making the actual distance travelled not the same as the value used in the calculations. This however is not likely an explanation, as any fault in the system or the offset is likely to make the distance shorter than the desired one, resulting in a calculated sound speed further from the theoretical one.

#### *4.4.3.6 Uncertainty*

Some assumptions must be made in order to find a value for the uncertainty of c. Assuming a working translation system and considering the offset discussed in section 4.3.3.2, the deviation is assumed to be no more than 1 mm to each side, giving a standard deviation of 0.5 mm. For the timing $\Delta t$, the largest error probably comes from the cross-correlation algorithm detecting the start of each signal. Considering the consistency in its detection seen in Figure 4.30 and Figure 4.31, estimating a deviation of no more than 10% of one wavelength. The uncertainty of $\Delta t^{diff}$ is difficult to guess, however the impact of the value towards $c$ is small, meaning overestimating the uncertainty will have little effect on the uncertainty of c. Considering the measurements took place outside the transducers Rayleigh distance but closer than infinitely far away, the value of $\Delta t^{diff}$ lies somewhere between 0 and $5 \times 10^{-7}$ seconds. This gives a maximum value for the uncertainty of $\Delta t^{diff}$ at $\frac{5\times10^{-7}}{2}$ seconds.

$$u\Delta L = 5 \times 10^{-4}\ m \qquad u\Delta t = \frac{0.1}{500\,000\ Hz} = 2 \times 10^{-7}\ s \qquad u\Delta t^{diff} = 2.5\ \times 10^{-7}\ s$$

$$uc = \sqrt{\left(\frac{\delta c}{\delta \Delta L} u\Delta L\right)^2 + \left(\frac{\delta c}{\delta \Delta t} u\Delta t\right)^2 + \left(\frac{\delta c}{\delta \Delta t^{diff}} u\Delta t^{diff}\right)^2} \qquad 4.17$$

$$uc = 1.4618\ m/s$$

The estimate for the uncertainty of the sound speed is based on many estimates but gives idea of the magnitude of the variations in the measured sound speed. Most of the uncertainty in the current estimate comes from the uncertainty in $\Delta L$. This makes sense as it is linked to the physical set-up of the experiment and only small error in its accuracy results in relatively large changes in c. Doubling the estimate for the uncertainty in the set-up, and therefore in $\Delta L$, practically doubles the value of $uc$.

## 4.5 System delay

In order to know the precise distances between a transducer and its target, a few things are needed, the time delay between transmitting and receiving of the signal, as well as the sound speed of the

medium. Using these two to calculate the actual distance however may give a faulty answer, as the time measured between transmitting a signal and receiving it may involve delays in the equipment used. This means that the time measured includes both the actual travel time of the sound wave, as well as a small delay caused by the transducer, filter, amplifier, or other parts of the set-up the electric signal travels through on its way from the signal generator to the oscilloscope. The timing on the oscilloscope starts from zero and is based on the sync signal from the signal generator. This is a separate signal sent by the signal generator such that other equipment can know when the bursts are sent, to the transducer in this case. See section 3.2 to see the equipment involved. The combined delay from signal being sent by the signal generator to a sound wave starts to propagate through the water, and the delay between the sound wave being registered by a hydrophone or transducer and being registered on the oscilloscope, is the system delay. Although the contributions to this delay from the different sources are hard to quantify individually, the combined delay can be measured.

### 4.5.1 Delay measurement method

Finding the system delay involves taking several measurements at different distances between transducer and target. The measured time delays plotted against the distances will be a linear function with an offset at 0. The physical interpretation of this offset is the delay between signal sending and receiving when the distance travelled by the propagating sound wave is 0. This will be the system delay. To perform this measurement, the absolute distance from transducer to target needs to be known. The experimental set-up has no mechanism to measure the absolute distance between the stages or any other objects. Only the relative distance can be changes using the translation stage. This was used to find the sound speed, however the absolute distance needs to be measured manually in order to find the system delay.

*Figure 4.36: Finding absolute distance from transducer face to determine system delay using a ruler.*

Using a ruler placed along the sound axis of the transducer in use, a starting distance of 31 cm in the case of the calibration sphere and 9 cm in the case of the hydrophone, was measured.

### 4.5.2 Measuring system delay

When measuring distances acoustically, it is important to isolate the propagation time of the sound in the medium. If other delays between signal transmission and reception are included, the calculated distance will be faulty. When sending a sinusoidal pulse from a signal generator to a transducer, there will be a slight time delay between the signal being sent from the generator to the soundwave starting to propagate through the medium in front of the transducer. There will also be a similar delay when using a hydrophone to receive the sound produced by the transducer. A delay between signal reception, detection, processing, and presentation. When using a calibration sphere, the delay from the transducer end will be doubled as it will now function as both the sender and the receiver. In addition, an analogue filter is used to increase signal to noise ratio. This will also delay the signal slightly.

In this work it is important to know this delay as it will directly affect the triangulation calculation where acoustically measured distances are the inputs. Not factoring in the delay will result in too large

distances and the final position of the target will be off. Finding the delays contributions from individual components in the system chain is difficult, but also unnecessary. The entire delay can be simply measured via two experiments. Firstly, the sound speed in the medium needs to be determined. This was done in section 4.4. Secondly, the time between signal sending and reception needs to be measured at several known distances from the sound source.

Finding the distance between two points in the experiment tank can be done by translating the stages by a known distance. However, this will only give the relative distance between the two chosen points. To determine the system delay, the absolute distance from the source is needed. This was done by moving the stage holding the transducer and the stage holding the target as close to each other as possible and then manually measuring the distance between the source and target with a ruler, seen in Figure 4.36: Finding absolute distance from transducer face to determine system delay using a ruler.. This method is not ideal and lends itself to many sources of measurement error but was determined to be the best option with the resources available. The distance was measured from the source to both a hydrophone and a calibration sphere in order to find the system delay in both cases. The distance from transducer to hydrophone was found to be 90 mm, and 310 mm for the tungsten carbide calibration sphere. These distances will be added to the relative distances measured using the translation of the stages to give the total absolute distance.

The second experiment was then performed at several distances with both types of targets. Time between sending and reception was measured, then the target was moved 10 cm further from the source. In case of the hydrophone, the total absolute distance would then be 9 cm plus n times 10 cm of relative translation. Making sure not to measure within the transducers near field. When knowing the time, distance and speed, the system delay can be extracted by comparing the time sound would have taken to cover the known distance, using the previously measured sound speed, and the actual measured time taken. The difference between the two is the system delay. Doing it as several distances ensures the experiment was done correctly as well as providing more data points for higher certainty of accuracy.

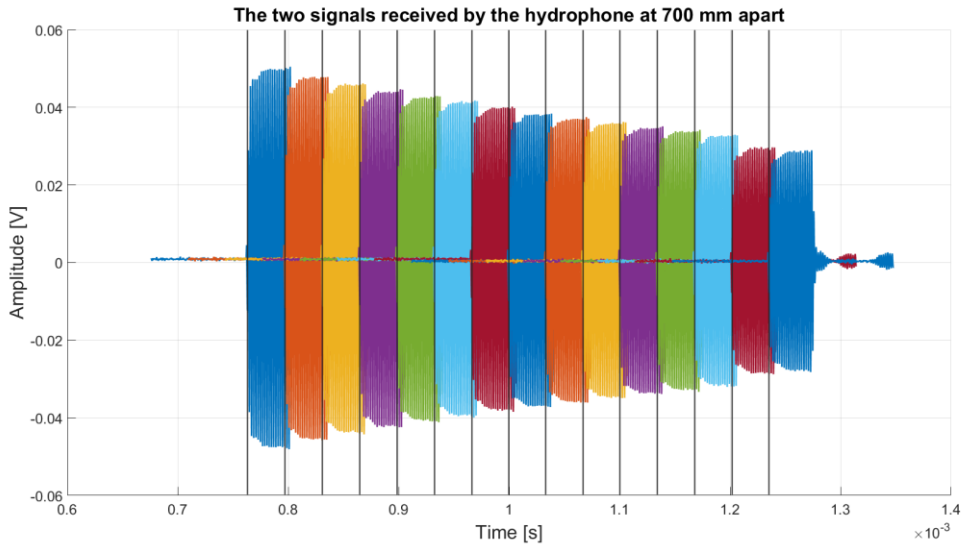


*Figure 4.37: Signals received by hydrophone from different distances.*

Finding the system delay is then only a matter of plotting the measured times against the absolute distances the times were measured at, then finding a linear line of best fit and finding where it crosses the y-axis. This represents the delay between signal sending and reception, with zero distance of sound propagation, also known as the system delay. This was done using MATLABs curve fitting tool and two different delays were found.

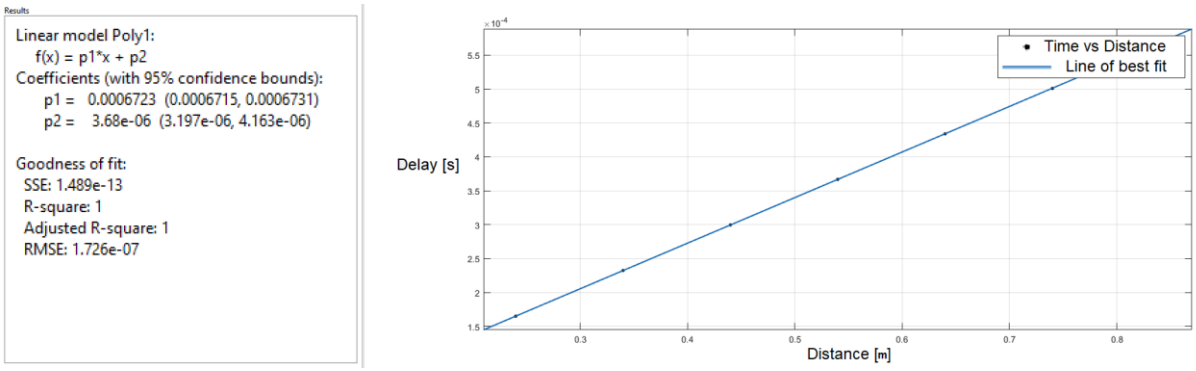


*Figure 4.38: Time vs distance for hydrophone.*

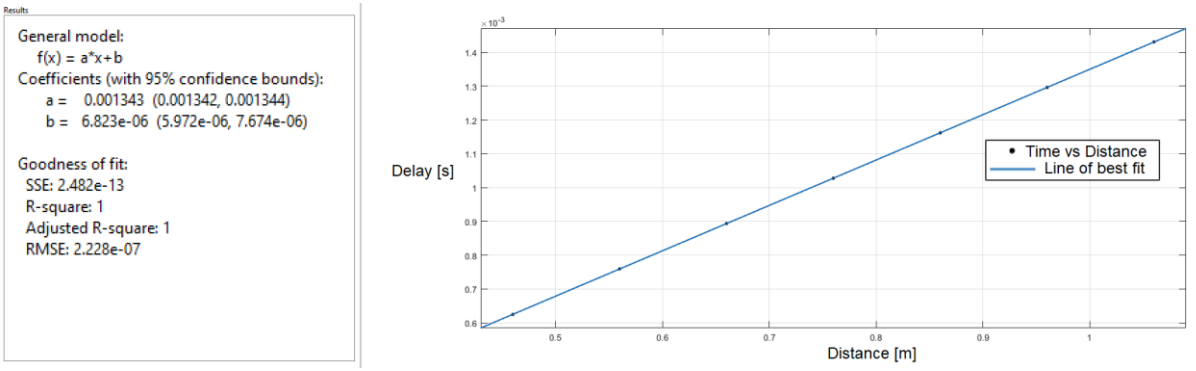


*Figure 4.39: Time vs distance for calibration sphere.*

The line of best fit was modelled with the formula $ax + b$, the b then representing the system delay. When using a hydrophone, the system delay was measured to be:

$$t_h = 3.68\ \mu s \qquad t_s = 6.82\ \mu s$$

with an uncertainty of:

$$u_{t_h} = 0.24\ \mu s \qquad u_{t_s} = 0.43\ \mu s$$

where $t_h$ is the system delay when measured with a hydrophone, and $t_s$ is the system delay when measured with a calibration sphere. The delay nearly doubles when using a calibration sphere instead of the hydrophone, which makes sense when assuming that most of the delay in such a system comes from the delay between converting between material vibrations and electric signal within the transducer. This happens twice when using a calibration sphere, as the signal is both sent and received by the transducer. In the case of the hydrophone, the transducer is only used for sending the signal.

It is also worth noting that the "a" in the modelled formula for line of best fit represents a value with the unit s/m, taking the reciprocal of this value will then give the sound speed in the medium. When this is done the resulting values for $c$ are:

$$c_h = \frac{1}{0.0006723\ s/m} = 1487.43\ m/s \qquad c_s = \frac{2}{0.001343\ s/m} = 1489.20\ m/s$$

It is hard to say if these values are any more or less accurate than the one found in section 4.4, but they do better align with the expected value for $c$ found using the theoretical model for distilled water. These experiments where also done about a month later than the sound speed measurement, and the temperature in the water may have changed in that time.

## 4.6 Triangulation and $\psi$-estimation

This section presents different methods of estimating the value of $\psi$ and what factors may affect it, with emphasis on the triangulation methods. For all experiments, the "origin" transducer will be transducer β, meaning, during this section, all experiments use transducer β when measuring, estimating and calculating anything related to beam pattern or $\psi$. This is done to ensure all results are comparable. A theoretical uncertainty and sensitivity analysis for the triangulation method is also performed via monte Carlo simulations.

### 4.6.1 Monte Carlo simulation

This section presents some simulations of the triangulation methodology by calculating a theoretical targets position with simulated uncertainties for many iterations. The following histogram for the results of the targets coordinates will tend toward the true uncertainty and distribution given the input parameters. A sensitivity analysis to explore the effect of each input parameter is also performed.

#### *4.6.1.1 Simulated uncertainty*

When triangulating a target point, as discussed in section 2.5, it is necessary to know 12 input values the 3 locators' x, y and z-coordinates and their distances to the target. All of which have some level of uncertainty. For this analysis, the positions of the locators will be chosen using the echosounder schematic for G.O. Sars, choosing three of the in total 7 transducer locations. In section 4.6.1.2 other combinations of positions will be used to investigate the effects on uncertainty of having a larger area between the locators. The positions chosen for this simulation is shown in Figure 4.40. As mentioned in section 2.5, doing a coordinate shift will decrease computation time significantly and will make large amounts of simulated iterations possible. The coordinates are therefore shifted to make T1 be placed in the origin and all three locators are on the XY-plane.

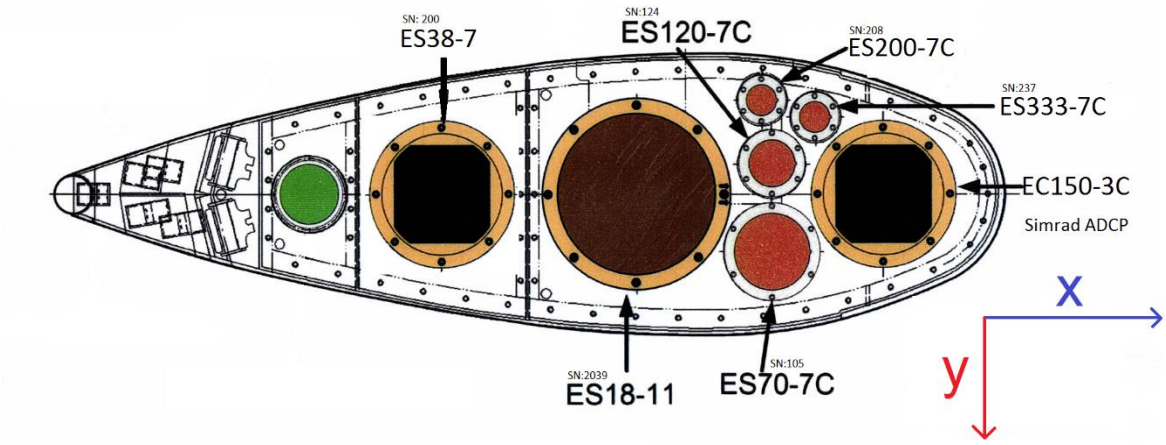


*Figure 4.40: Positions of echosounder transducers on G.O. Sars' drop keel.*

The transducers labelled ES200-7C, ES70-7C and ES38-7 are chosen as the locators for this simulation. Using their on-ship position and shifting the coordinate system making ES200-7C the origin transducer, the coordinates can then be written as

$$T_1 = ES2007C - ES2007C = (0, 0, 0)$$

$$T_2 = ES707C - ES2007C = (0.035, 0.524\ , 0)$$

$$T_3 = ES387 - ES2007C = (-1.138, 0.327, 0)$$

with all coordinates in meters. The position of the target is chosen to be directly underneath $T_1$, at 20 meters, a typical calibration depth [5]. The coordinates of the target are then,

$$S = (0, 0, 20).$$

The uncertainties involved were then chosen, these are not known values and their values were chosen for this simulation. The uncertainty in the position of all locators in all directions was set to be the same, $uT$, and the uncertainty in the distances, $ud$, was separated into an uncertainty in propagation time measurement and sound speed, $ut$ and $uc$.

$$uT = 1\ mm$$

$$ut = 1\ \mu s$$

$$uc = 1\ m/s$$

The position of the target $S$ was then calculated with each input parameter, locator position and distance to target, having a random variation chosen from a normal distribution with the standard deviation equal to the parameters chosen uncertainty, $uT$, $ut$ and $uc$. This process was repeated 100 000 times with each iteration having a different random variation in the input parameter. The resulting histograms are shown in Figure 4.41.

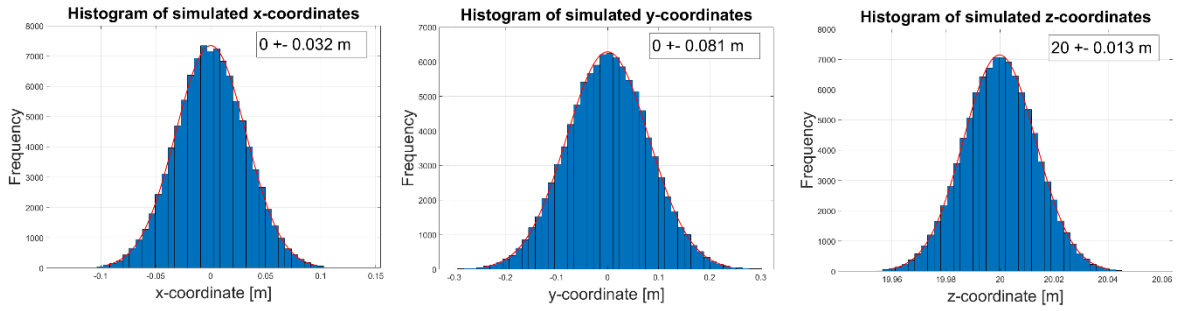


*Figure 4.41: Histogram of simulated target coordinates.*

The resulting histograms are also overlayed with a distribution function and the mean and standard deviation is written in the annotation. All three coordinates seem to have a gaussian distribution, assuming this, the resulting means and standard deviations are

$$uS_x = 0\ \pm 0.032\ m$$

$$uS_y = 0 \pm 0.081\ m$$

$$uS_z = 20 \pm 0.013\ m.$$

The uncertainty in the z-direction is smaller than in the x or y-direction and is a result of the geometry. When the target is placed far away compared to the distances between the locators, not any one parameter change will affect the z-coordinate much, but the x and y-coordinates become more sensitive to input-variations. This also plays into why the distribution of the z-coordinate does not seem gaussian. Any change in any one parameter will, almost always move the triangulated point closer to the locator plane and laterally in the x and/or y-direction. Only a combination of random increases in more than one distance parameter will change the estimated z-coordinate in the positive direction, making it less likely to be overestimated.

The uncertainty in the x-coordinate is also noticeably smaller than in the y-direction this is due to the area between the locators spans further in the x-direction than the y-direction giving better accuracy in the x-direction. This is shown in section 4.6.1.2.

With the chosen uncertainties of 1 mm, 10 µs and 0.1 m/s, the resulting coordinates have standard deviations of up to 0.8 meters, resulting in an equivalent of 2.3 degrees from the z-axis, which could prove significant when estimating the transducers beam patterns. In the y-direction alone, 5 % of the estimates were of by an equivalent of 4.65 degrees or more.

### *4.6.1.2 Sensitivity analysis*

By simulating the triangulation process while changing the uncertainties of the input parameters, the outcome's sensitivity to each input uncertainty can be found. For this study the uncertainties remain the same as in previous section above, but two of them will be set to 0, to see the effects of only one of the uncertainty parameters. All three cases are presented in Figure 4.42-Figure 4.44, each simulation with 10 000 iterations.

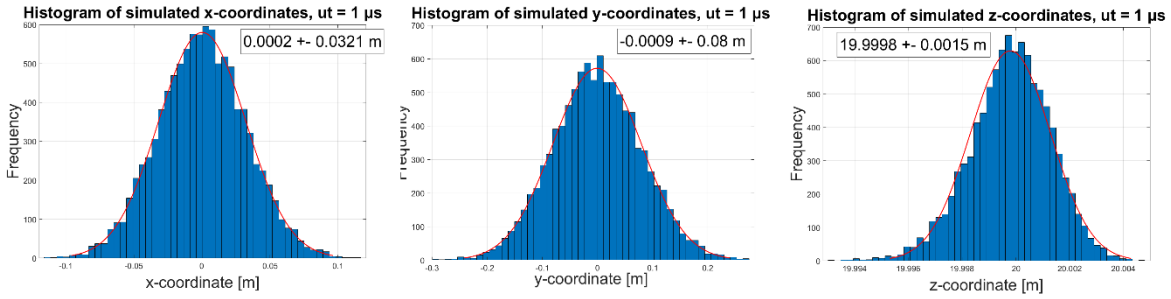


*Figure 4.42: Resulting histograms from monte Carlo simulated triangulation ut = 1 µs.*

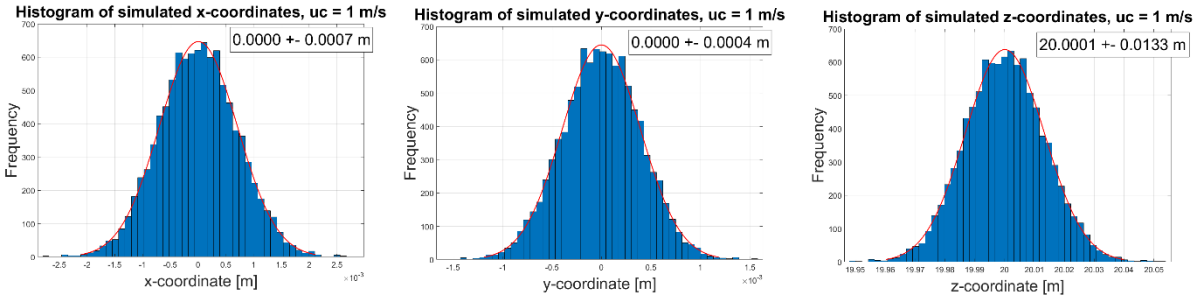


*Figure 4.43: Resulting histograms from monte Carlo simulated triangulation uc= 1 m/s.*

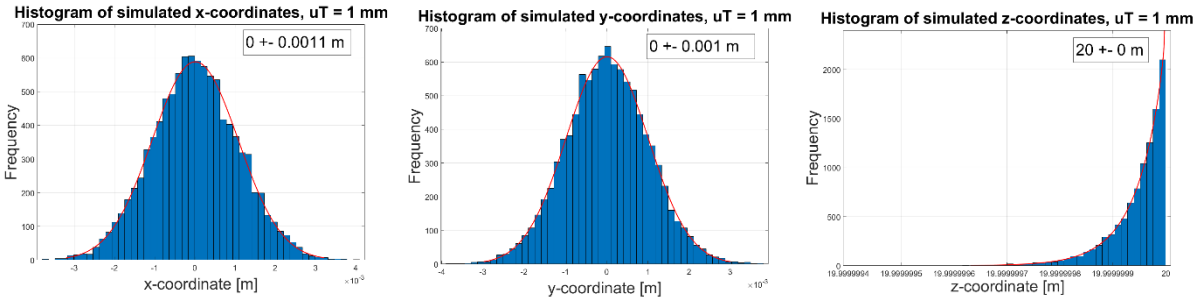


*Figure 4.44: Resulting histograms from monte Carlo simulated triangulation uT= 1 mm.*

The majority of uncertainty in the targets x and y-position in the case presented in 4.6.1.1 seems to come from its uncertainty in the propagation time $ut$, as seen in Figure 4.42-Figure 4.44. $uc$ contributes to most of the uncertainty in the targets z-position, as it affects all distance estimates equally, while $ut$ affects each distance estimate individually. @

The distribution of the simulated z-coordinate has a normal distribution when $uT = 0$, and while $uT \neq 0$ and $ut = uc = 0$, the distribution becomes a reverse exponential distribution. While the target point is directly below one of the locators, no change in either locator position results in a higher z-coordinate for the triangulated target, hence the cut off distribution. In certain combinations of input uncertainties where $uT$ is large enough compared to the other uncertainties involved, the distribution of the z-coordinates starts to take this skewed shape. This was simulated and is shown in Figure 4.45, using the input uncertainties set at

$$uT = 10\ mm, \quad ut = 10\ \mu s, \quad uc = 1\ m/s$$

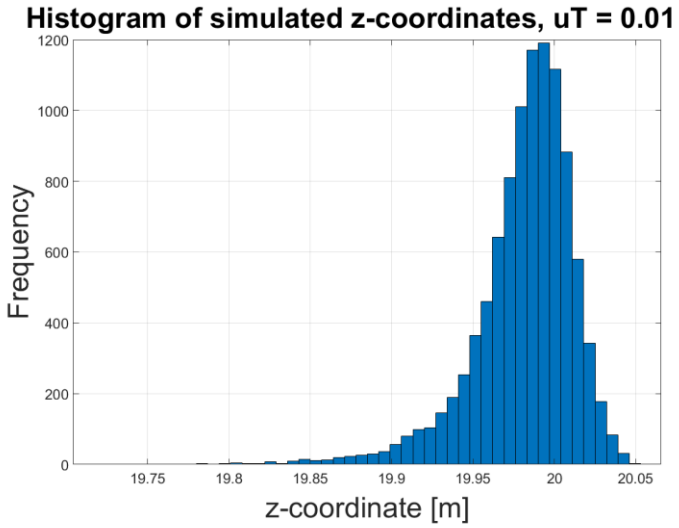


*Figure 4.45: Skewed histogram of simulated z-coordinate.*

#### 4.6.1.2.1 Locator positioning

By changing which three transducers used to triangulate the area between them will change, and this affects the accuracy of the coordinates of the triangulated target point. Using the same uncertainties as transducer positions as in as in section, and only changing locator $T_3$ from ES38-7 to ES18-11 as seen in Figure 4.40, the area between the three locators is now smaller in the x-direction and is now similar to the extension in the y-directions. The resulting simulated uncertainties are presented in Figure 4.46 with 10 000 iterations, with the locator positions

$$T_1 = ES2007C - ES2007C = (0, 0, 0)$$

$$T_2 = ES707C - ES2007C = (0.035, 0.524\ , 0)$$

$$T_3 = ES1811 - ES2007C = (-0.441, 0.327, 0).$$

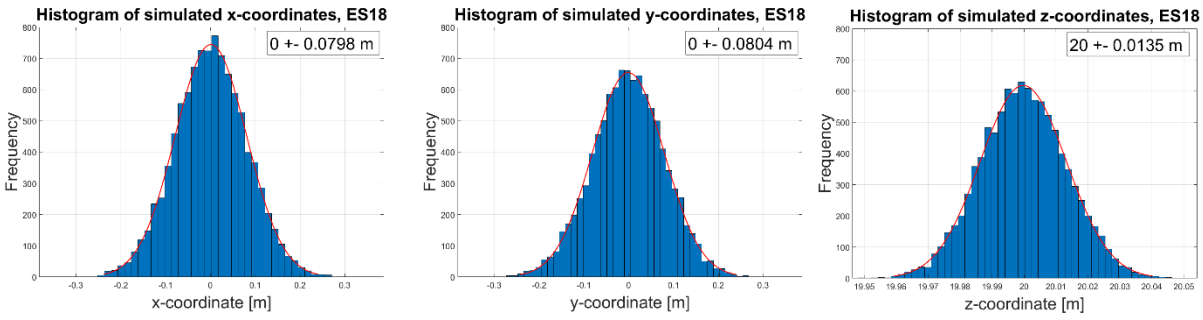


*Figure 4.46: Simulated uncertainties when decreasing area between transducers.*

With a more similar extension in both the x and y-direction, the uncertainties for the x and y-coordinates of the target are almost equal, while both the uncertainties of the y and z-coordinates remain the same as the previous case. Choosing locators as far apart as possible decreases inaccuracy dramatically in the case studied here. This is one important reason split beam triangulation is highly sensitive to uncertainties and may give faulty results.

The MATLAB code used for the monte Carlo simulations can be found in appendix A.4.

### 4.6.2 Single target triangulation testing

To test out the accuracy of the triangulation method using three transducers and one target, an experimental set-up was made. Two 500 kHz and one 1 MHz transducer were mounted to the transducer mounting plate in the positions 2, 5 and 7, see Figure 3.26. A 22 mm tungsten carbide calibration sphere was then suspended in the water some distance from the transducers, using fishing line in the IMR octant configuration. The three transducers were then supplied with a 500 kHz, 10 Volt peak to peak, 25 cycle signal, one at a time. The echoes received from the sphere were recorded and saved. Using the positions of the transducers and the distances measured from each transducer to the calibrations sphere, the exact position of the sphere could be calculated using the triangulation method.

#### *4.6.2.1 Finding the transducer positions*

Using the triangulation method requires knowledge of the positions of the transducers. The mounting plate has known dimensions, and this could be used to find the distances between the transducers, however it is desirable to define coordinate system to be parallel with the positioning system in the experiment tank. This will make it easy to know the position of the sphere for reference. For this reason, the positions of the transducers were found acoustically by moving the calibration sphere on a plane using the translation system.

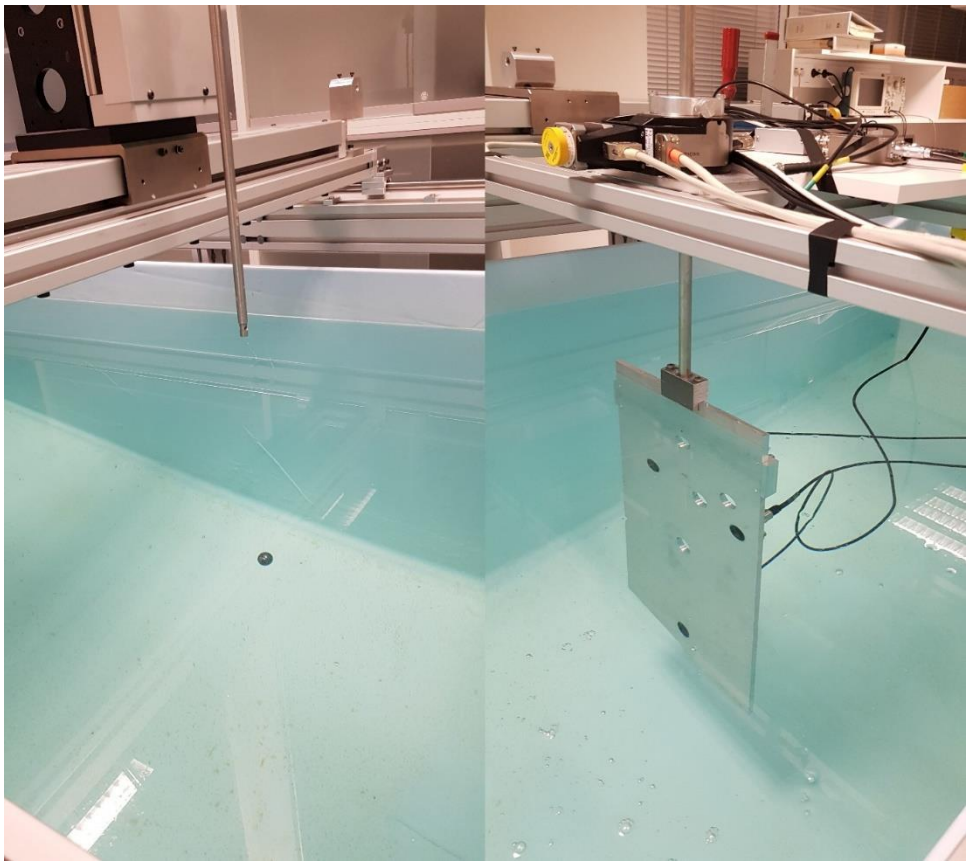

*Figure 4.47: Calibration sphere on one side of the tank, movable by the translation system and three transducers in the mounting plate at the other side.*

Using the methodology described in section 3.3.2. The point directly in front of each transducer, along the defines z axis, can be found by moving the sphere around and measuring the distances. Since the relative positions of the sphere are known via the positioning system, the positions of the transducers can also be found. Each transducer's position is the same as the sphere when it is at its closest point, minus the distance measured in the z-axis.

$$T_p = S_p + d_z = (x, y, z - d_z)$$

*4.18*

Where $T_p$ and $S_p$ are the positions of the transducer in question and the calibration sphere respectively, and $d_z$ is the distance between them on the z-axis. The sphere's x and y- positions are known because of the position system, the z-coordinate, however, must be defined. XY-plane defined by the translation system, meaning the plane the sphere is placed on, is defined as z = 0. This makes it so that the sphere will have coordinates $(x, y, 0)$. The x and y position can then also be defined as being zero at this point and the sphere is now defined as being at the origin. The three transducers will then have measured positions in relation to the origin and the exact position of the calibration sphere can now also be known for reference when triangulating.

#### *4.6.2.2 Finding the distances*

Finding the distance between transducer and sphere is a matter of signal detection. An algorithm needs to be used to find the signal, or echo, received by the transducer, from the calibration sphere. A cursor method cannot be used as the timing window is unknown as the position of the sphere is unknown. For this experiment the cross-correlation method described in section 3.3.1.4 was used. The position in time where the received signal best resembles the signal sent will be the time delay between signal sent and signal received. The system delay found in section 4.5 also used the same signal detection algorithm. The system delay will be part of the measured time delay and must be accounted for, so that the calculated distance used for triangulation is accurate.

#### *4.6.2.3 Knowing the sphere position*

In order to know if the triangulated position for the sphere is correct, we need to already know the spheres position via some other method. As described in section 4.4.1, if the transducers positions are defined using the tanks positioning system, then the position of the sphere can also be known. When both the triangulated position and the actual position of the sphere is known, the two can be compared. For this experiment, the origin was chosen to be the origin of the tanks translation system. This was chosen as these coordinates are the ones operating with when using the system and therefore no coordinate system conversion needs to be done. This means the origin is on the plane on which the calibration sphere can move, giving it a z-coordinate of 0. The exact physical position of the origin is not important as all the coordinates are only for comparison. The position of the sphere can then be chosen to be anywhere within the coordinates $(0, 0.15, 0)$ and $(0.5, 0.65, 0)$. The sphere shouldn't be placed outside these coordinates as it will then be placed too close to, or inside, the walls, surface or bottom of the tank.

#### *4.6.2.4 Finding the transducers' coordinates*

The positions of the three transducers were first measured via the method described in section 4.6.2.1 The value "b" in Figure 4.48-Figure 4.53 represent the coordinate of the transducer in question. The "a" represents its distance from the XY-plane where the calibration sphere is located.

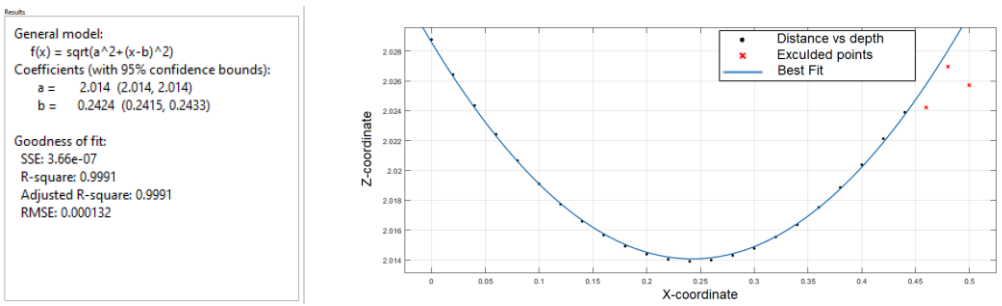


*Figure 4.48: Finding transducer 1 x-coordinate.*

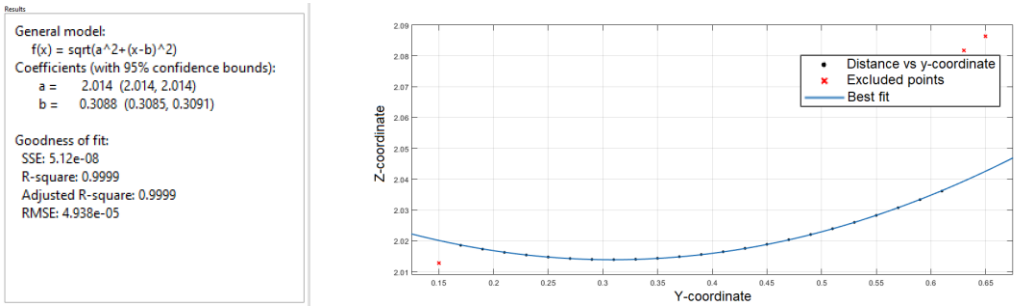


*Figure 4.49: Finding transducer 1 y-coordinate.*

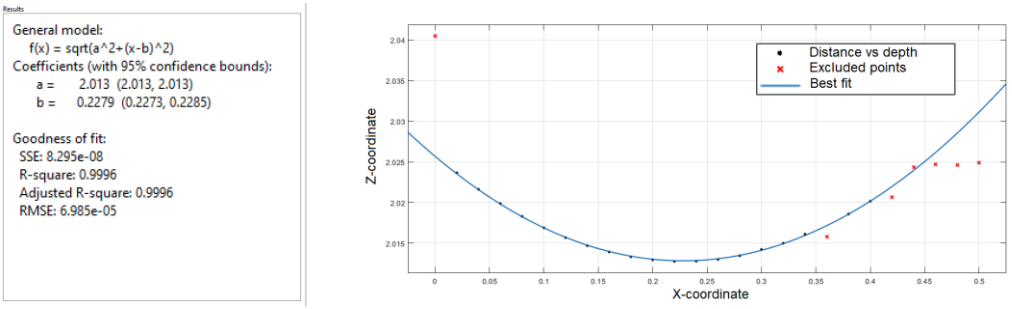


*Figure 4.50: Finding transducer 2 x-coordinate.*

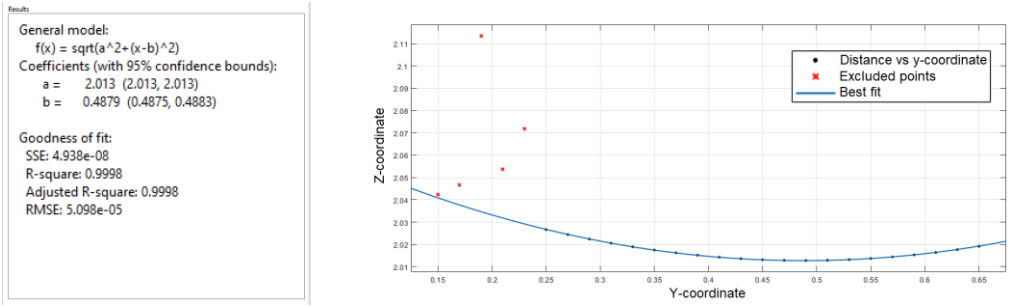


*Figure 4.51: Finding transducer 2 y-coordinate.*

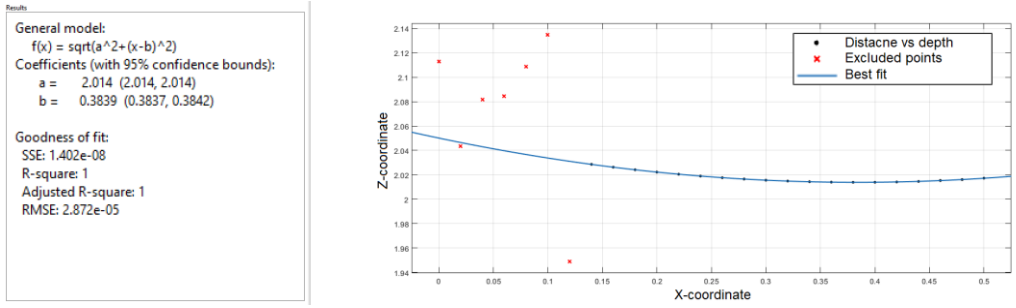


*Figure 4.52: Finding transducer 3 x-coordinate.*

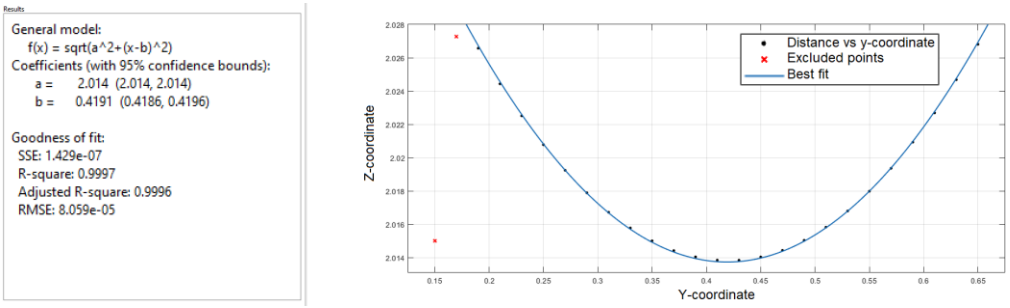


*Figure 4.53: Finding transducer 3 y-coordinate.*

The estimated positions of the three transducers are then:

$$T_1 = (0.2424, 0.3088, -2.014)\ T_2 = (0.2279, 0.4879, -2.0133)\ T_3 = (0.3839, 0.4191, -2.0138)$$

#### 4.6.2.4.1 Comparing the results

The calibration sphere was then placed, via the translation system, at the coordinates:

$$S = (0.34, 0.43.0)\ m$$

The distances between the three transducers were measured acoustically being sure to compensate for the system delay present when using a calibration sphere:

$$d_1 = 2.02\ m - \ t_s c = 2.0099\ m$$

$$d_2 = 2.0169\ m - \ t_s c = 2.0068\ m$$

$$d_3 = 2.0143\ m - \ t_s c = 2.0042\ m$$

The positions and distances found above can then be used in equations 2.15-2.17 to get a triangulated answer for the position of the calibration sphere. The equation gives two answers for the position. The answer containing a z-coordinate close to zero was selected, the other answer for the z-coordinate being ~ -4 m, and as we know the sphere is in front of the transducers. The result then becomes:

$$S_t = (0.337, 0.433, 0.01)$$

Comparing to the known position of the sphere, both the x and y-coordinates are off by 3 mm, while the z-coordinate is off by only 1 mm despite being the larger distance. This shows promise for the triangulation method as is its accuracy in this test was high.

### *4.6.2.5 Uncertainty*

Before finding the uncertainty of the coordinates for the calibration sphere, $S_t$ , the uncertainties for the all the variables used to find $S_t$ need to be determined, starting with the distances $d_1$, $d_2$ and $d_3$. These are based on the equation:

$$d = c(t - t_s) \qquad 4.19$$

Where $c$ is the sound speed, $t$ is the measured time delay between signal transmission and reception and $t_s$ is the system delay. Combining this formula with the uncertainties for $c$, $t$ and $t_s$ found in section 4.4 and 4.5, the uncertainty for $d$ can be found.

$$ud = \sqrt{\left(\frac{\delta d}{\delta c}uc\right)^2 + \left(\frac{\delta d}{\delta t}ut\right)^2 + \left(\frac{\delta d}{\delta t_s}ut_s\right)^2}$$

*4.20*

The same equation can also be used for finding $uT_z$, being the uncertainty of the z-coordinate for any given transducer, since this value is also based on a distance found with equation 4.19.

$$uT_z = \sqrt{\left(\frac{\delta d}{\delta c}uc\right)^2 + \left(\frac{\delta d}{\delta t}ut\right)^2 + \left(\frac{\delta d}{\delta t_s}ut_s\right)^2}$$

*4.21*

Uncertainties for the remaining variables $T_x$ and $T_y$, are not as straight forward to estimate, as they involve the uncertainty of the translation system as well as regression analysis. Using the same uncertainty for the translation system as used in section 4.4.3.6 and adding on the uncertainties for the regression analysis shown in Figure 4.48-Figure 4.53, a combined value for $uT_x$ and $uT_y$ can be found.

$$uT_x = uT_x = u\Delta L + uR_a$$

*4.22*

Where $u\Delta L$ is the uncertainty in the positioning of the translation system, found in section 4.4.3.6, and $uR_a$ is the uncertainty in the regression analysis, being one quarter of the 95% confidence interval, as it corresponds to two standard deviations in each direction.

The uncertainties doe all the variable involved in calculating $S_t$ are calculated to be:

$$ud_1 = 0.00209\,m \quad ud_2 = 0.00208\,m \quad ud_3 = 0.00208\,m$$

$$uT_1^x = 0.00095\,m \quad uT_1^y = 0.00065\,m \quad uT_1^z = 0.0021\,m$$

$$uT_2^x = 0.0008\,m \quad uT_2^y = 0.0008\,m \quad uT_3^z = 0.0021\,m$$

$$uT_3^x = 0.00065\,m \quad uT_3^y = 0.00075\,m \quad uT_3^z = 0.0021\,m$$

Combining the uncertainties to find the uncertainty in the triangulated coordinates of $S_t$ gives:

$$uS_t^x = \sqrt{\left(\frac{\delta S_t^x}{\delta d_1}ud_1\right)^2 + \left(\frac{\delta S_t^x}{\delta d_2}ud_2\right)^2 + \left(\frac{\delta S_t^x}{\delta d_3}ud_3\right)^2 + \left(\frac{\delta S_t^x}{\delta T_1^x}uT_1^x\right)^2 + \cdots \left(\frac{\delta S_t^x}{\delta T_3^z}uT_3^z\right)^2}$$

*4.23*

$$uS_t^y = \sqrt{\left(\frac{\delta S_t^y}{\delta d_1} ud_1\right)^2 + \left(\frac{\delta S_t^y}{\delta d_2} ud_2\right)^2 + \left(\frac{\delta S_t^y}{\delta d_3} ud_3\right)^2 + \left(\frac{\delta S_t^y}{\delta T_1^x} uT_1^x\right)^2 + \cdots \left(\frac{\delta S_t^y}{\delta T_3^z} uT_3^z\right)^2}$$

*4.24*

$$uS_t^z = \sqrt{\left(\frac{\delta S_t^z}{\delta d_1} ud_1\right)^2 + \left(\frac{\delta S_t^z}{\delta d_2} ud_2\right)^2 + \left(\frac{\delta S_t^z}{\delta d_3} ud_3\right)^2 + \left(\frac{\delta S_t^z}{\delta T_1^x} uT_1^x\right)^2 + \cdots \left(\frac{\delta S_t^z}{\delta T_3^z} uT_3^z\right)^2}$$

*4.25*

$$uS_t^x = 0.0485\ m \quad uS_t^y = 0.0463\ m \quad uS_t^z = 0.00222\ m$$

It is worth noting the significant difference in the magnitude of $uS_t^z$ compared to $uS_t^x$ and $uS_t^y$. This is likely because the any small variation in the distances $d_1$, $d_2$ and $d_3$ will change the position of $S_t$ in the XY-plane by a comparatively large amount, while the z-coordinate will remain almost constant as it is denoting the distance from transducer to target. If the target change position by a few cm in the XY-plane the change in the distance from transducer to target is miniscule. From the perspective of transducer 3, is the target directly in front of the transducer and is then moved in the Y-direction by 10 cm, the resulting change in the distance from transducer to target only changes by 2.5 mm. The configuration of the transducers compared to the relative distance of the target makes it more sensitive to changes in the z-direction then in the XY-plane. If the area between the transducers was increased compared to the distance of the target. The three uncertainties would be lower and closer to each other in magnitude. This is discussed in section 4.6.1.2.1.

The uncertainties of the x and y-coordinates for the target are comparatively large considering the size of the main lobe at that distance for instance. Using the piston model, the main lobe of the transducers used at a distance of 2 meters has a radius of $\tan(8.32°) \times 2\ m = 0.292\ m$. Trying to measure an area of that size with an uncertainty that large is not ideal, as an amplitude measurement at any point of the beam pattern may be falsely attributed to a different part of the beam pattern, making the estimate of $\psi$ potentially inaccurate.

Perhaps the assumptions made in the uncertainties were higher than in reality. Comparing the calculated uncertainty to the result in section 4.6.2.4.1, comparing $S$ to the triangulated position $S_t$, the results were much closer than the uncertainties predict. This may of course be by chance, doing a larger scale experiment might reveal more.

### 4.6.3 Choosing a curve fitting equation for transducer beam pattern estimation

In order to be able to integrate over the beam pattern to find a value for $\psi$, an estimate for the transducers beam pattern is found via MATLABs curve fitting tool, using a custom fitting equation. This equation was chosen based in the piston model approximation of a transducers beam pattern as well as the observations done during the bafflement testing in section 4.3.4 and can be expressed as

$$B_e(\varphi) = \left|\frac{2J_1(v)}{v}\right|^{\gamma} \qquad v = ka\,sin(\varphi)$$

*4.26*

where $\varphi$ is the angle from the sound axis and is the function variable, while $ka$ is a parameter. The Curve Fitting Tool will change these parameters in the given equation numerically until a curve of best fit is found.

The other parameter introduced is $\gamma$, used to compensate for the lowered side lobe levels observed when baffling transducers. If $\gamma$ is above 1 the resulting beam pattern will have lower amplitudes at all points other than the sound axis. The curve fitting algorithm will combine a value for $\gamma$ with a new $ka$-number to fit the beam pattern of the transducer. $ka$ is then no longer a representation of the wavenumber multiplied by the face radius but is used as an otherwise nameless variable used to find the best fit for the beam pattern.

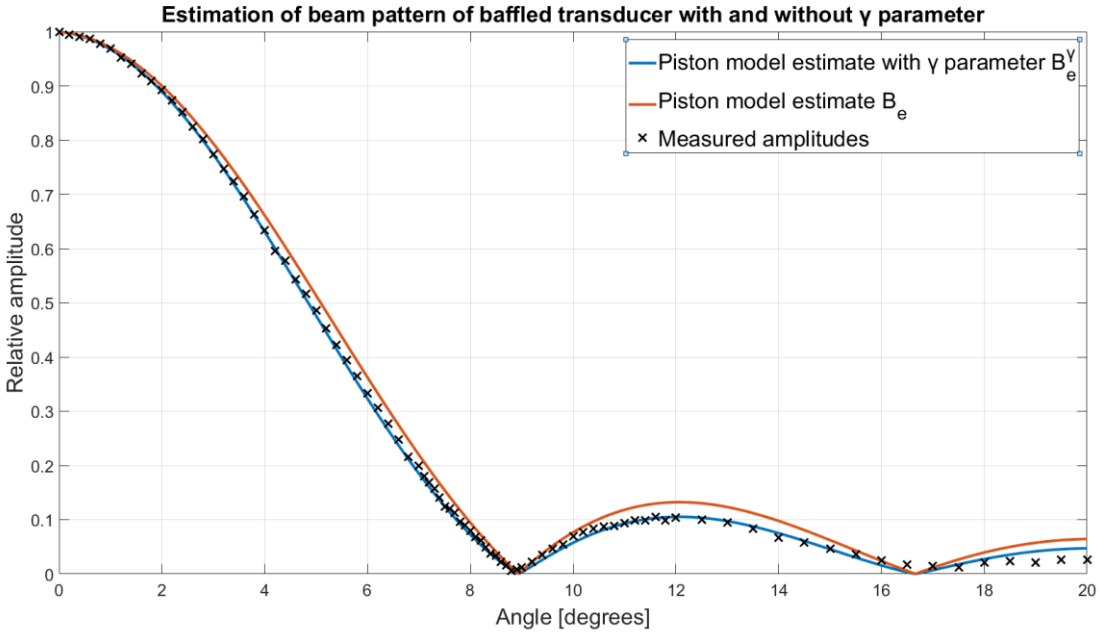


*Figure 4.54: Estimation of beam pattern of baffled transducer with and without γ-parameter, based on piston model.*

Figure 4.54 shows the improved estimate for the beam pattern of a baffled transducer by introduction of the $\gamma$-paramter, in this case using the 12 cm baffle. The unaltered estimation derived from the piston model fails to account for the lowered side lobes and altered shape of the main lobe. The $\gamma$-paramter will be used to get a better estimate of the beam pattern of the transducers in this study.

In the ICES report [5], a model of the beam pattern is proposed and is expressed as

$$\mathrm{b}(\alpha,\beta)^2 = 10^{0.60206\left(\left(\frac{2\alpha}{\alpha_{-3\,\mathrm{dB}}}\right)^2+\left(\frac{2\beta}{\beta_{-3\,\mathrm{dB}}}\right)^2-0.18\left(\frac{2\alpha}{\alpha_{-3\,\mathrm{dB}}}\right)^2\left(\frac{2\beta}{\beta_{-3\,\mathrm{dB}}}\right)^2\right)},$$

*4.27*

where α and β are the angles in the alongship and athwartship directions and $\alpha_{-3\,dB}$ and $\beta_{-3\,dB}$ are the -3 dB beamwidths in the α and β directions. This model will not be used during this study as the model only models part of the main lobe, while this study aims to model side lobes as well for better $\psi$-estimation. Figure 4.55 shows the cross section of the beam pattern estimated using equation 4.27 in the α direction using $\alpha_{-3\,dB} = \beta_{-3\,dB} = 7°$ compared with the piston model's beam pattern estimate using the same beamwidth.

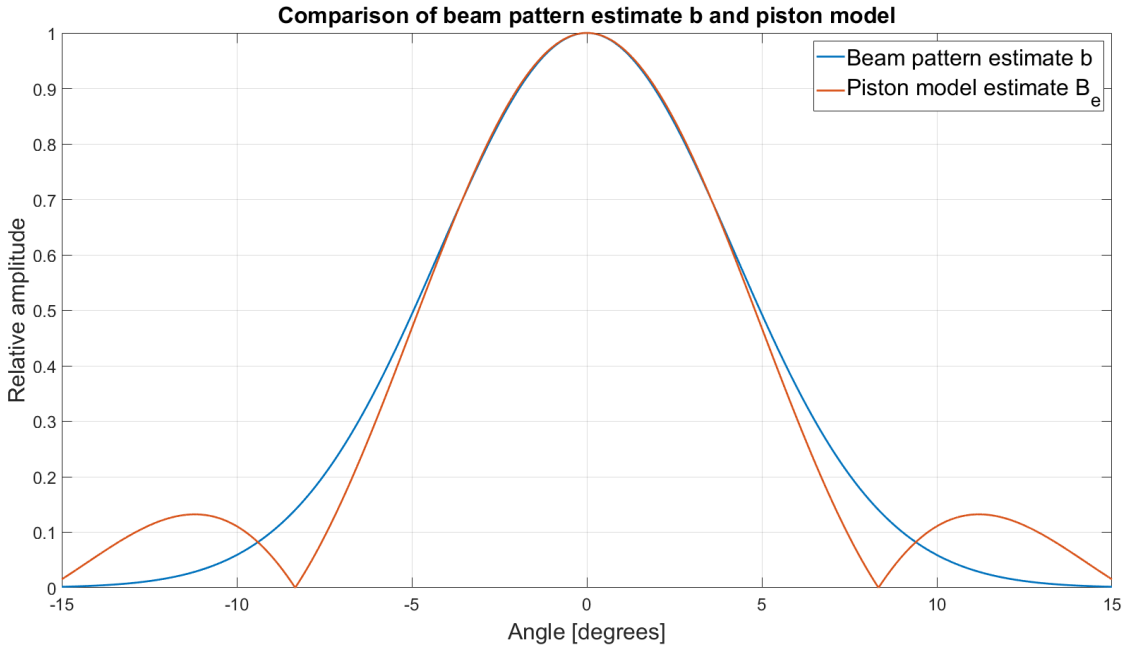


*Figure 4.55: Comparison of beam pattern estimate b and piston model.*

The figure above shows the discrepancy in equation 4.27 compared to the beam pattern estimated by the piston model, for angles higher than a few degrees.

### 4.6.4 Multi target triangulation testing with hydrophone

The same experiment as described in section 4.6.2 was performed using a hydrophone and recording the signal from the transducer at several locations. A hydrophone was used to better be able to test the triangulation method by removing some variables and also achieving a higher signal to noise ratio, therefore being able to record over a large area as more of the signals further from the sound axis could be detected over the noise. One of the transducers were also swapped for a 1 MHz transducer, this was done as only two 500 kHz transducers were available at the time, as well as being an opportunity to test the methodology for several frequencies and beam patterns.

Using the same coordinate system definitions as in section 4.6.2. The hydrophone was moved between the Y-coordinates 0.15 and 0.645, and between the depths of 0 and 0.48, with 0.015 m between the positions. This makes for an array of dimensions 33x34, containing all together 1122 positions, all with measured distances and amplitudes from the three transducers, which are still placed in the positions

2, 5 and 7, see Figure 3.26, on the mounting plate. The experiment was done in three phases, each phase having one of the transducers transmitting a 25 cycle, 10 Vpp electric signal every 10 ms. The hydrophone is placed in each position and averages the sound signal it receives over a time of 60 seconds to achieve the best signal to noise ratio before being moved by the translation system to its next location. After having cycled through all 1122 positions and recording the signals from the transducer, the transducer in use is then changed to one of the other transducers placed in one of the other sockets on the mounting plate. The whole procedure is then done again for this transducer. This is done three times, once for each transducer. Then the amplitude of the signal and distance from each transducer at each location has been recorded. This information can then be used to triangulate the hydrophones position and map each transducers beam pattern.

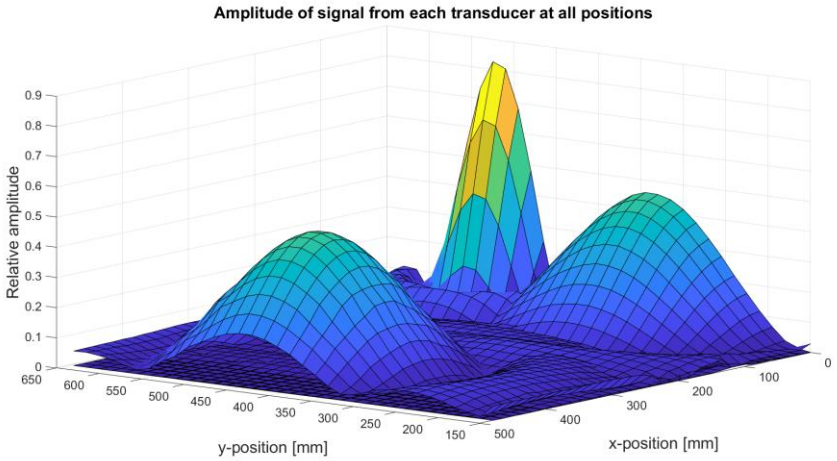


*Figure 4.56: Amplitude of signal picked up by hydrophone from the three transducers at all positions.*

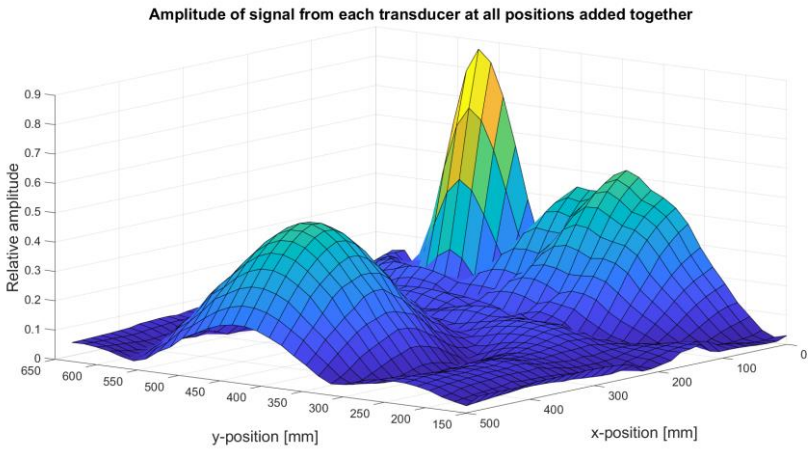


*Figure 4.57: Amplitude of signal picked up by hydrophone from the three transducers at all positions added together.*

In Figure 4.56 and Figure 4.57, the amplitudes of the signals coming from the three transducers in the 1122 positions have been plotted, showing the effects of the beam patterns of the three transducers. Since the hydrophone is not equidistant from the transducer at all measurement points, therefore, Figure 4.56 doesn't show the beam patterns exactly.

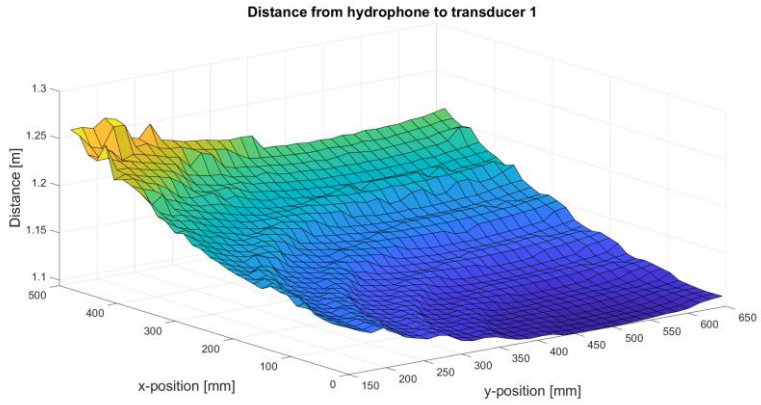


*Figure 4.58: Measured distance from Transducer 1 to hydrophone.*

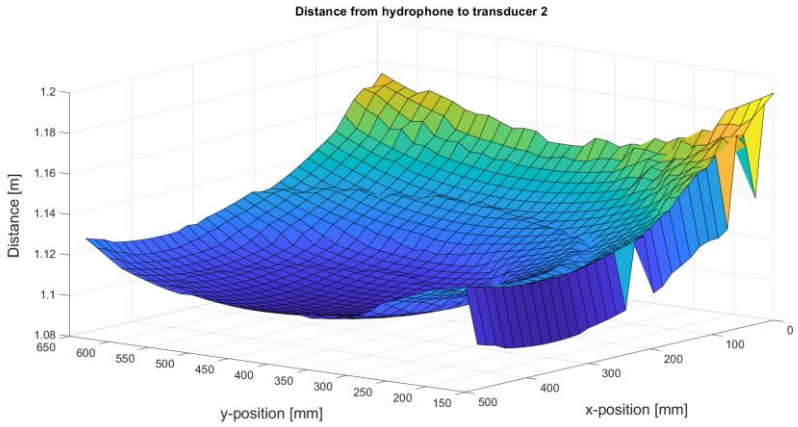


*Figure 4.59: Measured distance from Transducer 2 to hydrophone.*

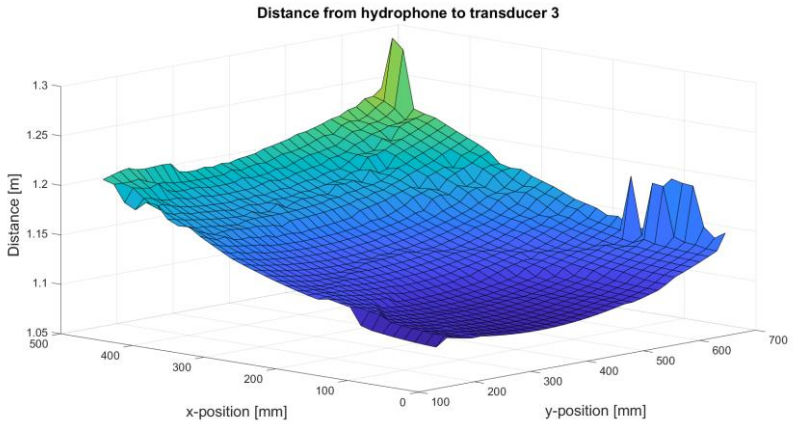


*Figure 4.60: Measured distance from Transducer 3 to hydrophone.*

In Figure 4.58, Figure 4.59 and Figure 4.60 the distances between the hydrophone and the three transducers are shown. Note the outliers with higher or lower values than expected. These occur at the edges of the measurement area, either because of low signal to noise ratio, making it difficult to find the exact distance or interference from wall reflection altering the apparent arrival time. These outliers will be excluded further in the study as any point triangulated by using only one faulty distance will also faulty. Using the measured distances with the x, y and z-coordinates of the transducers, the

position of the hydrophone at all points can be found. The positions of the transducers are chosen as the coordinates of their locations on the mounting plate, see section 3.2.1.1. The CAD-model has the coordinates for each mounting hole which is then used as the transducer's positions. By defining one of the transducers as being the origin the others get their coordinates from there.

$$T_1 = (0, 0, 0) \quad T_2 = (0.38, -0.112, 0) \quad T_3 = (-0.392, 0.069, 0)$$

Proceeding to use the triangulation method discussed in section 2.5 the result is a field of triangulated points in space with each having an $x$, $y$ and $z$-coordinate as well as a corresponding amplitude as measured by the hydrophone and found by Fourier-transformation via the method discussed in section 3.3.3. With this the field of points is plotted in Figure 4.61.

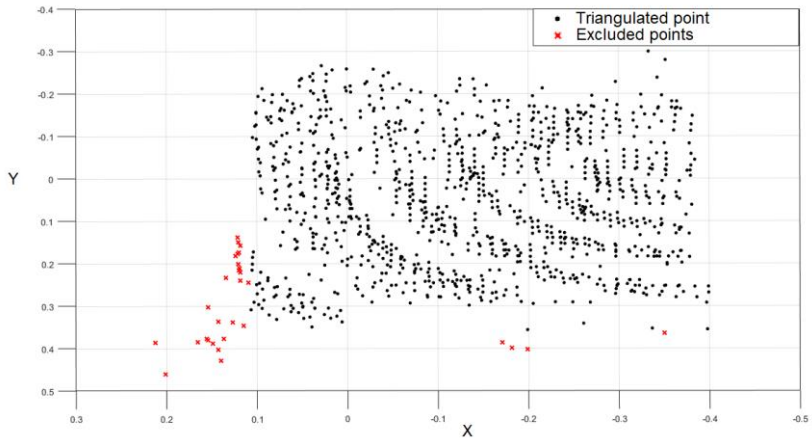


*Figure 4.61: All triangulated points at their x and y-coordinates [m].*

Figure 4.61 presents a 2-dimensional view of the points as their x and y positions were triangulated. Some of the points have been excluded as discussed earlier. Bad signal to noise ratios can make it impossible to detect the true arrival times of the echo to just one of the transducers, making the resulting triangulated position faulty. Since the measurement area in which the hydrophone was moved is known, any point outside this area is excluded for analysis purposes. A phenomenon worth noting is the apparent ripples or waves the points seem to group around. The ripples seem to have their origin at the position of transducer 1, the 1 MHz transducer. The reason for this is unknown but perhaps has something to do with the points being far outside transducer 1's main lobe and the signal from it has a low signal to noise ratio, as the ripples seems to contour around the beam pattern of transducer 1. If this is the case, it may be that the points that should have been detected around the dips in transducer 1's beam pattern have had too low signal to noise ratios and therefore been falsely positioned elsewhere by the triangulation. The excluded point in Figure 4.61, may be the falsely positioned points around the dips in transducers 1's beam pattern.

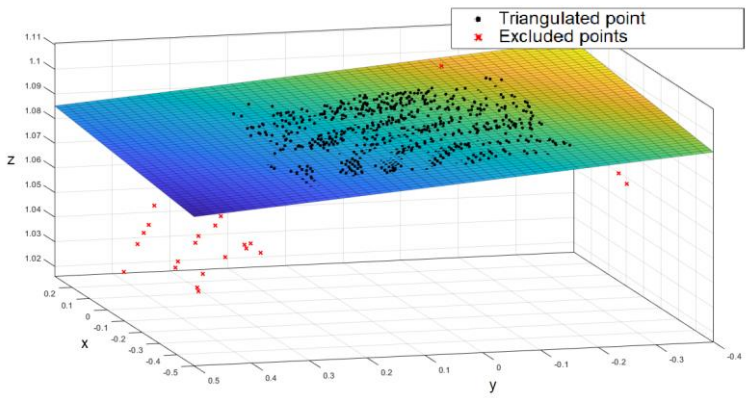


*Figure 4.62: All triangulated points at their x, y, and z-coordinates [m].*

The same points are, in Figure 4.62, plotted in 3D-space with a plane of best fit also plotted. The excluded points are more clearly faulty in this Figure as they z- coordinates are much lower than expected as well as being outside the measurement area. The extrapolated plane is not parallel with the XY-plane, meaning that the measurement plane the hydrophone was moved in was not parallel with the plane defined by the three transducers. The non-parallelity of the planes was expected and the difference is only minor and should not affect any results. The two planes were not aligned in the set-up process, partly to test the robustness of the experiment and see if a misalignment could be detected.

The x and y-coordinate of any given triangulated point can be translated into the angle between the z-axis and the vector between the point and the transducer in the origin, in the x and y-direction. The expression for these angles can be written as

$$\theta_x = \tan^{-1}\frac{x}{z} \qquad \& \qquad \theta_y = \tan^{-1}\frac{y}{z} \tag{4.28}$$

where $x$, $y$ and $z$ are the x, y and z-coordinates of the point. This being relative to the transducer, which in this case is in the origin, making no need for a correction. The amplitude measured at each point can then be plotted as a function of these angles.

Using the angles $\theta_x$, $\theta_y$ and their corresponding amplitudes, the beam pattern of the transducer can be plotted and estimated. However, the points are all not the same distance from the targets and the amplitudes need to be adjusted accordingly [1]. The amplitude connected to each point is then

$$p_a = p_m\, r, \tag{4.29}$$

where $p_a$ is the distance adjusted pressure amplitude, $p_m$ is the measured pressure amplitude at the point in question and r is the distance from transducer to this point. Doing this for all points will ensure

the pressure amplitudes are no longer distance dependant and they can now be compared and be used to plot the beam pattern.

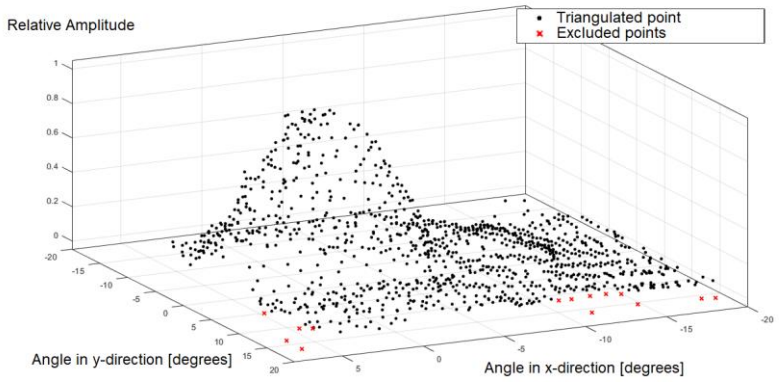


*Figure 4.63: All triangulated points at their angle in the x and y direction with the measured relative amplitude as the z-coordinate.*

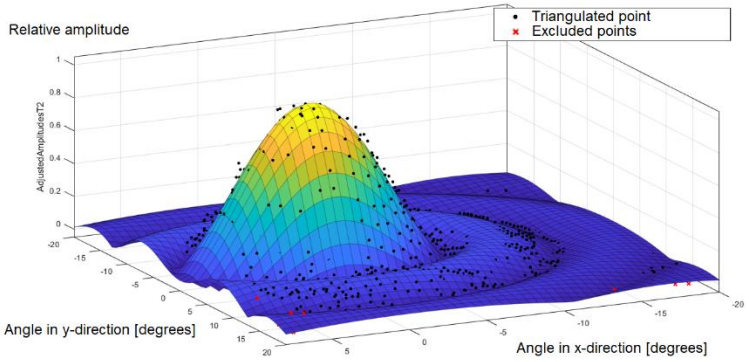


*Figure 4.64: All triangulated points at their angle in the x and y direction with the measured relative amplitude as the z-coordinate, with an extrapolated beam pattern.*

In Figure 4.63 and Figure 4.64 each point has been plotted at their $\theta_x$ and $\theta_x$-positions as well as a z-coordinate corresponding to the corrected amplitude measured at that point found via equation 4.29. In the latter Figure 4.64 a curve has been fitted to the points. This was done using MATLABs Curve Fitting Tool and the custom equation function was used.

Doing the curve fitting analysis using equation 4.26, the resulting curve as seen in Figure 4.64 is

$$B_e(\theta_x, \theta_y) = \left|\frac{2J_1(v)}{v}\right|^{1.053} \qquad v = 26.37\, sin\left((\theta_x + 0.384)^2 + (\theta_y - 0.123)^2\right)$$

with an R-squared of 0.871.

The value for $ka$ found to give the best fit was 26.37 and $\gamma = 1.053$. This estimated beam pattern can then be integrated over in order to find a value for the two-way beam solid angle, $\psi$. The interpretation of the introduced variables $n$ and $m$ is as a correction factor for the angle of the sound axis. Without them the sound axis would be assumed to be parallel with the z-axis, which is not necessarily the case,

making the resulting estimation for the beam pattern inaccurate. Knowing the offset of the sound axis of the transducer may also be of interest.

A different way of estimating the beam pattern is by converting the triangulated coordinates of every point into spherical coordinates $\theta$, $\varphi$ and $r$.

$$\theta = \tan^{-1}\frac{y}{x} \qquad \varphi = \cos^{-1}\frac{z}{r} \qquad r = \sqrt{x^2 + y^2 + z^2}$$

*4.30*

The angle between the z-axis and the vector from the origin transducer to any given point will then be

$$\alpha = 2\pi - \varphi$$

*4.31*

as $\varphi$ is the elevation angle from the XY-plane.

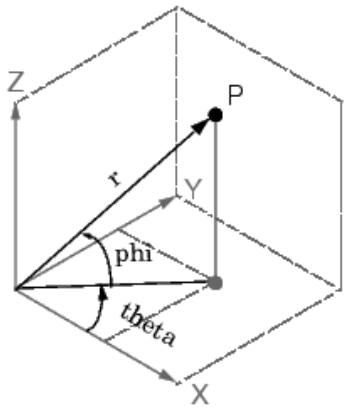


*Figure 4.65: spherical coordinates.*

The amplitude at every point can then be plotted as a function of the directivity angle $\alpha$ and an estimate of the directivity can be found.

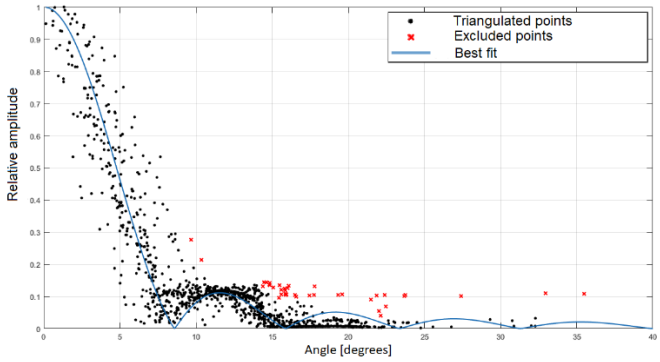


*Figure 4.66: all amplitudes plotted as a function of angle $\alpha$.*

Figure 4.66 shows the relationship between the angle from the z-axis and the amplitude of the signal picked up by the hydrophone at each location, showing the effects of the beam pattern. A curve has

been fitted to the dataset as an estimate of the beam pattern. Equation 4.26 is also used for the basis of this analysis as the curve of best fit is expressed as

$$B_e(\alpha) = \left|\frac{2J_1(v)}{v}\right|^{\gamma} \qquad v = ka\ sin(\alpha)$$

*4.32*

The curve fitting results in a $ka$-number of 26.38, $\gamma = 1.085$ with a R-square of 0.8666. This method does not in its current state however compensate for the sound axis not being parallel with the z-axis, as the $n$ and $m$ parameters did for the 3-dimensional method and will not be used to estimate $\psi$ in this thesis. It does however give a good visual representation of the beam pattern estimate.

Since this experiment was done under controlled conditions, the actual position of the hydrophone was known. Therefore, the real, as opposed to triangulated, directivity angle $\alpha$ can be used when plotted against the measured amplitude at each point. The resulting plot is shown in the plot below.

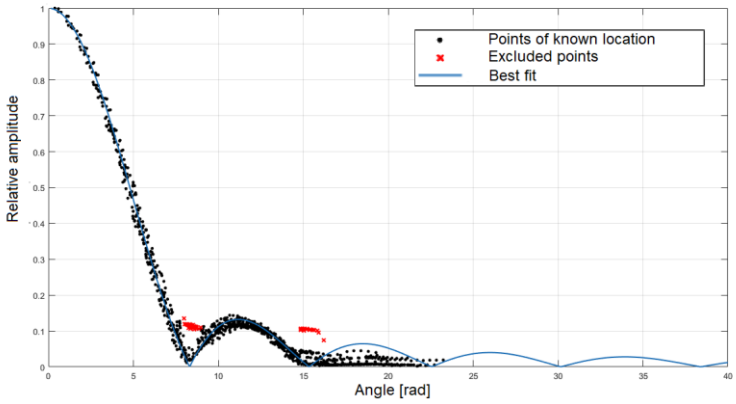


*Figure 4.67: All amplitudes plotted as a function of angle α at known locations.*

Figure 4.67 shows the amplitudes measured at each hydrophone location against that positions angle from the sound axis $\alpha$. The curve fitting results in a $ka$-number of 26.5, $\gamma = 1.063$ and with a R-square of 0.987. The positions in the Figure 4.67are the positions of the hydrophone as known via the tanks translation system. This method doesn't compensate for the fact that the plane defined by the transducers and the plane the hydrophone is moved through are not parallel, as seen in Figure 4.62, meaning the estimating is not entirely accurate.

### 4.6.5 Multi target triangulation testing with calibration sphere

The same methodology used in section 4.6.4 can be applied using a calibration sphere as the target as opposed to a hydrophone. The transducers themselves will then serve as both transmitter and receiver. Only a few changes were done when doing the experiment again with the 22 mm tungsten carbide calibration sphere. The distance from the transducer plane to target plane was changed from 1 meter to 2 meters. This was done to make the main lobes of the transducers cover more of the measurement area since it now takes up a smaller angle. The goal was to achieve a higher signal to

noise ratio and avoid points being too far outside the transducers main lobe as to be renders “invisible” by that transducer as the signal would drown in noise and not be detected, rendering the triangulation of the point faulty. For further improved signal to noise ratio, an amplifier was used between the signal generator and the transducer, amplifying the signal by 26 dB. Since the amplification was set at 26 dB and to not damage any equipment, the signal generator was set to deliver 222 mV peak to peak, resulting in a 92 V peak to peak 500 kHz, 45 cycle burst signal being supplied to the transducer every 10 ms. The 1 MHz transducer was swapped for the newest transducer, number 3, and the transducers were moved to the configuration 2, 3 and 6, see Figure 3.26

The new transducer locations result in the transducer coordinates

$$T_1 = (0, 0, 0) \quad T_2 = (-0.0127, -0.181, 0) \quad T_3 = (0.148, -0.112, 0).$$

The method used to produce Figure 4.56 can be done here by plotting the measured amplitude against the known location of the calibration sphere. The results are shown in Figure 4.68-Figure 4.70. The distances measured from each transducer to the calibration sphere is also shown, in Figure 4.71-Figure 4.73. Some points far enough from the transducers sound axis have distance estimates that don’t align with its neighbouring points, this is due to low signal to noise ratio in those areas making signal detection tough. For an example of this see Figure 4.75.

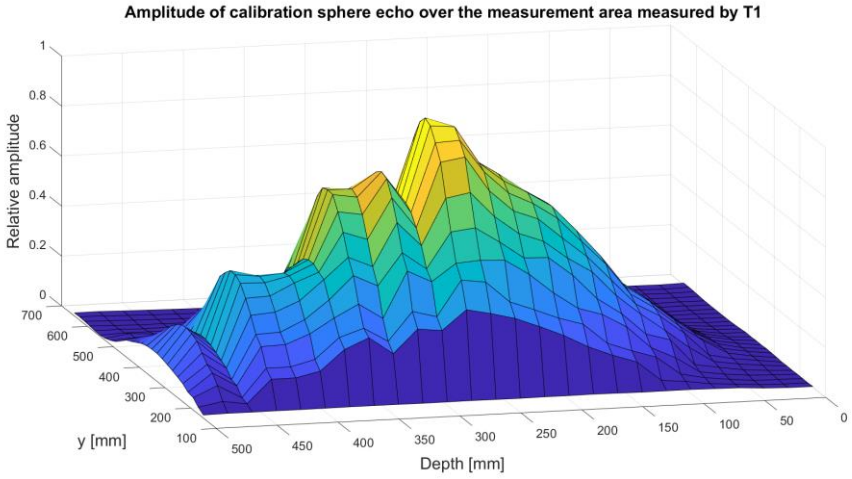


*Figure 4.68: Amplitude of calibration sphere echo over the measurement area measured by T1.*

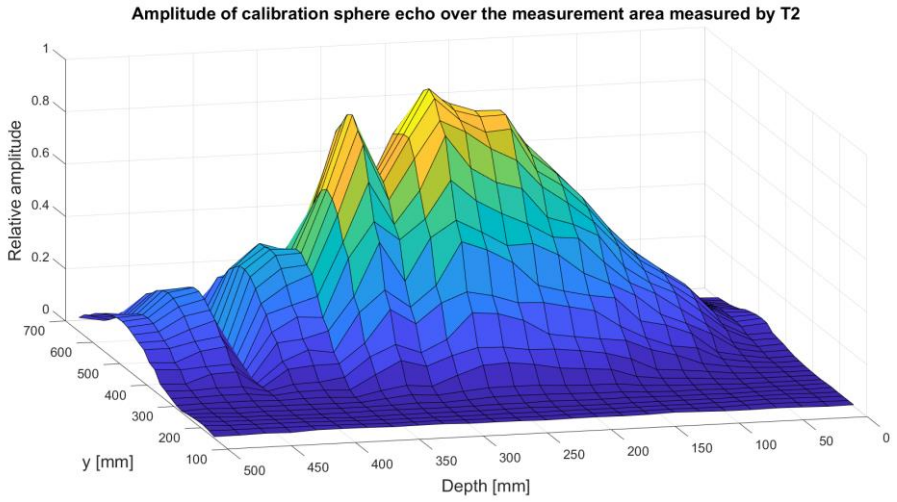


*Figure 4.69:Amplitude of calibration sphere echo over the measurement area measured by T2.*

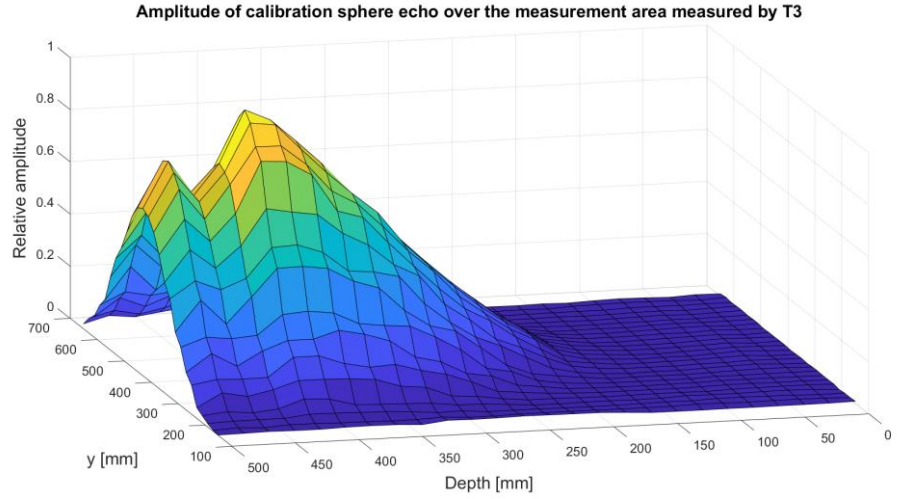


*Figure 4.70: Amplitude of calibration sphere echo over the measurement area measured by T3.*

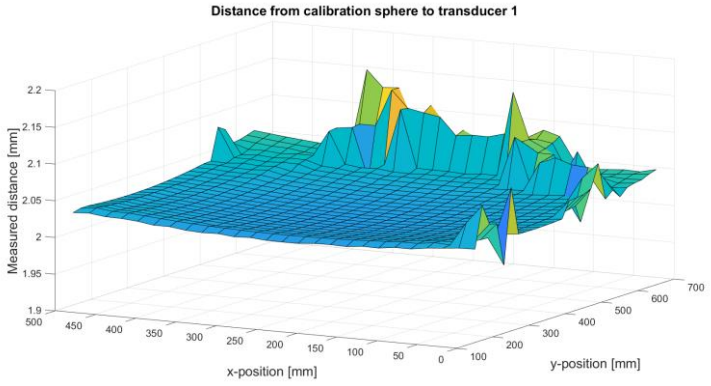


*Figure 4.71: Measured distance from Transducer 1 to calibration sphere.*

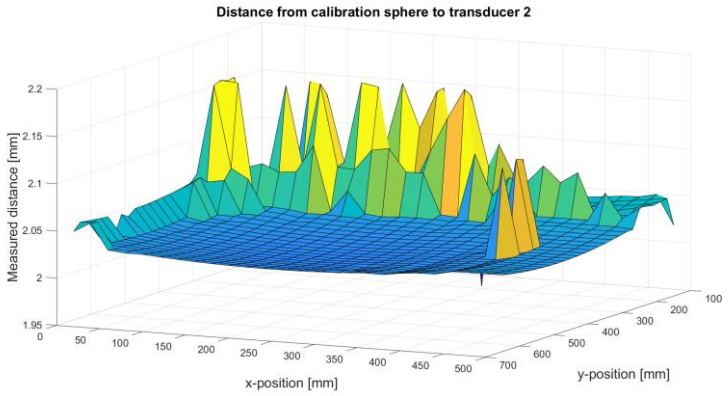


*Figure 4.72: Measured distance from Transducer 2 to calibration sphere.*

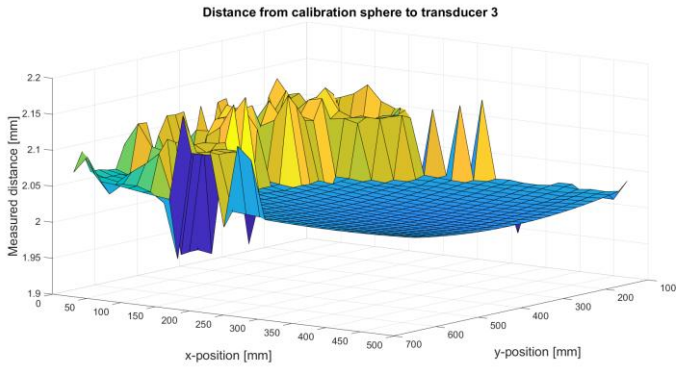


*Figure 4.73: Measured distance from Transducer 3 to calibration sphere.*

The Figures above show the distances measured from transducer to calibration sphere and show the curving distance as the sphere is moved through the measurement plane. The differences between these plots and the ones shown in Figure 4.58-Figure 4.60, corresponding to the distances measured in the hydrophone experiment, are less curvature due to the doubling in distance from transmitter to target, as well as a lot more faulty readings as the echo returning from the calibration sphere is much weaker than the direct signal picked up by the hydrophone, even after amplification and being closer to the sound axis.

Figure 4.68-Figure 4.70 show the effects of the transducers' directivities on the amplitude of the echo returning from the calibration sphere as a function of the spheres position. The positions of the sphere in these plots are from the translation system of the tank. The measurement area being [0, 500] mm in depth and [150, 650] mm in the y direction. The plots show an unexpected effect, an oscillating amplitude as a function of depth that only seems to appear at a depth lower than the transducer measuring it. This is consistent for all three transducers and the pattern is similar for all three. This phenomenon is further discussed in section 4.7.3.

#### *4.6.5.1 Triangulation*

Making sure to compensate for the two-way wave propagation, both by halving the measured travel time to find the distance, and when considering the directivity, which will now be measured as the

square of the beam pattern. The system delay found for calibration spheres in section 4.5 was compensated for when calculating the distances. The resulting points after triangulation are shown in the below.

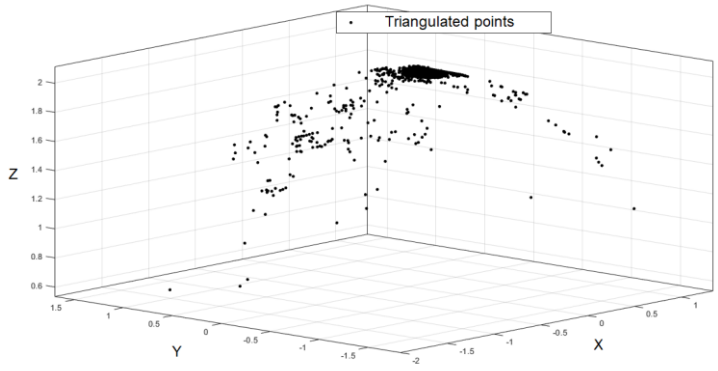


*Figure 4.74: Triangulated sphere positions.*

Figure 4.74 shows several points far away from their expected locations. Looking into these cases, the reason for the faulty triangulation seems to be low signal to noise ratio due to the calibration sphere being far from the main lobe of one of the transducers. An example of the signal received by the three transducers at one of the points is shown in Figure 4.75-Figure 4.77.

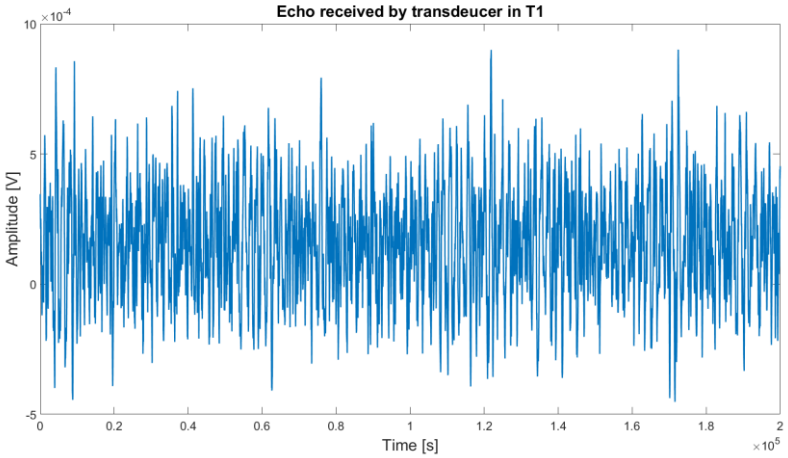


*Figure 4.75: Echo received by T1.*

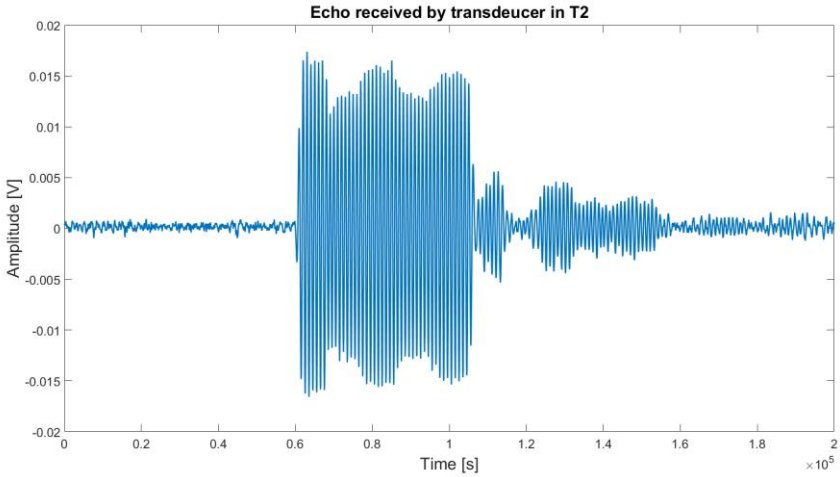


*Figure 4.76: Echo received by T2.*

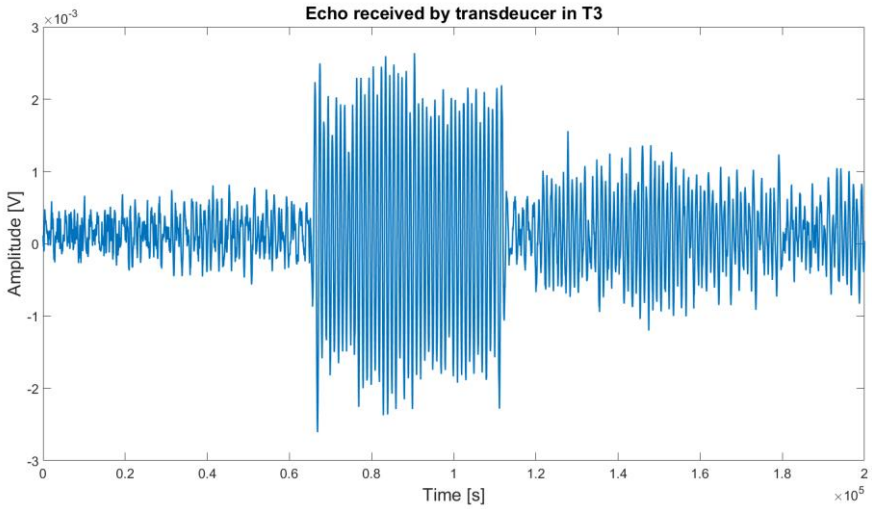


*Figure 4.77: Echo received by T3.*

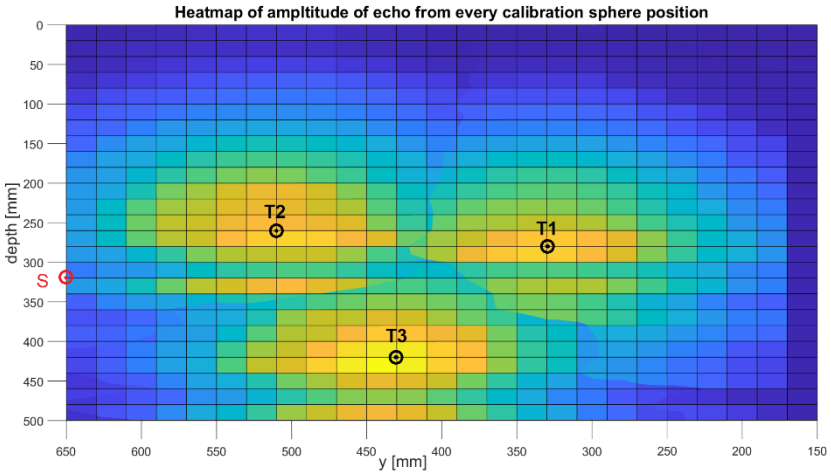


*Figure 4.78: Heatmap of amplitude of echo from all transducers.*

The echoes received by the three transducers shown in the Figures above, were recorded while the calibration sphere was positioned at the point labelled “S” in Figure 4.78. The signal to noise ratio is

good for T2 and T3, but the signal arrival time is undetectable for T1 due to bad STR. The signal detection algorithm then faulters and the resulting triangulated point is placed at the “wrong” location.

After Removing all points deemed to have too low of a signal to noise ratio for any one transducer, the resulting triangulated plane is shown in Figure 4.79, along with a plane of best fit.

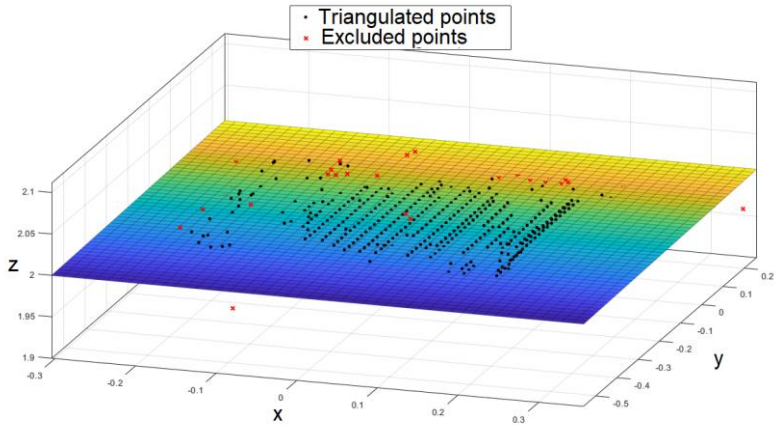


*Figure 4.79: Triangulated points on a plane.*

The resulting plane formed by the points is, as also seen in section 4.6.4, not parallel with the XY-plane defined by the transducer locations. This is again expected.

In Figure 4.80, all amplitudes recorded by T1 at each point is plotted against the angle between the vector from T1 to that point and the z-axis, which is very close to the sound axis of T1. The angle was found by using equation 4.28.

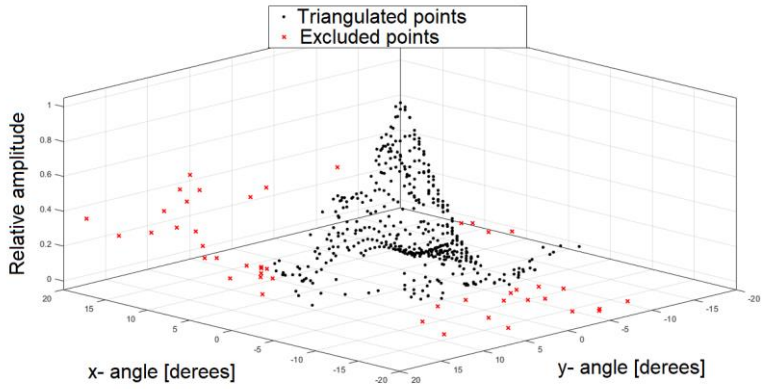


*Figure 4.80: Amplitude of echo from calibration sphere as measured by T1 as a function of angle.*

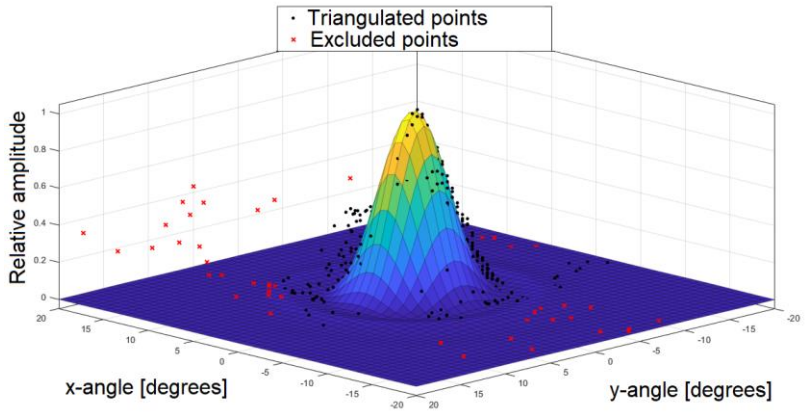


*Figure 4.81: Beam pattern curve of best fit using triangulated points.*

Figure 4.81 shows the estimate for the beam pattern using the points triangulated by calibration sphere plotted with the relative amplitude measured by the transducer at T1. The points deemed to have a too low signal to noise ratio has been excluded from the analysis. The resulting fit is not good, with a R-square of 0.806. The reason for this is thought to be the phenomenon seen in Figure 4.68-Figure 4.70 and further discussed in section 4.7.3, dubbed oscillating target strength. Due to the seemingly irregular amplitude of the echo coming from depths below T1, the estimated beam pattern fit is lacking and an estimate of $\psi$ is bound to be inaccurate. The estimate shown in the Figure above calculates to an estimated value for the two-way equivalent beam solid angle of $\psi = 0.006377$ which is far lower than expected.

The solution to avoid interference from this phenomenon used in this thesis will be to exclude all measurement points triangulated to be at a depth coordinate x below that of T1, which in this case is 0. This means all points with a x-coordinate above 0 will be excluded as the x-axis is defined as being to the floor. This solution is non-optimal for many reasons. The number of sampled points will be almost halved as well as all being from only one side of the beam pattern, making for a poorer beam pattern estimate and therefore poorer $\psi$-estimate. The effects causing the oscillating target strength may also not be exclusive to this area even if it may seem so.

Doing this exclusion and running the curve fitting with the fitting equation

$$B_e(\theta) = \left(\left|\frac{2J_1(v)}{v}\right|^{\gamma}\right)^2 \qquad v = ka\,sin\left((\theta_x + n)^2 + (\theta_y + m)^2\right) \tag{4.33}$$

Which is the same equation as 4.32 but squared as the beam pattern is now two-way. The resulting parameters of best fit are

$$ka = 26 \quad \& \quad \gamma = 1.051$$

with an improved R-square of 0.9577. The resulting curve is shown in Figure 4.83.

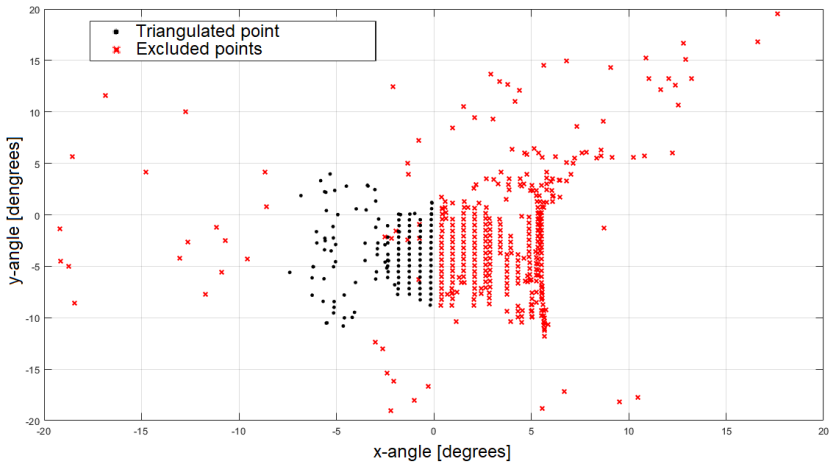


*Figure 4.82: The x and y-positions of the points remaining after exclusion.*

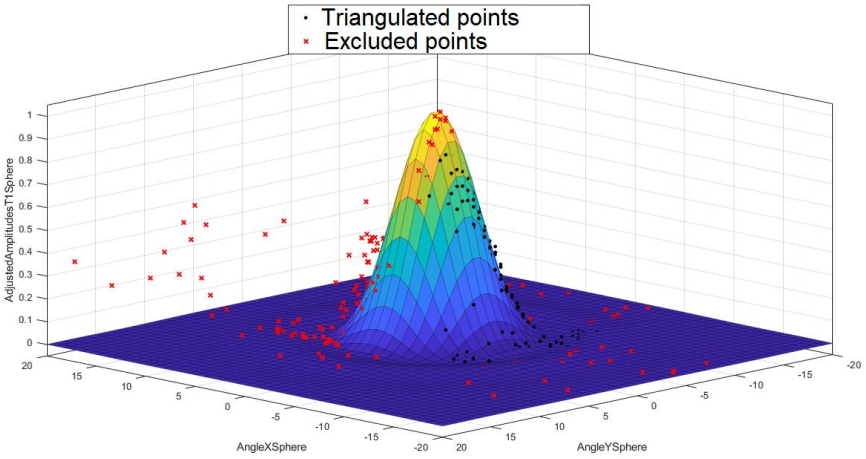


*Figure 4.83: Curve of best fit for the beam pattern of T1 after exclusion.*

### 4.6.6 $\Psi$-estimation

The two-way equivalent beam solid angle is calculated by integrating the beam pattern over all angles, as seen in equation *4.2*. In this section $\psi_h$ is calculated through different methods and the results are compared. The limitation and accuracy of the estimates of $\psi_h$ are also discussed.

#### *4.6.6.1 Simplified formula*

Since over 99% of the transmitted energy is found within the main lobe of the beam pattern [2], $\psi$ can be estimated using the transducers beamwidth [19],

$$\psi \cong \frac{\alpha_{-3\,dB} \times \beta_{-3\,dB}}{5800} \tag{4.34}$$

using a beamwidth of $\alpha_{-3\,dB} = \beta_{-3\,dB} = 7°$, which is the piston model estimated beamwidth of the 500 kHz transducers used in this study as well as the beam width of most the transducers used on in the scientific echosounder aboard research vessels for fisheries acoustics [20], gives the estimate

$$\psi_h^s = 0.0084483\ sr$$

#### *4.6.6.2 Piston model estimation*

By using the theoretical beam pattern found for a 500 kHz transducer with a face diameter of 25 mm in the conditions of the experiment tank, found with the piston model in section 4.3.1, it is possible to calculate the two-way equivalent beam solid angle. Using the piston model beam pattern and the equation for best fit used 4.32, the parameters are $ka = 26.47$ and $\gamma = 1$, and integrating over the angles $\theta = [0{,}360]$ and $\varphi = [0{,}90]$ gives an estimate for $\psi$.

$$\psi_h^{pm} = 0.0082381\ sr$$

#### *4.6.6.3 Estimation through hydrophone measured directivity*

In section 4.3.2, the directivity of the transducers as measured by a hydrophone was presented. The 500 kHz transducer referred to as transducer β was then baffled with a 12 cm and a 32 cm baffle, and the directivities were again measured by hydrophone. This is the same transducer which directivity is estimated via triangulation in sections 4.6.4 & 4.6.5. The results from directivity measurements is then compared by calculating the corresponding two-way equivalent beam solid angle using equation 4.26.

The estimate of the beam pattern for transducer β when in free field as well as baffled by the 12 cm and 32 cm baffles was found using MATLABs Curve Fitting Tool and used equation 4.26 and the best fit was found. The results are presented below.

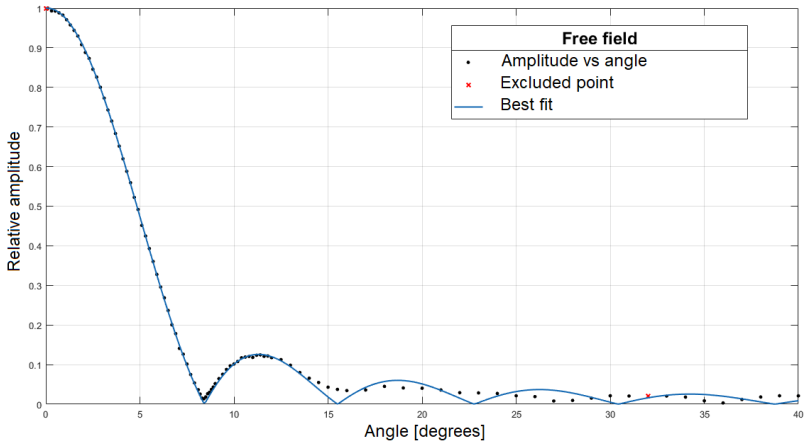


*Figure 4.84: Estimate of beam pattern in free field.*

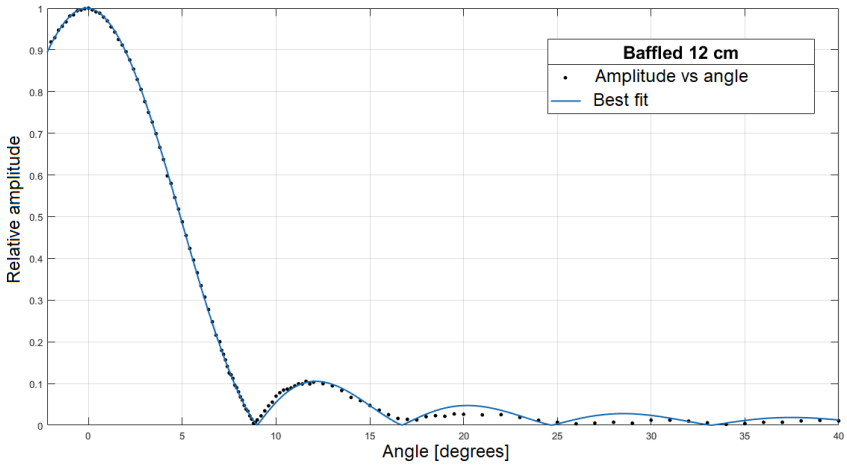


*Figure 4.85: Estimate of beam pattern when baffled 12 cm.*

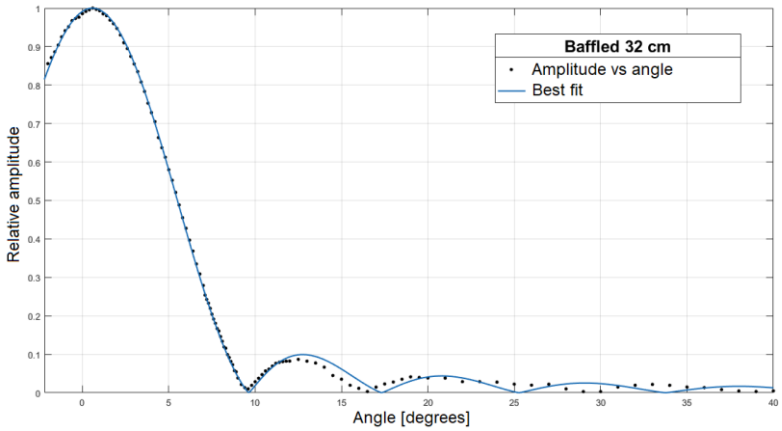


*Figure 4.86: Estimate of beam pattern when baffled 32 cm.*

The Figures above show the best fitting estimate of the beam pattern when the transducer is in free field and baffled. Below are presented the parameters for each estimate as well as the goodness of fit.

| | Figure | $ka$ | $c$ | R-square |
|---|---|---|---|---|
| **Free field** | Figure 4.84 | 26.36 | 1.025 | 0.9992 |
| **12 cm baffle** | Figure 4.85 | 24.26 | 1.113 | 0.9996 |
| **32 cm baffle** | Figure 4.86 | 24.35 | 1.141 | 0.9994 |

*Table 4.1: Beam pattern regression from free field and baffled directivity measurements.*

Using these parameters, it is possible to estimate a value for the two-way equivalent beam solid angle by rotating the estimate about the y-axis and integrating over all angles using equation 4.26. As discussed in 4.1, in this analysis only the elevation angles [0-90°] will be used, as almost all energy in the beam pattern is found in this interval [2]. The expression for $\psi_h$ can be written as

$$\psi \approx \psi_h = \int_0^{\pi/2} \int_0^{2\pi} B_e^4(\theta, \varphi)\, sin(\varphi)\, d\theta d\varphi \tag{4.35}$$

where $B_e$ is the estimated beam pattern.

The resulting estimates of $\psi_h$ are:

$$\psi_h^{FF} \approx 0.0081166\ sr$$

$$\psi_h^{12cm} \approx 0.0088795\ sr$$

$$\psi_h^{32cm} \approx 0.0086121\ sr.$$

#### *4.6.6.4 Estimate through triangulation*

By using the curves found via the methodologies described in section 4.6.4 & 4.6.5, $\psi_h$ can be estimated by integrating over the estimated beam pattern. Equation 4.26 is then used together with MATLABs "trapz" function to calculate the value for $\psi_h$ based on the estimate for the beam pattern found via triangulation with a hydrophone, using $ka = 26.37$ and $\gamma = 1.053$ as found in section 4.6.4, the resulting curve is shown in the Figure below.

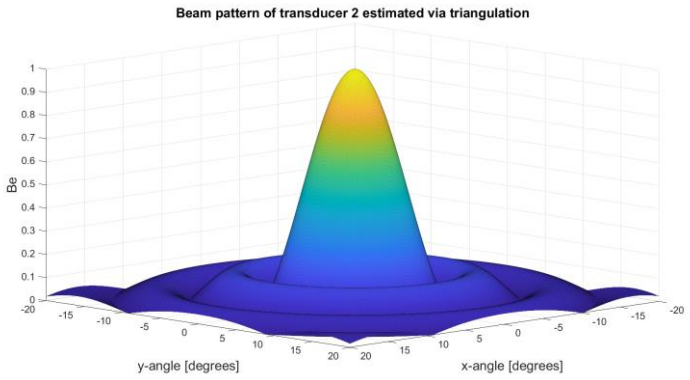


*Figure 4.87: Beam pattern estimate via hydrophone triangulation.*

Integrating the beam pattern estimate, $B_e$, for transducer β, shown in Figure 4.87, over the angles $\theta = [0,360]$ and $\varphi = [0,90]$ gives an estimate for $\psi_h$.

$$\psi_h \approx \int_0^{\pi/2} \int_0^{2\pi} B_e^4(\theta,\varphi)\, sin(\varphi)\, d\theta d\varphi$$

4.36

$$\psi_h^{ht} \approx 0.0079193\ sr$$

Further, the beam pattern estimate for transducer β found by triangulation using a calibration sphere in section 4.6.5 is used to estimate $\psi$. The parameters for the curve of best fit are $ka = 26$ and $c = 1.051$ and the resulting curve is shown in the Figure below.

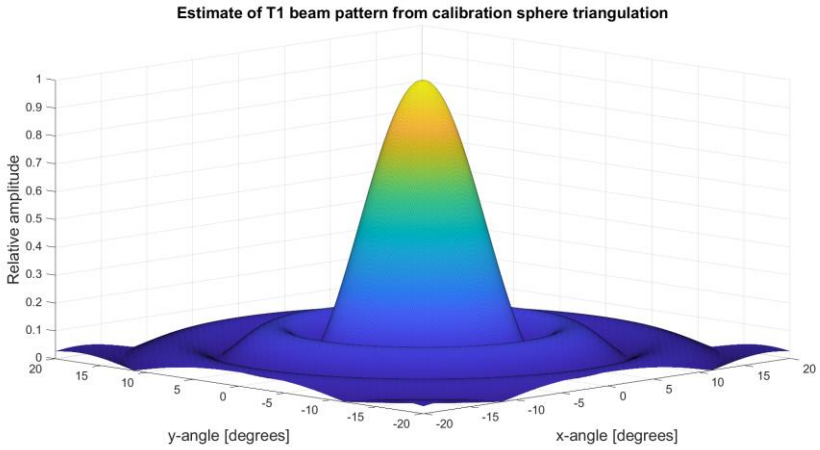


*Figure 4.88: Beam pattern estimate via calibration sphere triangulation.*

In Figure 4.88 the curve of best fit for the beam pattern of transducer β (T1) as found by triangulation of the calibration sphere is shown. If this curve is integrated over the angles $\theta = [0,360]$ and $\varphi = [0,90]$, an estimate for $\psi$ is found.

$$\psi_h \approx \int_0^{\pi/2} \int_0^{2\pi} B_e^4(\theta,\varphi)\, sin(\varphi)\, d\theta d\varphi$$

4.37

$$\psi_s^{st} \approx 0.0081494\ sr.$$

*4.6.6.5 Results and discussion*

The different estimates for the values of the two-way equivalent beam solid angle $\psi$ are presented in the following table and will be discussed in this section.

| Case | $\Psi_h$-estimate [sr] |
|---|---|
| **Simplified formula** | 0.0084483 |
| **Piston model estimation** | 0.0082381 |
| **Free field hydrophone measurement** | 0.0081166 |
| **12 cm baffle hydrophone measurement** | 0.0088795 |
| **32 cm baffle hydrophone measurement** | 0.0086121 |
| **Hydrophone triangulation** | 0.0079193 |
| **Calibration sphere triangulation** | 0.0081494 |

*Table 4.2: Value of $\psi_h$ as estimated in different cases.*

For ease of comparison the cross-section of the estimated beam pattern for all estimation methods are plotted in the Figures below.

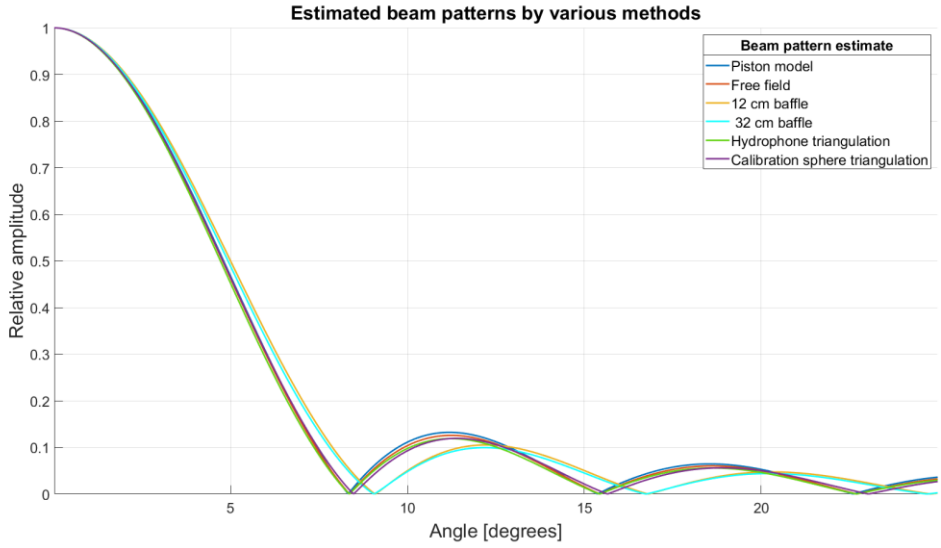


*Figure 4.89: All estimates of beam pattern through different methods.*

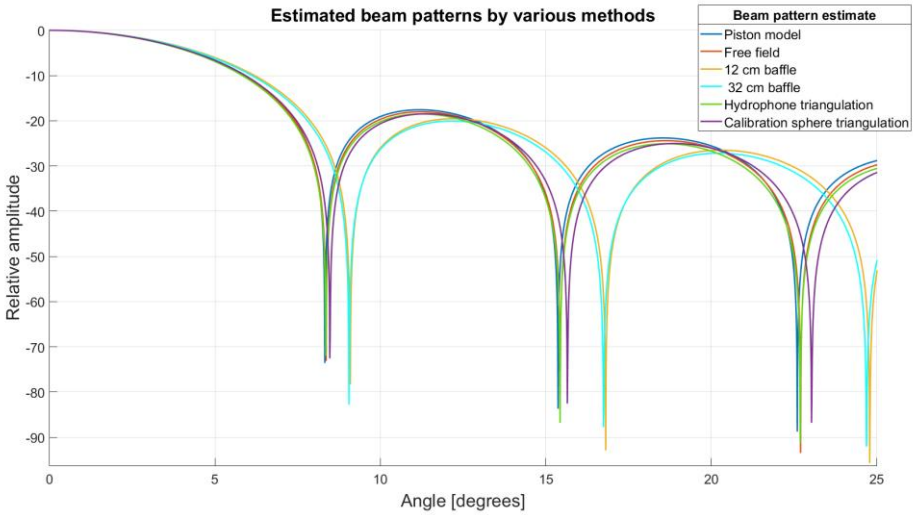


*Figure 4.90: All estimates of beam pattern through different methods in decibel.*

The two beam patterns corresponding to the measurements of the baffled transducers stand out from the rest, both in shape and estimate of $\psi_h$. As seen in section 4.3.4 the baffle seems to widen the main lobe, this would in turn result in a higher value of $\psi_h$ as more of the energy in the beam is now beam directed at a wider angle making the equivalent solid angle also wider. The introduction of a baffle also seems to lower the amplitude of the first side lobe, something that would narrow the equivalent beam solid angle as less energy is directed at these wider angles. The effect of this van be seen in the estimate of $\psi_h$ for the case of the 32 cm baffle as the width of the main lobe is the same as for the 12 cm baffle, but the first side lobe has a lower amplitude, making the estimate for $\psi_h$ narrower in the case of the 32cm baffle than for the 12cm baffle. This indicates that bafflement may both widen and narrow the two-way equivalent beam solid angle by both widening the main lobe and lowering the side lobes.

The estimates derived from triangulation would, in comparison, suggest a slight effect from bafflement but not as severe as observed with the 12 and 32 cm baffles. This is indicated by the parameter $\gamma$, which represents a weakening of the side lobes compared to the main lobe. Theoretically the value should be $\gamma = 1$, but choosing a parameter of slightly more than one fits the measured beam pattern better, and bafflement seems to increase the value of $\gamma$, and therefore, as seen in section 4.6.6.3, weaken the side lobes. Table 4.3 presents the parameter $\gamma$ in all considered cases.

| Case | $\gamma$ |
|---|---|
| **Piston model** | 1 |
| **Free field** | 1.025 |
| **Triangulation mount** | 1.052 |
| **12 cm baffle** | 1.113 |
| **32 cm baffle** | 1.141 |

*Table 4.3: Value of regression γ-parameter for different cases.*

Table 4.3 shows an increase in parameter $\gamma$ as bafflement increases. Even the "free field" transducer has some bafflement in its casing. The $\gamma$-parameter seems to indicate the triangulation mount is between the 12 cm baffle and the "free field" case. The $\gamma$-parameter, of course, was introduced in this study and holds little weight as predictor.

The estimates of the beam pattern labelled "Free field", "Hydrophone triangulation" and "Calibration sphere triangulation", shown in Figure 4.89 & Figure 4.90, stay close to the theoretical beam pattern found via the piston model. Only the calibration sphere estimate is slightly different. The lack of good signal to noise ratio as well as the unexpected phenomenon, discussed in section 4.7.3, excluding most measurement points, made for a non-ideal size and distribution of the dataset for estimating the beam pattern. The estimate found through triangulation using the hydrophone may be a better representation of the methodology as it lacks most of the aforementioned problems with using the calibration sphere on the set-up used in this thesis.

If the measurement of the free field beam pattern is assumed to be the "true" beam pattern of transducer β, then value for $\psi$ derived from it can be compared with the estimates found via the triangulation methods. The percentage of the

| Estimation method | % of "true" $\psi$ |
|---|---|
| **Free field** | 100.00 % |
| **Hydrophone triangulation** | 97.57 % |
| **Calibration sphere triangulation** | 100.40 % |

*Table 4.4: ψ estimates from triangulation methods compared to free field directivity measurement.*

Table 4.4 shows accuracy of the estimation of the two-way equivalent beam solid angle $\psi$ by the two triangulation experiments performed in this study. This is assuming the free field estimate is the true value which is not the case as the triangulation mount will have changes the beam pattern of the transducers, if only slightly.

#### *4.6.6.6 Suggestions for on-ship estimation*

When doing on ship calibrations with suspended spheres under the ships keel, measuring the entire beam pattern is not practical or feasible. Often only the main lobe, or part of it can be measured [5]. A method for estimating $\psi$ from measurements of only parts of the beam pattern is needed, a way of extrapolating the full value of $\psi$ from the measurement of the main lobe. Most of the energy in the beam pattern is focused on the main lobe and therefore most of the value for $\psi$ is found by integrating over only the main lobe [2]. An analysis of the accumulative value $\psi_c$ as equation 4.26 is integrated over the angles $\theta = [0,360]$ and $\varphi = [0,90]$, is shown in the Figure below.

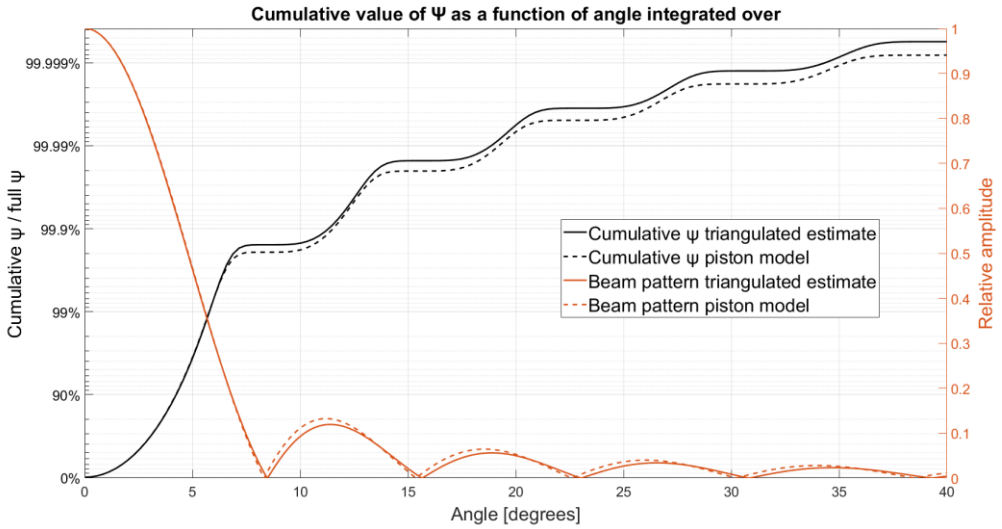


*Figure 4.91: Cumulative psi comparison between piston model and estimated beam pattern.*

In Figure 4.91, the cumulative value for $\psi_c$ is plotted as a function of the angle from the sound axis, integrated over, as well as the beam pattern used to find $\psi_h$. Meaning integrating to the first zero points results in an estimated $\psi$ of around 99.985 % of the "full" value being, in this case, integrated out to 90°. The x-axis shows the value of the cumulative $\psi_c$ as a percentage of the "fully" integrated $\psi_h$, which is listed in Table 4.2. The piston model and the estimate of the beam pattern found through the calibration sphere triangulation method are both plotted.

Both by using the theoretical piston model and by the triangulation method, over 99.8 % of the value of $\psi_h$ has been reached once the main lobe has been integrated over. This means that only about 0.2 % of the value of $\psi_h$ is found by integrating further. A final estimate for $\psi_h$ can be found with high accuracy by integrating a model that fits the main lobe only out to the first zero and then adding a small amount to compensate.

All the $\psi$ estimation methods shown in Table 4.2, are again shown in Table 4.5 below with the percentage of fully integrated $\psi$ when only considering the main lobe.

| Case | % of $\psi_h$ cumulated from main lobe |
|---|---|
| **Piston model** | 99.81 % |
| **Free field** | 99.81 % |
| **12 cm baffle** | 99.90 % |
| **32 cm baffle** | 99.92 % |
| **Hydrophone triangulation** | 99.84 % |
| **Calibration sphere triangulation** | 99.84 % |

*Table 4.5: Percentage of $\psi$ cumulated from integrating over main lobe in different cases.*

As shown in the table above all models and estimation reach above 99.8 % of the "true" value for $\psi_h$ once only the main lobe has been considered. Measuring only the main lobe will then give a highly accurate measurement of the two-way equivalent beam solid angle for the transducers used in this study and can be made more accurate by adding a small amount to compensate. These numbers are also relevant to the echosounders used by IMR as the ka numbers of the transducers are the same as the once in this study.

#### 4.6.6.6.1 Example

As an example, by simulating a high-quality triangulated dataset by using only the points known to be within 5° of the sound axis during the hydrophone triangulation experiment, an estimate of the main beam pattern based only on measurements of the main lobe can be made. All points outside 5° have been excluded from the estimation and the curve fitting analysis is done again. Since none of the side lobes are measured, the value for $c$ needs to be set beforehand as to not widen the main lobe too much. If $c$ is left as a free parameter, the resulting best fit will lack side lobes and will result in a faulty estimate of $\psi$. An example is shown in the Figure below.

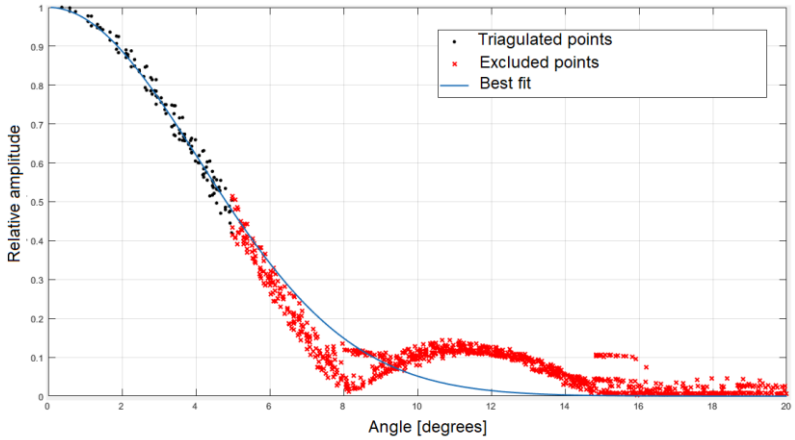


*Figure 4.92: Beam pattern estimate based on main lobe, $\gamma$ = 208.*

As Shown in Figure 4.92, leaving $c$ unfixed when basing the beam pattern estimate off the main lobe only will result in faulty estimate beyond 5°. A value for $\gamma$ is therefor set based in prior experience.

For this study $\gamma$ was set to 1.025 as it was the value found to fit best during the free field directivity measurements shown in section 4.6.6.3. A natural choice would be setting $\gamma$ to 1 as is calculated from the piston model, both possibilities are explored in this study.

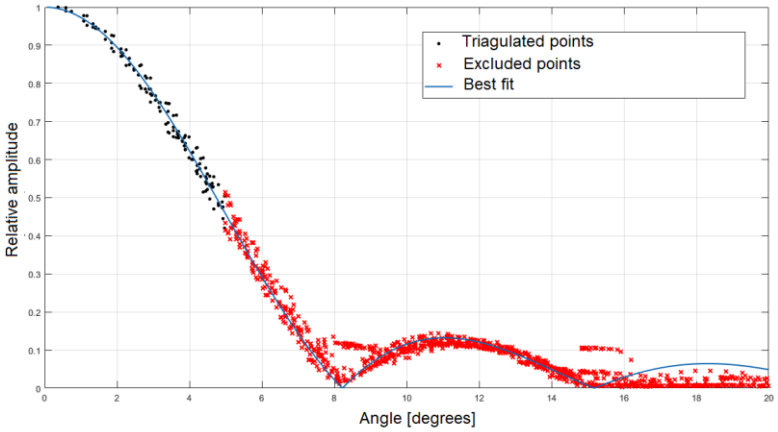


*Figure 4.93: Beam pattern estimate based on main lobe, γ = 1.*

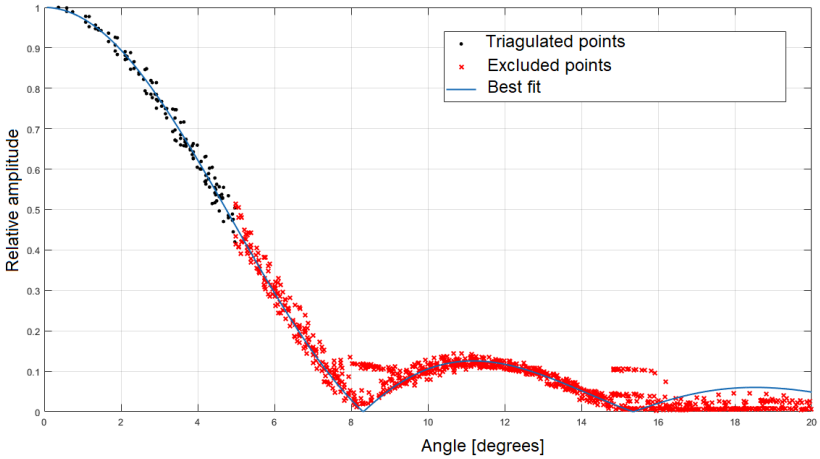


*Figure 4.94: Beam pattern estimate based on main lobe, γ = 1.025.*

Further, the resulting estimates for $\psi_h$ are presented in the table Table 4.6: Results from main lobe $\psi$ estimation.. Both values for $c$ are included and also two methods for achieving $\psi_h$, estimating over the full 90° or estimating to the first zero and adding a small amount to compensate. Based on the previous Figures for percentage of $\psi_h$ found be integrating over the main lobe, presented in Table 4.5, the compensation used is dividing by 0.998, thereby assuming 99.8 % of the value for $\psi_h$ has been found while integrating over the main lobe.

$$\psi_{compensated} = \frac{\psi_{main\ lobe}}{0.998} \tag{4.38}$$

| | $c$ | $ka$ | $\psi_h$ | $\psi_{\mathbf{compensated}}$ | % of "true" $\psi_h$ |
|---|---|---|---|---|---|
| **Method 1, Figure 4.93** | 1 | 26.79 | 0.0080403 sr | 0.0080375 sr | 99.03 % |
| **Method 2, Figure 4.94** | 1.025 | 26.5 | 0.0080309 sr | 0.0080311 sr | 99.94 % |

*Table 4.6: Results from main lobe ψ estimation.*

"True" $\psi_h$ is the same as used in Table 4.4. Both methods resulted in estimates of $\psi_h$ very close to those of the other methods discussed.

## 4.7 Potentially interfering phenomena

### 4.7.1 Calibration sphere resonance

This phenomenon was noted while working on finding good parameters to using during experiments involving calibration spheres such as number of cycles, delay between burst and signal frequency. It was discovered that for certain frequencies, the echo received from the sphere had been severely altered and extended. After further investigation it was discovered that this phenomenon repeats itself every 60 kHz. If the signal frequency is set too far from the resonance frequency of the transducer however, the phenomenon is drowned out by other effects. It is therefore most clear closest to the transducer's optimal frequency, in this case 500 kHz. The phenomenon is observed at the frequencies

$$(480 \pm n60)\, kHz \qquad n = 1, 2, 3 \ldots$$

*4.39*

The echo received from the sphere at these frequencies is normal for the first few cycles and is then gradually dampened to be almost completely silent. Then, at the time the normal echo would be expected to end, an almost identical echo is received again.

Figure 4.14 shows the echoes received from the tungsten carbide calibration at a distance of 88 cm, when ensonified by a 50-cycle burst at different frequencies using the one of the 500 kHz transducers. The Figure shows the effects is apparent at 420 kHz, 480 kHz and somewhat at 540 kHz. The frequencies in between were scanned through to check for any other occurrences, but none were found in the frequency band [420-580].

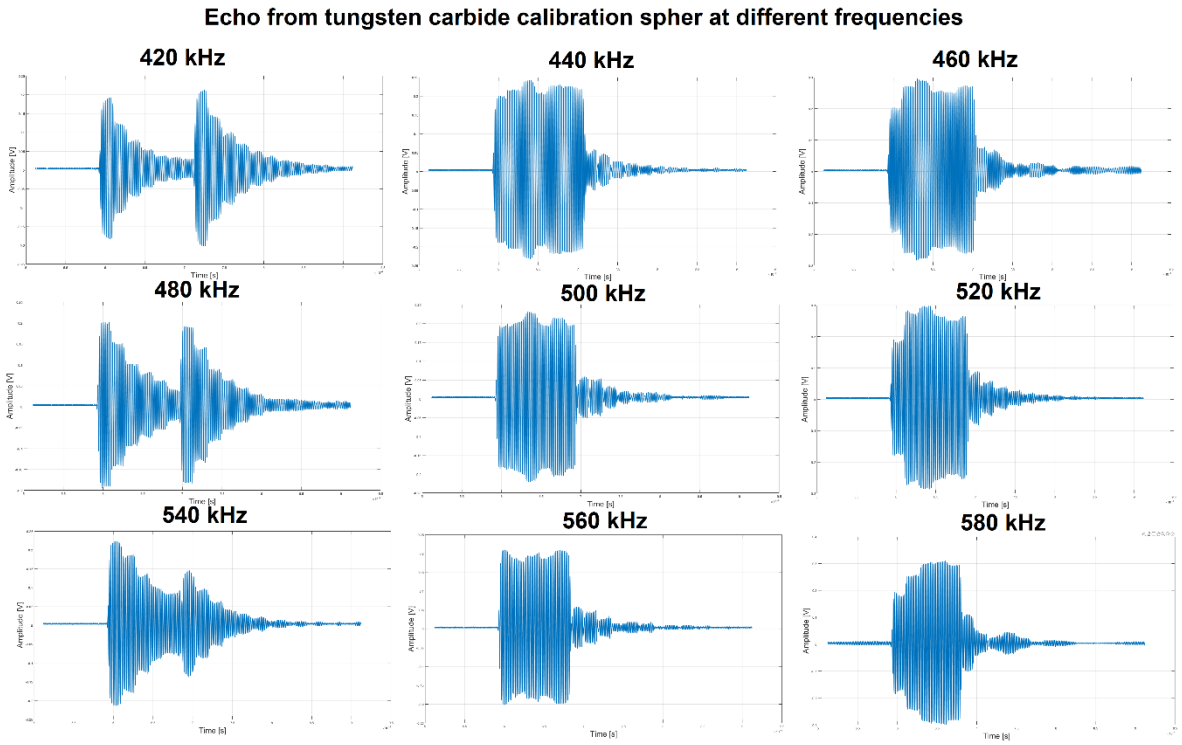


*Figure 4.95: Echo from tungsten carbide sphere at various frequencies*

A hypothesis for the origin shapes of the echoes around certain frequencies is presented here. This effect may be from hitting the resonance frequencies of the calibration sphere. The very start of the signal transmitted from the transducer contains several frequencies other than the signals main frequency, which may be the reason it is reflected by the sphere. While when the signal has become stable and only contains the resonance frequency of the sphere, the waves are absorbed by the sphere as it starts to vibrate. The same thing happens as the sent signal ends. The signal now contains several different frequencies that are reflected by the sphere. After this the sphere will by vibrating at its resonance frequency and therefore produce sound that is detected by the transducer for a short time after the sphere is no longer ensonified by the signal sent by the transducer. This sound is seen as the tails after the peaks in the echoes.

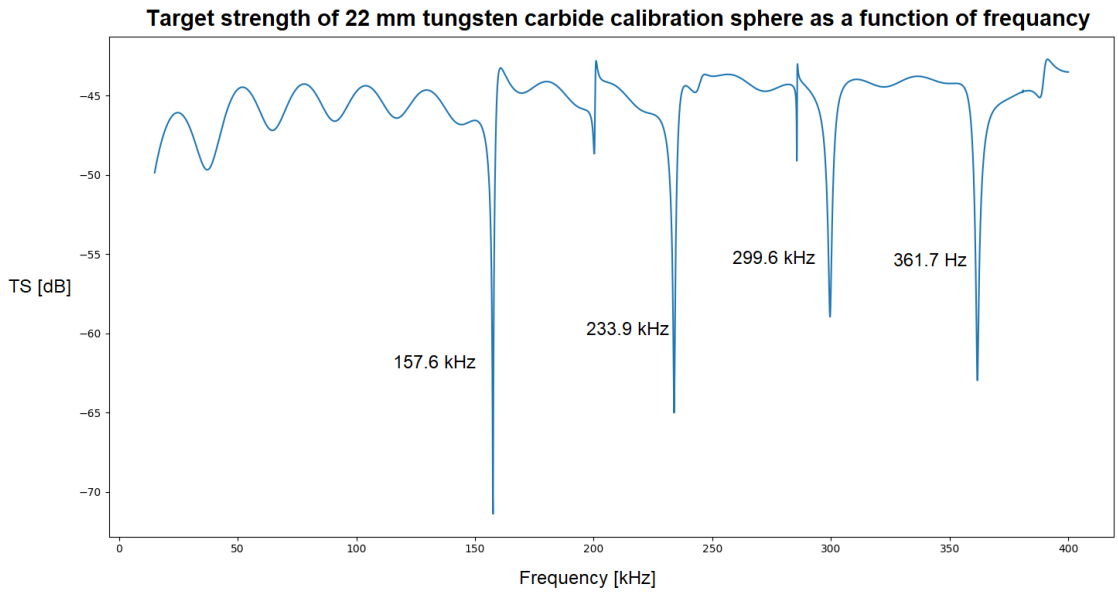


*Figure 4.96: Target strength of 22 mm tungsten carbide calibration sphere as a function of frequency as measured by IMR.*

The measured target strength of the same 22 mm tungsten carbide calibration sphere has been measured by IMR and is plotted in Figure 4.96. Continuing the trend, the next expected resonances should be around somewhere around 420, 480 and 540 kHz, as observed in Figure 4.14.

Similar effects were observed using the steel and copper calibration spheres. Non-of the spheres displayed resonance effects at 500 kHz.

### 4.7.2 Calibration sphere circumferential waves

After placing the tungsten carbide calibration sphere in the experiment tank for initial testing, an unexpected phenomenon was observed. When sending a sufficiently strong signal containing just a few cycles, the initial direct echo from the sphere was followed up by several similar echoes with exponentially lower amplitudes. Sphere was placed 64 cm from the transducer, while transmitting 3 cycle, 500 kHz, 10 V peak-to-peak signal from a transducer and the echo was recorded with the same transducer, using the calibration sphere set-up described in section 3.1.1.2. The resulting echo is shown in Figure 4.97.

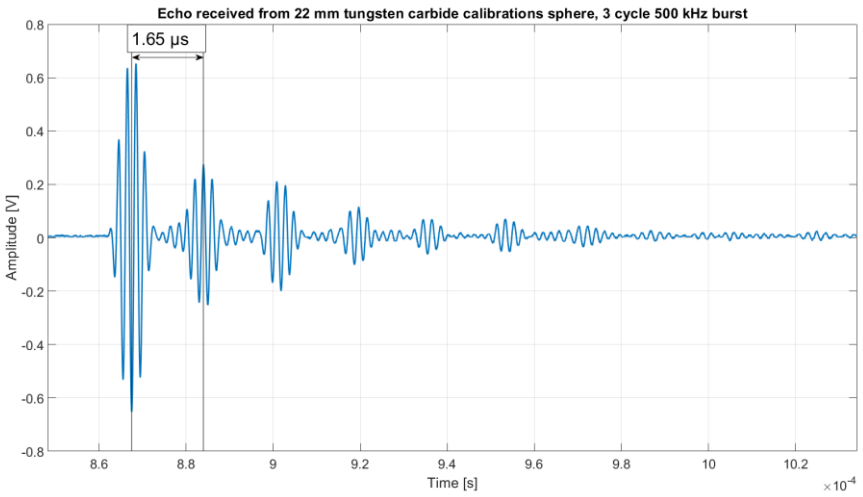


*Figure 4.97: Echo from 22 mm tungsten carbide calibration sphere for 500 kHz.*

The initial echo is as expected, but following it is a series of weaker, equally spaced out “echoes”. It is thought that this phenomenon might be the cause of the irregular shape of the echo received from calibration spheres while using longer bursts. Figure 4.98 shows a signal shape consistently seen when receiving echoes from calibration spheres using long bursts.

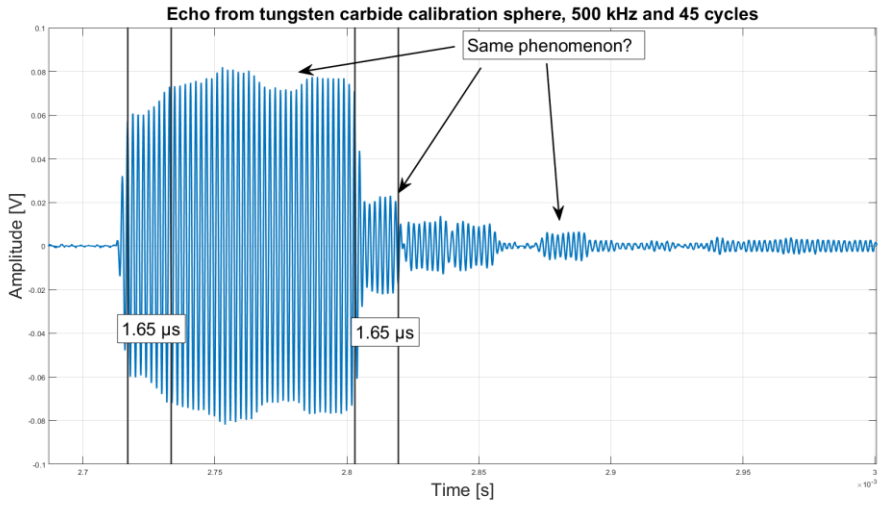


*Figure 4.98: Echo from calibration sphere transmitting 45 cycle burst showing unexpected pattern.*

The plot above shows a similar echo trailing after the main echo after the initial burst has been fully reflected at around 2.8 ms, with a similar drop in amplitude and delay as shown in Figure 4.97. The ending of the main direct echo seems to be followed by a weaker echo lagging about 1.65 µs behind. This is then also followed by an even weaker echo delayed by the same amount. In addition, the start of the direct echo is weaker than the rest, lasting for also around 1.65 µs. This suggests a continues second echo interfering with the direct echo lagging slightly behind. 1.65 µs is the same delay observed when transmitting 3 cycles, suggesting it is cause by the same phenomenon.

#### *4.7.2.1 Measuring circumferential echo delay*

In order to find a possible explanation for this phenomenon, the exact delay between the periodic echoes needs to be measures. This was done in the experiment tank for all three calibration spheres. A transducer was pointed at the spheres, being supplied with a 10 Volt peak to peak 500 kHz signal every 10 milliseconds. The sinusoidal signal sent was only 3 cycles long in order to be able to see the periodic echoes individually. 3 cycles struck a good balance between signal strength and shortness. The echoes received were then averaged for 60 seconds to get the best possible signal to noise ratio. The averaged signal was then saved, and its envelope found using the MATLAB's envelope function. A moving mean was then also performed on the envelope function to get a smooth curve with a distinct maximum for each periodic echo. The absolute value of the averaged received signal for the three calibration spheres with labelled time delays between periodic echoes can be seen below in Figure 4.99 - Figure 4.101.

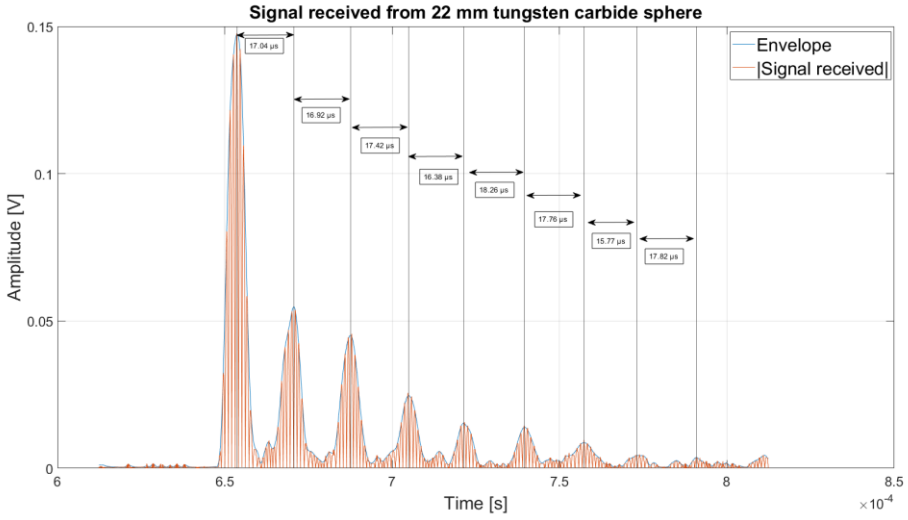


*Figure 4.99: Echo from 22 mm tungsten carbide calibration sphere with envelope.*

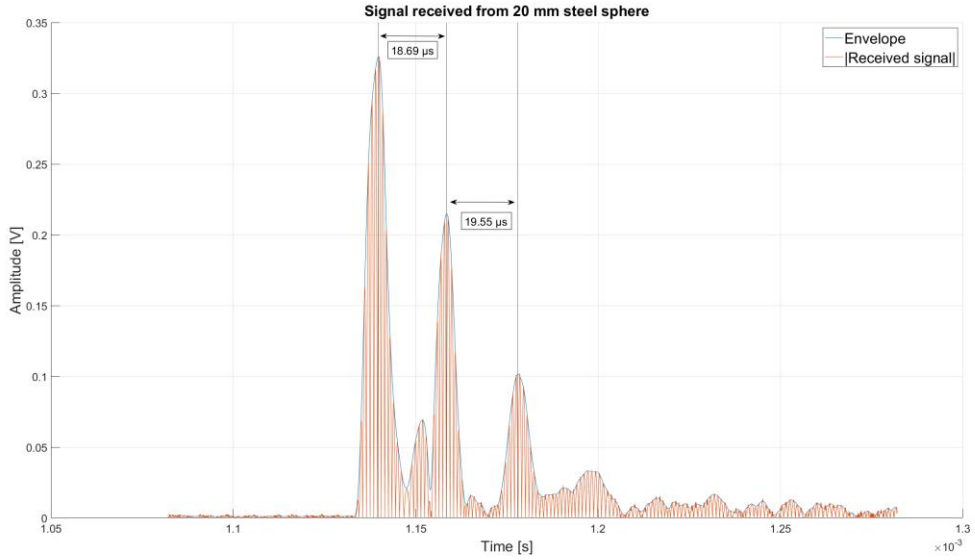


*Figure 4.100: Echo from 20 mm steel calibration sphere with envelope.*

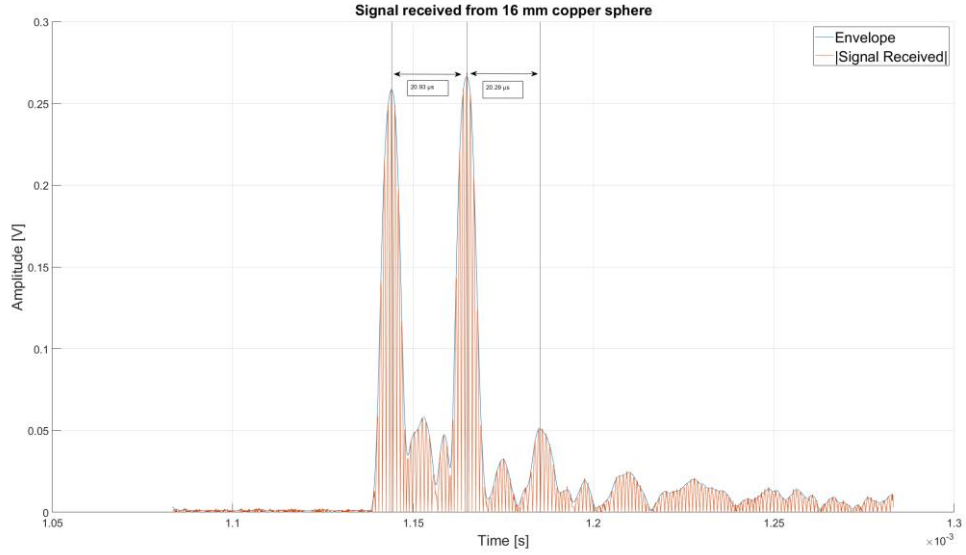


*Figure 4.101: Echo from 16 mm copper calibration sphere with envelope.*

By only using the delay between the distinguishable peaks, an average for the periodic time delay was found. For the sake of consistency only the first three peaks were considered for all three spheres when finding the average delay. These were found to be 16.98 µs for the tungsten carbide sphere, 20.61 µs for the copper sphere and 19.12 µs for the steel sphere.

#### *4.7.2.2 Investigating possible explanations*

##### 4.7.2.2.1 Creeping waves

The phenomenon was first thought to be linked to creeping waves. Where the wave front hitting a curved surface like a sphere, following the surface and radiates out from the surface while traveling along it. If on a sphere the creeping wave will eventually also radiate back towards the source of the incoming wave, registering as a delayed echo [21]. While some of energy in the creeping wave is

radiated away while traveling around the circumference, the wave may travel several circumstances before dying out. This could explain why there are several observed echoes with a constant delay and diminishing amplitudes coming from the calibration spheres.

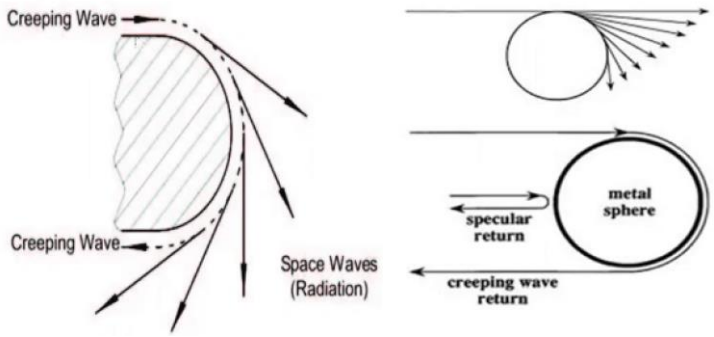


*Figure 4.102: Creeping waves [22, 23].*

To investigate if this could be the case, the delay between the circumferential echoes for the three different spheres was compared to the expected time delay caused by a creeping wave. Knowing the speed of sound in the water, the expected time delay between creeping echoes could be compared with the actual delays recorded in practice. The delay between any given creeping wave will be equal to the time sound takes to travel the radius of the sphere twice plus half the circumference, and can expressed like this

$$\Delta t_{cw} = \frac{2a + \pi a}{c} \tag{4.40}$$

where $a$ is the radius of the sphere and $c$ is the sound speed in the medium surrounding the sphere.

*( 2 )*

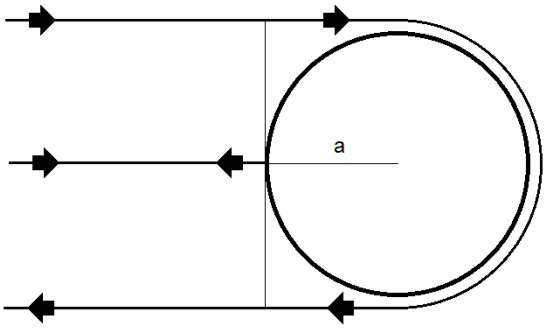


*Figure 4.103: Creeping wave propagation path.*

| Sphere | Material | Diameter | $\Delta t_{cw}$ | Measured delay |
|---|---|---|---|---|
| **1** | Tungsten Carbide | 22 mm | 38.1 µs | 16.98 µs |
| **2** | Copper | 16 mm | 27.7 µs | 20.61 µs |
| **3** | Steel | 20 mm | 34.6 µs | 19.12 µs |

*Table 4.7: Creeping wave delay compared to measured delay.*

The table above presents the calculated delays between creeping waves per equation 4.40, compared to the measured delays observed using calibration spheres. The expected delay between creeping wave does not line up with the actual delay that is observed. This means that there is probably another explanation behind these echoes.

#### 4.7.2.2.2 Surface waves

Another explanation involving surface waves in the sphere will now be proposed. The circumferential wave may not be moving through the water but rather through the surface of the calibration sphere and radiating into the surrounding water in a similar way to creeping waves. This would explain the observation that seems to indicate the observed circumferential waves being faster than normal creeping waves. It was first observed that the shear wave speed of the sphere's material fit much better with the measured results. Rayleigh waves, a type of surface wave, have a similar speed to shear waves in materials with a high Poisson Ratio such as the materials used in the calibration spheres. Although many types of surface waves exist, for the purpose of this study, the proposed surface waves in the calibration spheres are assumed to be Rayleigh waves.

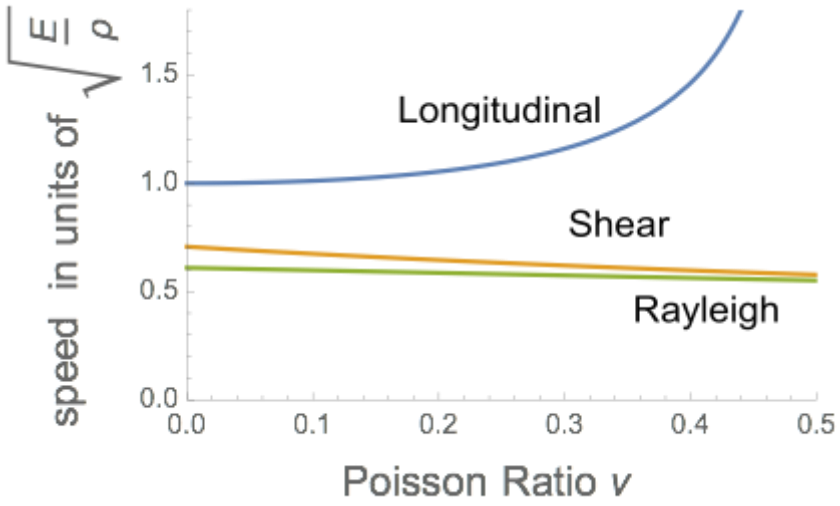


*Figure 4.104: Longitudinal, shear and Rayleigh wave speeds as a function of Poisson ratio [24].*

The Rayleigh wave speed can be approximated using the following formula, proposed by Malischewsky [25].

$$c_R = c_S(\,0.874 + 0.196v - 0.043v^2 - 0.055v^3)$$

*4.41*

Where $c_S$ is the shear wave speed and $v$ is Poisson Ratio. The shear wave speed in a medium can be calculated with the following formula.

$$c_S = \sqrt{\frac{\mu}{\rho}}$$

*4.42*

Where $\mu$ is the shear modulus, and $\rho$ is the density of the material. Using known values for these material constants, one can estimate the Rayleigh wave speed in each of the calibration spheres.

| Material | Poisson ratio | Density [kg/m$^3$] | Shear modulus [GPa] | Shear wave speed [m/s] | Rayleigh wave speed [m/s] |
|---|---|---|---|---|---|
| **Tungsten Carbide** | 0.31 | 15 630 kg/m$^3$ | 274 GPa | 4 187 m/s | 3 890 m/s |
| **Copper** | 0.343 | 8 960 kg/m$^3$ | 48 GPa | 2 315 m/s | 2 162 m/s |
| **304 Steel** | 0.285 | 7 900 kg/m$^3$ | 80 GPa | 3 223 m/s | 2 982 m/s |

*Table 4.8: Calculated shear and Rayleigh wave speeds from calibration sphere materials [26].*

It is worth noting that steel does not satisfy the criteria of having a Poisson ratio of more than 0.3. However, his exercise is only to see if this might be an explanation and the number calculated for the Rayleigh wave speed does not need to be highly accurate. For two of the sphere materials, formula 13 needs to be changed slightly to calculate the expected delay between direct reflection and the first circumferential wave. The reason the formula needs to be altered is that the Rayleigh wave moves faster than the longitudinal wave in the water. The Rayleigh wave propagating from point b will arrive at point c earlier than the wave traveling through the water. This was not the case when considering creeping waves, as the velocities of the two waves were the same and the wave propagating from point b has further to travel.

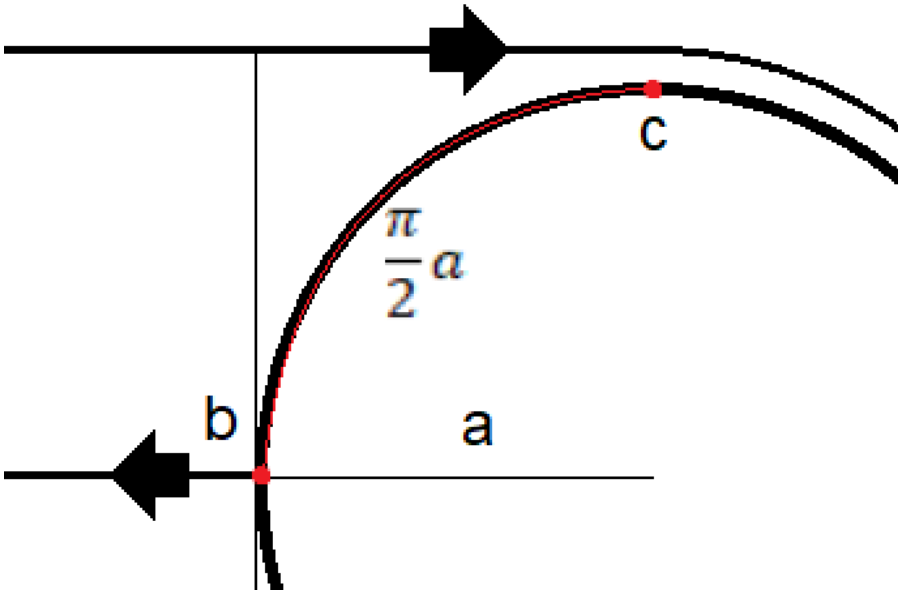


*Figure 4.105: Path travelled by Rayleigh wave alone sphere surface.*

This is true for the calibration spheres made from Steel and tungsten carbide. For this formula to be accurate. The material needs to have Rayleigh wave speed higher than $\frac{\pi}{2}$ times that of speed of sound in water. This comes out to around 2 333 m/s. This means that for copper, formula 13 is used as is.

$$\frac{a}{c_w} > \frac{\frac{\pi}{2}a}{c_R}$$

*4.43*

Where a is the radius of the sphere, $c_w$ is the longitudinal wave speed in water and $c_R$ is the Rayleigh wave speed for the material of the sphere. Meaning the first echo detected will be the one coming from the Rayleigh wave propagation from point b. The same argument can be used to argue that the earliest echo will also emanate from point b. The new formula for the expected time delay between direct echo and first circumferential echo is then this.

$$\Delta t_{Rw} = \frac{2\pi a}{c_R}$$

*4.44*

A table can then be set up so compare the estimate for time delay due to Rayleigh waves and the measured delays.

| Material | Diameter | $c_R$ | $\Delta t_{Rw}$ | Measured delay |
|---|---|---|---|---|
| **Tungsten** | 22 mm | 3 890 m/s | 17.77 µs | 16.98 µs |
| **Copper** | 16 mm | 2 162 m/s | 22.41 µs | 20.61 µs |
| **Steel** | 20 mm | 2 982 m/s | 21.07 µs | 19.12 µs |

*Table 4.9: Calculated Rayleigh wave delay compared to measured delay.*

The calculated delays between peaks are now much closer to the observed delays. Although the measured delays are consistently slightly shorter that the calculations suggest they should be. This might be due to a slight oversimplification done previously, where the shortest delay was found via assuming that the shortest path the wave could take starts at point b on Figure 30, since it was shown to be faster than from point c for two of the materials. This might not be the case, as a Rayleigh wave aminating from a point between b and c may arrive first. To investigate this, the function for delay between direct echo and circumferential was plotted for all three spheres.

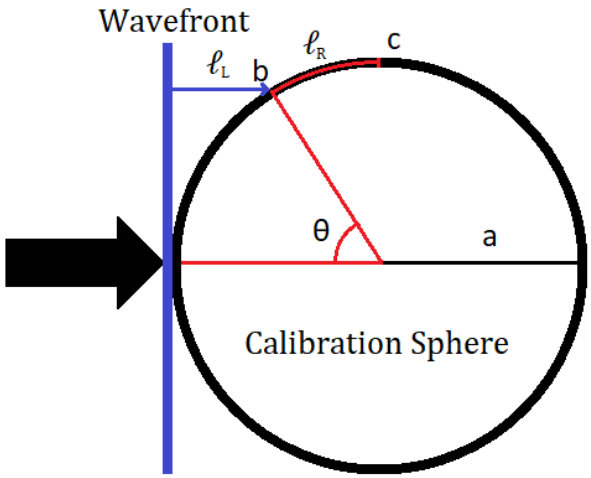


*Figure 4.106: Adjusted path travelled by Rayleigh wave along sphere surface as a function of excitation location.*

Point b can now be moved and its position is indicated by the angle θ. The delay is then worked out similarly to formula 13. $\ell_L$ needs to be covered by the longitudinal wave moving at c, the speed of sound in water. $\ell_R$ will then be covered by the emerging Rayleigh wave. The Rayleigh wave will the propagate along the back half of the sphere and then the first scenario will occur again as the Rayleigh wave will produce a longitudinal wave propagating towards the transducer, the first of which will arrive from a point a similar position as point b, only on the opposite hemisphere. With these assumptions the final formula for the delay is as follows.

$$\Delta t_{Rw2} = \frac{2a(1-\cos(\theta))}{c} + \frac{2a(\pi-\theta)}{c_R}$$

*4.45*

The first part of the equation represents the time taken for the longitudinal wave in the water to reach point b from the front of the sphere, which also happens on the way back. Where a is the diameter of the sphere and $\theta$ is the angle. The second part represents the time the resulting Rayleigh wave takes to travel the remaining distance around the sphere. The resulting time delay will be slightly shorter than previously found. It is important to find shortest path for the circumferential wave to take as that is the first echo we will receive and can time. We will not be able to determine the arrival times for any

other path than then the first one as the signals for these other paths will be somewhere in the echo, but we don't know where. Same for the direct echo coming from the front of the sphere we know the first arrival must be from the front of the sphere, previously point b, as it is the shortest path and will therefore arrive first, this Is why we compare the arrival times of these two echoes and not any other. Even though they are present.

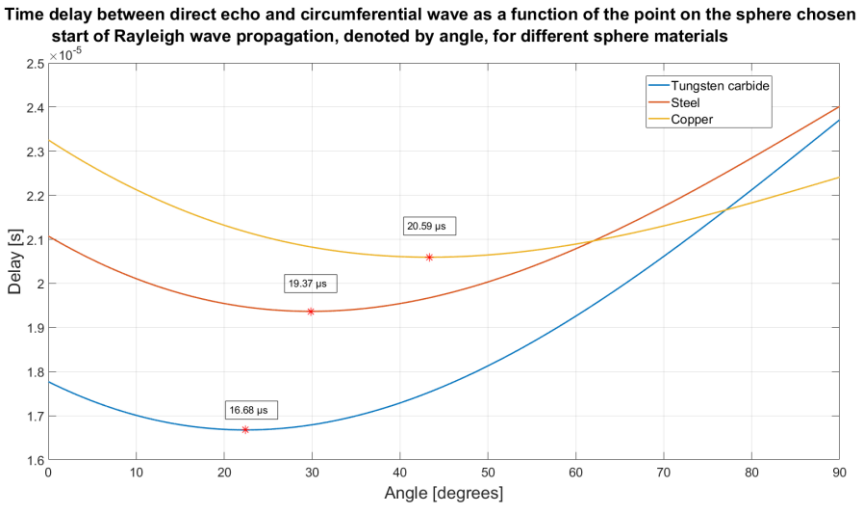


*Figure 4.107: Rayleigh wave delays as a function of excitation location for three calibration sphere materials.*

One more consideration needs to be made before these numbers can be compared to the ones measured. Not all angles of incidence can excite Rayleigh waves, meaning that not all angles on the plot will be valid as a starting location for Rayleigh waves. Rayleigh waves are only exited at or above a certain critical angle. Which means that the wave front hitting the front of the sphere won't excite Rayleigh waves since it has an incident angle of 90°. The critical angle for Rayleigh waves is

$$\sin\theta_R = \frac{Cw}{C_R} \tag{4.46}$$

where $Cw$ is the longitudinal wave speed in water, $C_R$is the Rayleigh wave speed in the material. Solving this equation gives us a lower bound for where the Rayleigh waves can start. The table displays the critical angle for exiting Rayleigh waves as well as the optimal angle which was found to yield the shortest delay.

| Material | $\theta_R$ | $Optimal\ angle$ |
|---|---|---|
| **Tungsten carbide** | 22.42° | 22.42° |
| **Copper** | 30.27° | 30.27° |
| **Steel** | 29.84° | 29.84° |

*Table 4.10: Critical Rayleigh angle compared to angle of shortest delay.*

As it turns out, solving these two equations gives the same answer. The critical angle and the optimal angle are the same for any sphere of any size and material. This also means that the results found can be used as the optimal angle is larger or equal to the critical angle.

| Material | Diameter | $\Delta t_{Rw2}$ | Measured delay |
|---|---|---|---|
| **Tungsten carbide** | 22 mm | 16.68 µs | 16.98 µs |
| **Copper** | 16 mm | 20.59 µs | 20.61 µs |
| **Steel** | 20 mm | 19.37 µs | 19.12 µs |

*Table 4.11: Adjusted Rayleigh wave delay compared to measured delay.*

From this table one can see that the delays measured between the direct echo and the first circumferential echo is close to the one estimated by Rayleigh waves. The estimation holds true even for spheres of different sizes and materials. With this result, the conclusion reached is that these recurring echoes likely come from surface waves in the sphere itself that radiates sound towards the transducer once every time the wave circumnavigates the sphere, making for a periodic but decaying echo coming from calibrations spheres ensonified by the frequencies used in these experiments, 500 kHz.

### 4.7.3 Calibration sphere oscillating target strength

As seen during the triangulation experiments where the position of a calibration sphere was attempted to be found and its target strength used to characterize the directivity of the transducers. The target strength of the sphere at a depth lower that the one of the transducers being characterized would oscillate as a function of depth. This was first observed when the amplitudes of the echo returning from the target sphere in all its positions were plotted. The plot shows that the amplitude of the echo follows the expected values for position where $z_{sphere} < z_{transducer}$. Those values following the shape of the previously measured directivity of the transducer. However, as soon as $z_{sphere} > z_{transducer}$, the amplitude of the echo has peaks and valleys while still being well within the transducer's main lobe. This phenomenon was first attributed to a mistake in the amplitude calculation software, but after reviewing two signals of almost the same depth having wildly different amplitudes in their steady state, it was confirmed to be a real effect.

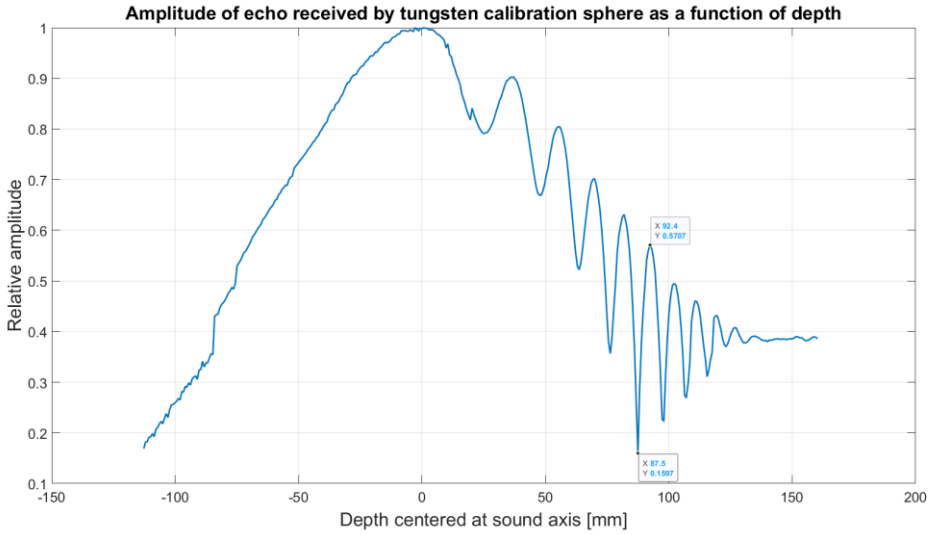


*Figure 4.108: Amplitude of echo from tungsten carbide calibration sphere as a function of depth.*

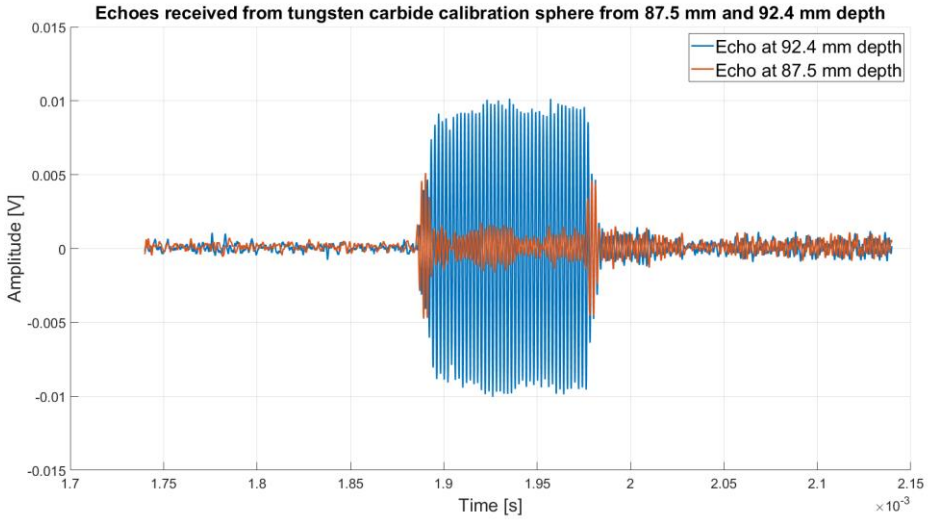


*Figure 4.109: Two echoes received from tungsten carbide calibration sphere from two different depths.*

After further investigation the same effect was observed at several different distances, signal amplitudes and frequencies. The phenomenon had not been observed earlier when testing with a hydrophone. To remove as many variables as possible, the calibration sphere was swapped for a hydrophone and large the transducer mount plate was swapped out for the free field transducer mount to exclude any effects coming from the sphere, its fishing line, or the baffle around the transducer. The hydrophone was then placed at the same y coordinate as the transducer moved from being above the transducer in depth to below it, in steps. The steps where of length 0.5 mm and the hydrophone travelled 600 mm. At every step a 60 second average of the signal was taken and saved. All the 1201 signals where then extracted, and their steady state amplitudes measured. The plot for these amplitudes as a function of depth is shown below.

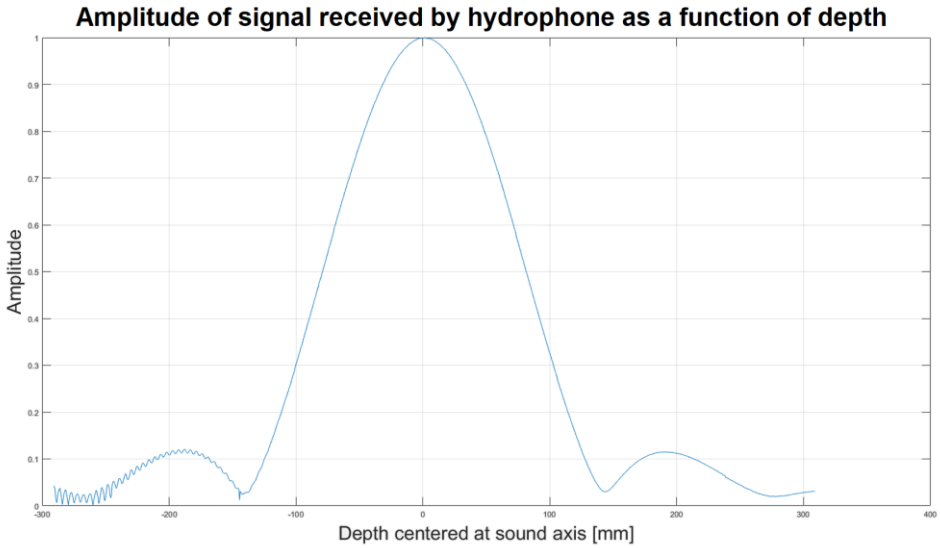


*Figure 4.110: Amplitude of signal received by hydrophone as a function of depth.*

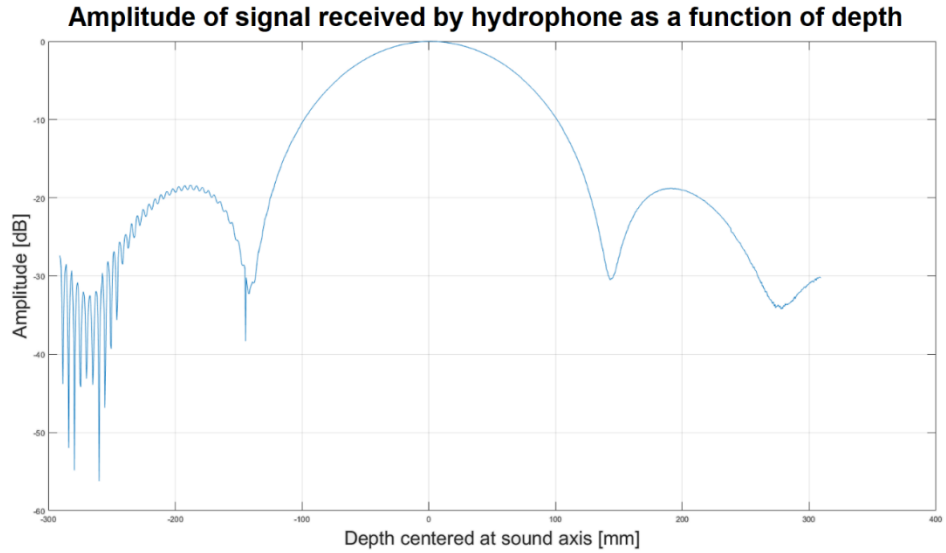


*Figure 4.111: Amplitude of signal received by hydrophone as a function of depth in decibel.*

The phenomenon could not be recreated under these circumstances and the variables could then be introduced. First, the calibration sphere was used as the target again. The same set-up was run as when using the hydrophone. The plot showing the amplitudes from the echoes received from the sphere is shown below.

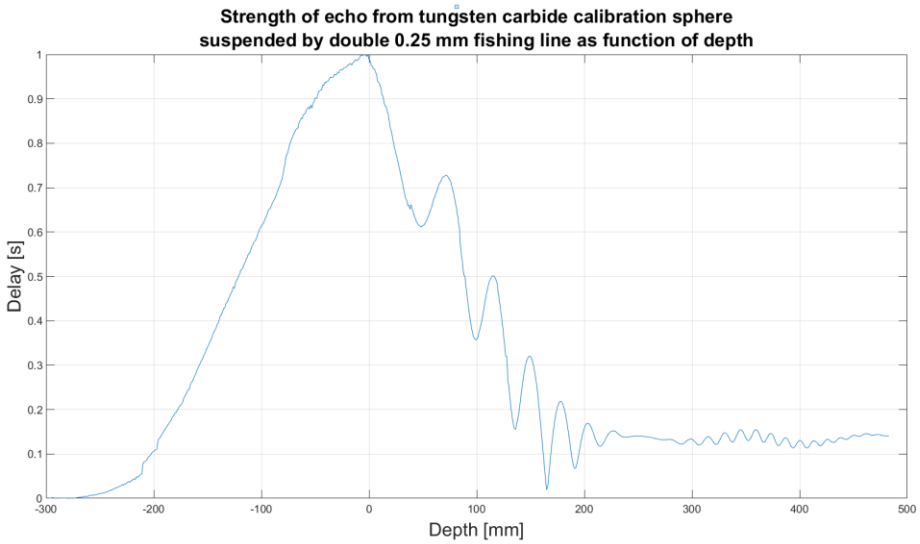


*Figure 4.112: Amplitude of echo received from tungsten carbide calibration sphere as a function of depth.*

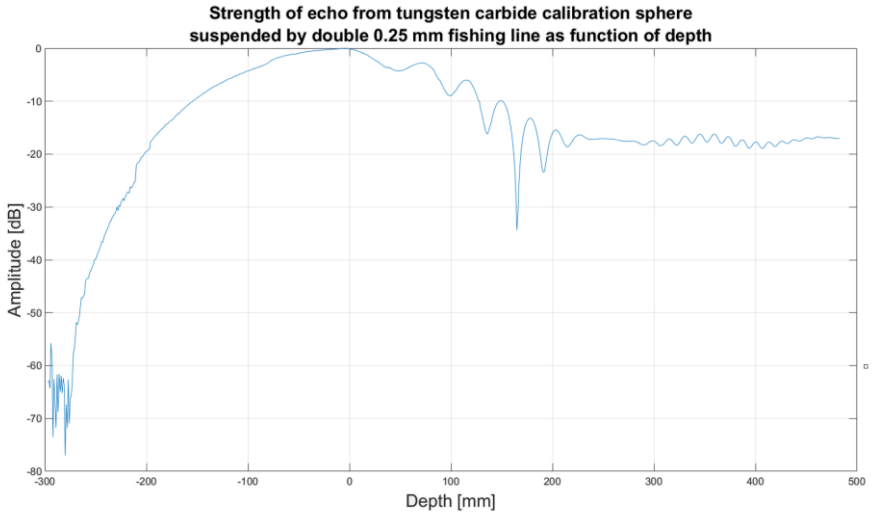


*Figure 4.113: Amplitude of echo received from tungsten carbide calibration sphere as a function of depth in decibel.*

The phenomenon could now be seen at a high level of detail. Knowing that the calibration sphere was the only new variable and the fact that the phenomenon is not symmetric, despite the transducer directivity being symmetric, points to one conclusion. The fishing line using to suspend the sphere in the water is not symmetrical and in fact has a knot and line coming of it on the top. This suspension method seems to greatly interfere with the echo returning to the transducer when the sphere is lower in depth than the transducer. This is also the point where the top of the sphere, as well as the knot and line, become directly visible to the transducer.

Comparing the measured echo as a function of depth and compare it to the one observed when using a hydrophone, the effect is clear. The differences between the plots highlights any effects the calibration sphere may have on the signal sent by the transducer before returning it, which will in turn effect the apparent directivity one might be trying to decern by using such a sphere. In order to compare the two some compensation needs to be done. The amplitudes have been normalized to be

equal to one at their peaks. The tests were done at slightly different distances, 91 cm and 96 cm. The measurements taken at the closest distance were therefore stretched in the x direction to reflects the slightly narrower directivity observed at that distance. The experiment involving the calibration sphere is also subject to the two-way directivity of the transducer since the signal is both sent and received by the transducer. This is not the case while using a hydrophone. The signal received by the hydrophone has been squared before plotting in order to have comparable signals. This means that the plot effectively shows the two-way directivity of the transducer. The reason the signals from the calibration sphere were not square rooted instead is that then the amplitude of the echo coming from the fishing line would then have been elevated compared to the signal from the sphere. The echo from the fishing line alone can be seen at depths of around 250 mm and 500 mm, where the echo from the sphere is negligible due to being in troughs of the directivity, while the echo from the fishing line is at constant strength as it is always ensonified by the main lobe of the transducer. Squaring the directivity measured by the hydrophone ensures that the ratio between sphere echo strength and fishing line echo strength remain accurate.

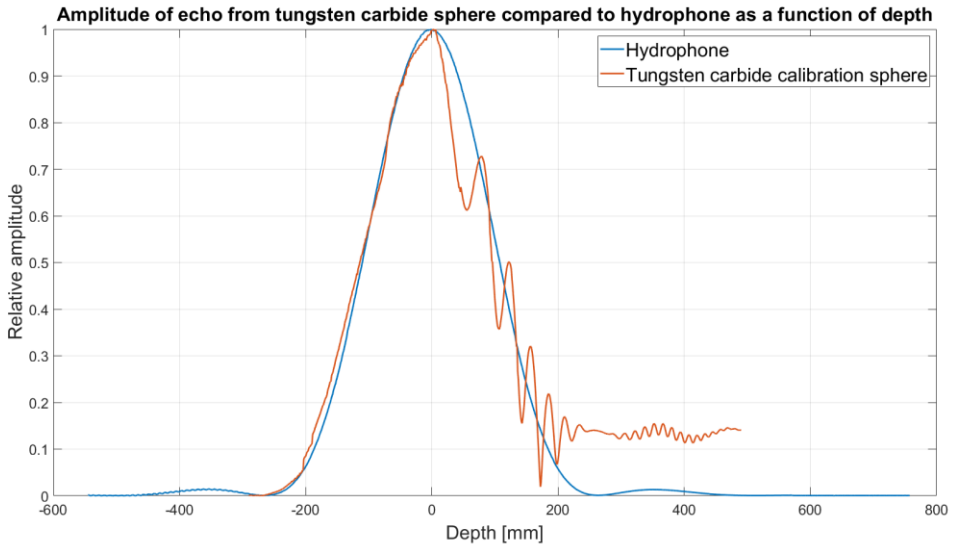


*Figure 4.114: Amplitude of echo from tungsten carbide calibration sphere compared to hydrophone as a function of depth.*

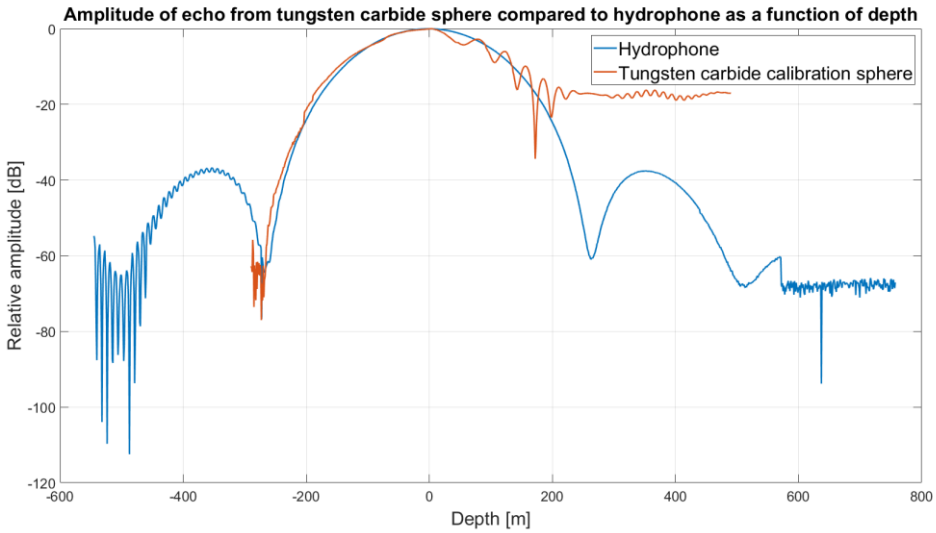


*Figure 4.115: Amplitude of echo from tungsten carbide calibration sphere compared to hydrophone as a function of depth in decibel.*

### *4.7.3.1 Effect of calibration sphere suspension method*

In all the experiments done using calibration spheres in this study, the method used to suspend the sphere in water while influencing the measurements as little as possible, was using fishing line. All the calibrations spheres were tied up with, or in some cases glued to, a 0.25 mm thick fishing line. The idea is that the fishing lines thickness and material will make it so that any sound wave traveling through it will not reflect the sound and therefore not change the measurement by being present. The fishing line does of course reflect some sound, but not enough to significantly affect the results of the experiments. Other methods of calibration sphere suspension have been suggested and researched. In this work however, only the effects of the 0.25 mm fishing line used will be discussed. This is also the method used by the Centre for Marine Research when using these spheres to calibrate their echosounders on ship. The effects of the fishing line being present was first observed when doing the triangulation experiments described in section 4.6.5. When the lower half of the directivity showed some strange patterns, the first proposed explanation was that the knot of fishing line on top of the sphere was the culprit. No asymmetries, other than the fishing line were present during the measurements of the transducer's directivity. After this some further experiments were conducted in order to find the effects of the fishing line suspension method, its severity as well as when it shows up.

#### 4.7.3.1.1 Fishing line direct echo interference

If a taut fishing line gives of a significant echo when ensonified, this can interfere with any measurements taking using calibration spheres suspended using fishing line. To investigate, a calibration sphere was suspended by a fishing line and placed at the bottom of the experiment tank, such that the line was taut. A transducer was then placed about 40 cm below the water's surface, pointing at the line. The distance between the taut line and the transducer face was 85 cm. The

calibration sphere at the bottom of the tank was far enough out on the transducers directivity to not register when measured.

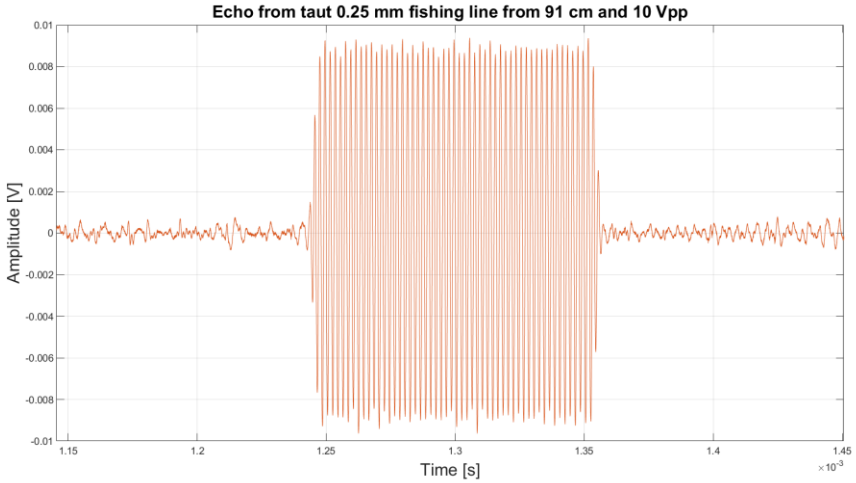


*Figure 4.116: Echo received from taut fishing line.*

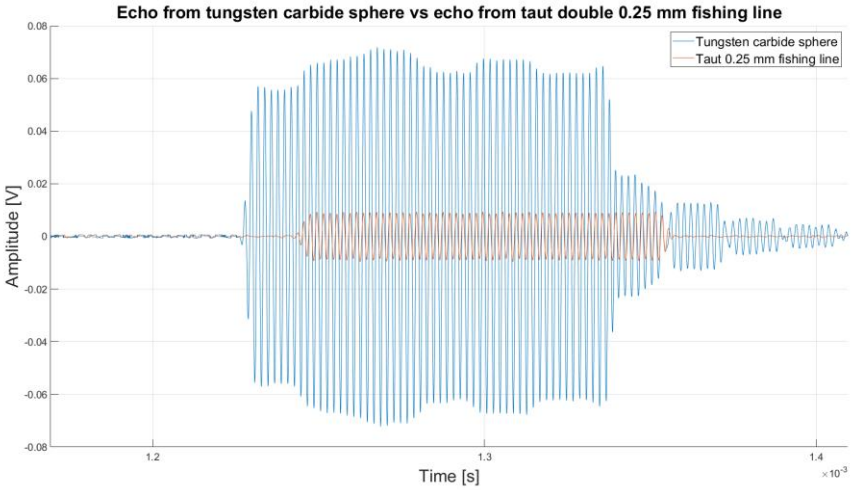


*Figure 4.117: Echo received from taut fishing line compared to tungsten carbide calibration sphere.*

The reason the two signals do not align in time is because of the physical size of the calibration sphere, the sphere is slightly closer to the transducer than the fishing line is. The peaks of the fishing line echo were recorded at around 9 mV, while the echo from the calibration sphere peaks at around 60 mV. Doing a quick comparison will reveal the impact interference between them can have. The echo from the fishing line has an amplitude $\frac{9\ mV}{60\ mV} = 0.15$ times that of the echo from the sphere on the sound axis. This ratio will only grow as the sphere is moved further from the sound axis and its amplitudes weakens, while the amplitude from the fishing line remains constant. Since the frequencies are the same for both signals, during perfect destructive and constructive interference, the combined echo should then oscillate by as much as 9 mV in this set-up.


*Figure 4.118: Jump in amplitude in echo from tungsten carbide calibration sphere.*

During this jump the amplitude changes by 30.14 % of the peak amplitude measured, which was around 60 mV as discussed earlier. Meaning the signal increased and the decreased by around $\frac{0.3014}{2} 60\ mV = 9.04\ mV$. Which is what was expected to be the maximum change in amplitude due to fishing line echo interference. It is true that points measured between are not at the same depth and the jump is therefore not as severe as this, but it is also true that aliasing has probably hidden some of the true peaks and troughs.

If the interference between the echo from the calibration sphere and the echo from the fishing line I the true cause of the observed oscillations, then adding a fishing line echo to a directivity measured by hydrophone should show a similar phenomenon. Since the echo from the fishing line comes mostly from the part of the line on the sound axis, this echo can be added to signal measured by a hydrophone only when it is below the sound axis in depth. A hydrophone in this scenario, is simulating a calibration sphere without any fishing line suspending it. When adding the expected echo from a taut fishing line without a calibration sphere, the results should resemble the ones observed when suspending a sphere using the fishing line.

The signal representing the fishing line alone was chosen to be the signal shown in Figure 41. This is the signal from the fishing line while suspending a tungsten carbide calibration sphere. The sphere was in this instance placed deep enough in the water column to not give off any distinguishable echo as it was far from the centre of the transducer's directivity. This signal was then added to some of the signal received by the hydrophone during its testing done earlier in this section. All the signals received while the hydrophone was placed deeper than transducer, had the fishing line echo added to it, to simulate the fishing line coming into "view" of the transducer. The fishing line echo was also weight slightly such that its echo was weaker about 0 mm depth, relative to the transducer. This is to simulate the fact the fishing line does not yet cover the entire main lobe as this depth and is

therefore weaker than when the calibration sphere, or hydrophone, is at a lower depth, when more of the fishing line is hit by the transducers sound waves.

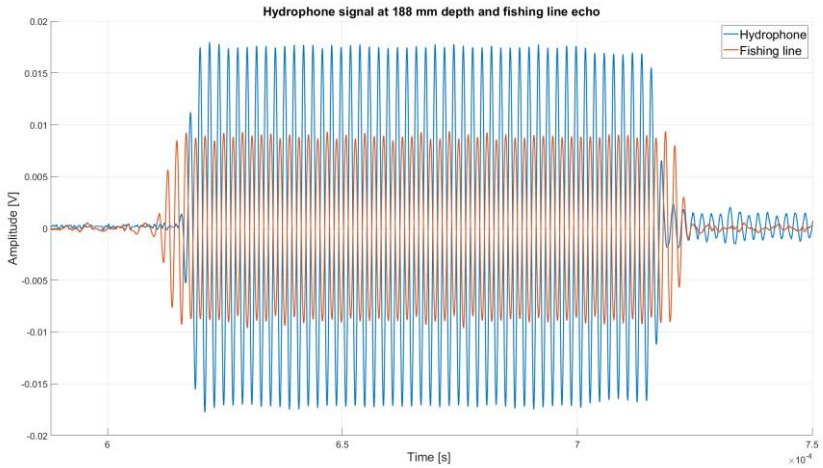


*Figure 4.119: Hydrophone signal ay 188 mm depth and fishing line echo.*

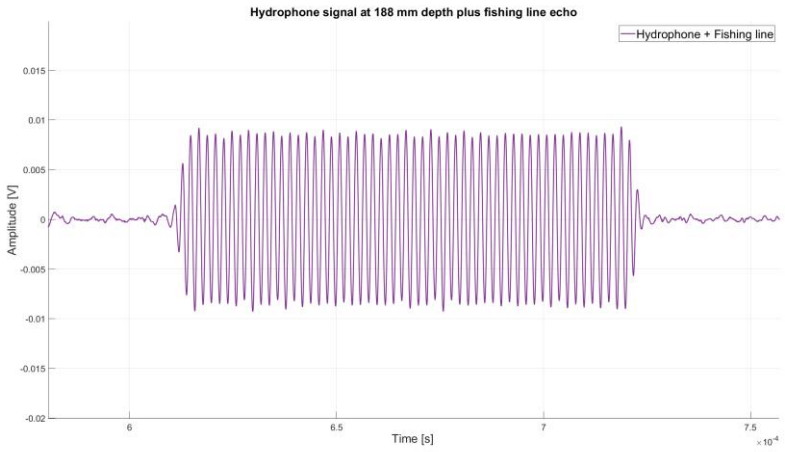


*Figure 4.120: Hydrophone signal ay 188 mm depth plus fishing line echo.*

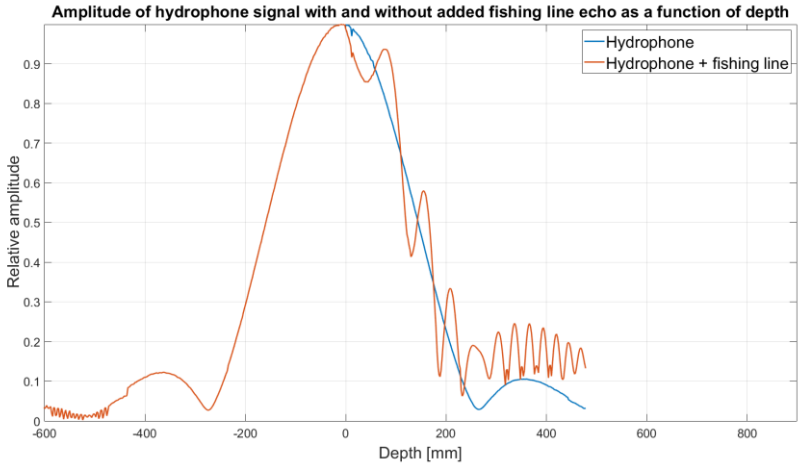


*Figure 4.121: Amplitude of signal received by hydrophone with and wothout echo from a taut fishing line added.*

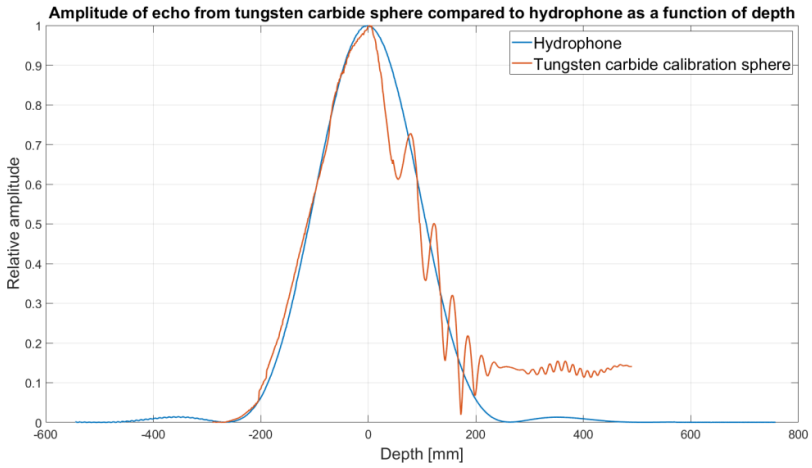


*Figure 4.122: Amplitude of echo from tungsten carbide calibration sphere compared to hydrophone as a function of depth.*

The results show a similar effect to the one observed when using a suspended calibration sphere, although the two are not directly comparable as the calibration sphere and fishing line are subject to the two-way directivity of the transducer whilst the signal received by the hydrophone is only subject to the one-way directivity. This is why the two scenarios are not in the same plot, as their values shouldn't be compared, only their shapes and interference patterns. The interference pattern at the first side lobe has a higher amplitude in the theoretical case, this is due to the amplitude of the hydrophone signal in the side lobe is higher as it is only subject to the one-way directivity. While the amplitude of the echo from the calibration sphere is much smaller and therefore, so is the amplitude of the interference. This test gives strength to the hypothesis that the direct echo from the fishing line is what's causing the oscillating echo amplitude measured when using a suspended calibration sphere.

#### 4.7.3.1.2 Calibration sphere rotation effects

Using the 22 mm tungsten carbide sphere with the same fishing line configuration as used by IMR during their calibrations, the sphere was suspended in water and rotated while a transducer ensonified the sphere from a close distance. The strengths of the echoes were recorded and plotted as a function of the angle the sphere was rotated. The sphere was rotated 360 degrees and a measurement was taken every 1 degrees, making sure to wait a while before taking the measurements to ensure the sphere was completely stationary.

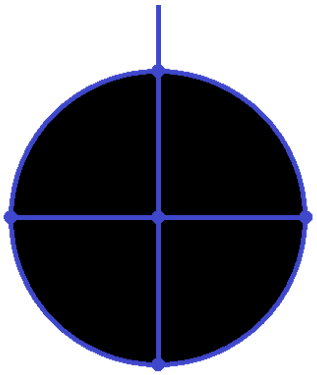

*Figure 4.123: Schematic of IMR's fishing line suspension method.*

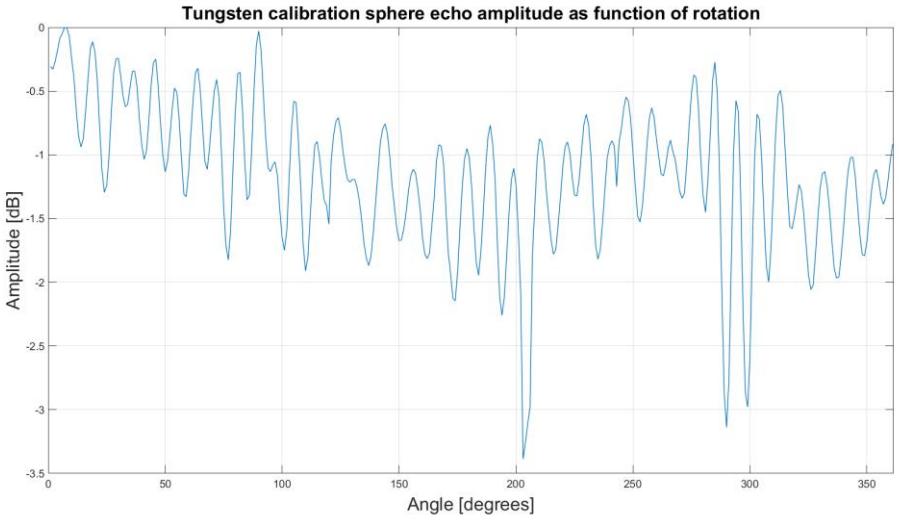


*Figure 4.124: Amplitude of echo from tungsten carbide calibration sphere as a function of its rotation.*

There is a clear pattern in the amplitudes of the echoes received from the sphere. The amplitude oscillates with a set frequency. With 38 peaks in 360 degrees. The average frequency of the oscillations is about 0.105 oscillations per degree or 9.5 degrees between oscillations. This seems strange as the configuration of the fishing line has 90-degree symmetries. No clear pattern in the amplitudes seem to repeat every 90 degrees. However, there is also a lower frequency present that seems to be around 180 degrees between oscillations. At three of the angles the amplitude drops significantly and the reason for this is unknown but might be some destructive interference from various parts of the fishing line set-up. The reason why the amplitude at 0 degrees doesn't match the amplitude at 360 degrees is not clear either. The Experiment was repeated, and a similar result was observed. Note that the three troughs are present in both experiments and are spaced about 90 degrees apart.

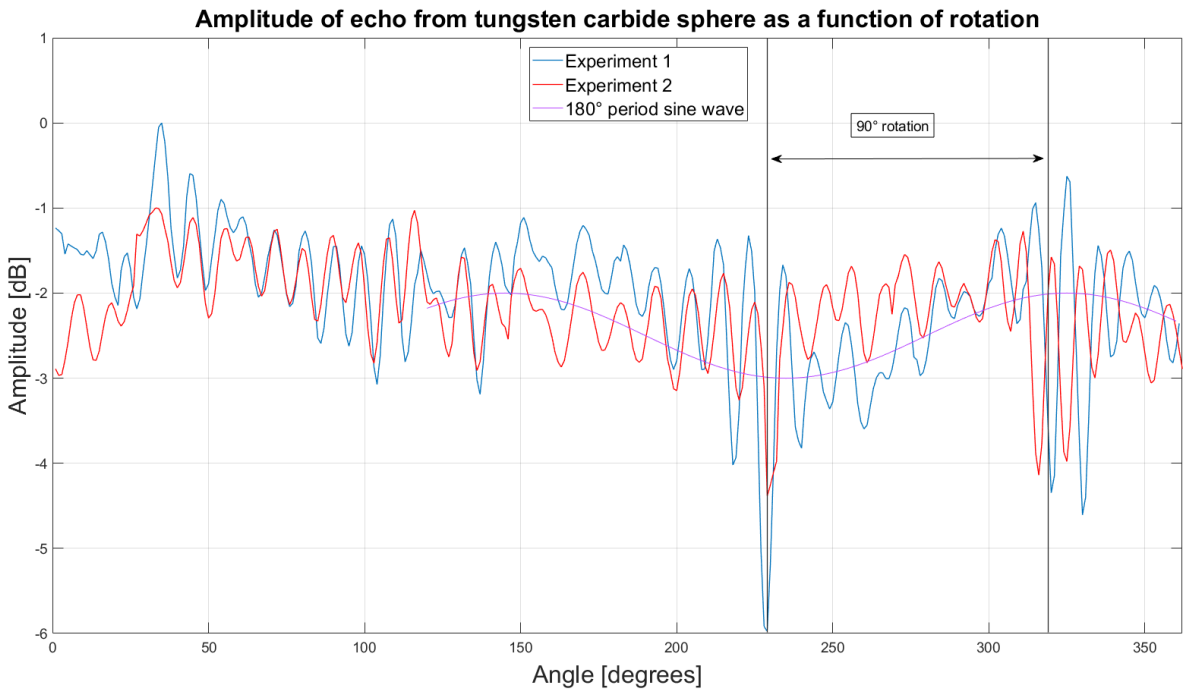


*Figure 4.125: Amplitude of echo from tungsten carbide calibration sphere as a function of its rotation done twice.*

The locations of the peaks and troughs, as well as their periodicity is very similar between observations, meaning the somewhat strange patterns are repeatable and actual.

The three troughs present in both experiments might be caused by the fishing line being at the front of the sphere as the wavefront sees the sphere, therefore dampening some of the direct echo and scattering some of the wave's energy in other directions than straight back. The troughs are spaced apart as much as the vertical fishing lines are, by 90 degrees. It is unclear why these troughs show up on only two locations when there are four vertical lines of fishing line running down the sphere. Perhaps the horizontal fishing line interferes at some rotations but not others, as it does not circumnavigate the sphere in the same plane as the sphere rotates. That is to say that the horizontal fishing line does not run completely parallel to the direction of the incoming sound wave.

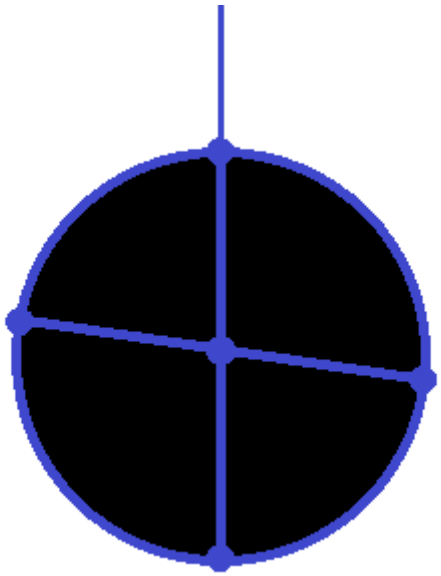

*Figure 4.126: potential offset in fishing line configuration.*

Tracing the position of the point horizontal fishing line at the front of the sphere as it rotates would trace out a sine wave with a period of 360 degrees. This is perhaps part of the reason why there is a periodicity in the echoes which have this period halved. If only the fishing lines distance from the equator of the sphere affects the echo and not the direction of misalignment, then the periodicity of changes to be 180 degrees. The greatest amplitude in echo is perhaps when the horizontal fishing line is the farthest from the equator, this happens twice, and therefore gives two peaks to the amplitude of the echo over the 360 degrees rotation. The horizontal and vertical lines may also be misaligned in numerous other ways which can affect the strength of the echoes, as there are patterns in the target strength plot that don't yet have any explanations.

The result of the experiments show that the orientation of the sphere can change its target strength dramatically, by as much as 3-6 decibel. As little as 4 degrees of rotation can change the target strength of a tungsten carbide calibration sphere by as much as 3-5 decibel. This is a significant difference and is very hard to compensate for as the change in target strength is very sensitive to angle and the current rotation of the sphere will be unknown while being used for calibration on ship.

#### 4.7.3.1.3 Fishing line suspension method effects

As seen in the previous section, the rotation of a tungsten carbide sphere suspended via fishing line can greatly affects its target strength. This was also investigated on other spheres, using different suspension methods. A steel sphere was suspended with a single loop of fishing line. Tied at the top. Some glue was used to prevent the sphere from slipping out of the loop. A copper sphere was suspended such that three lines wrapped around it. This arrangement did not use a knot at the top but did involve some glue at the bottom of the sphere.

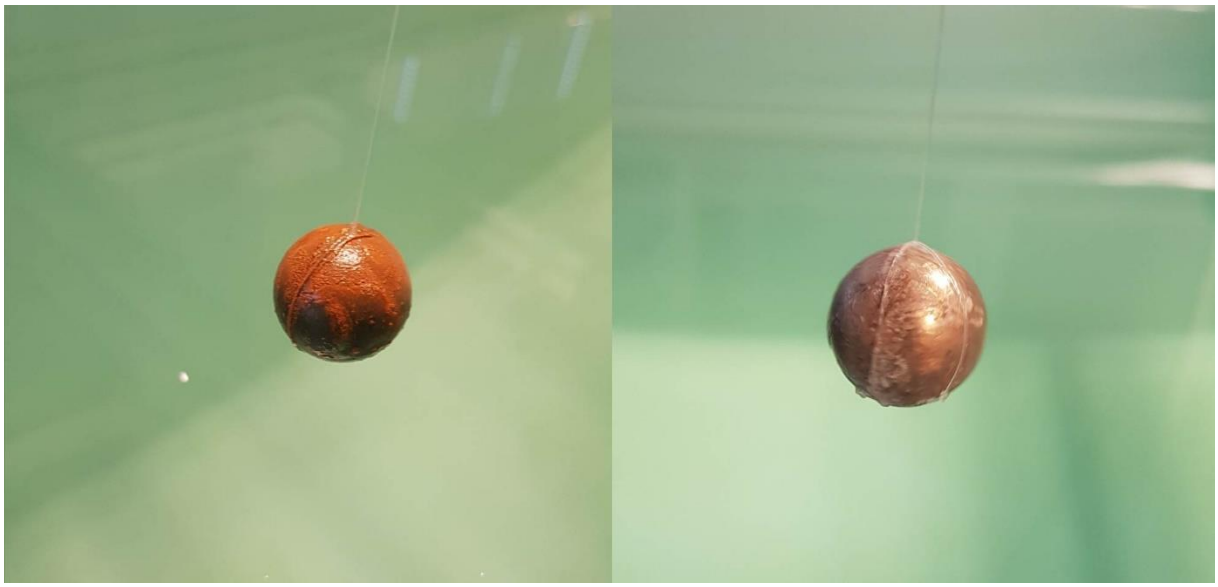

*Figure 4.127: Steel calibration sphere (left) and copper calibration sphere (right) using different suspension methods.*

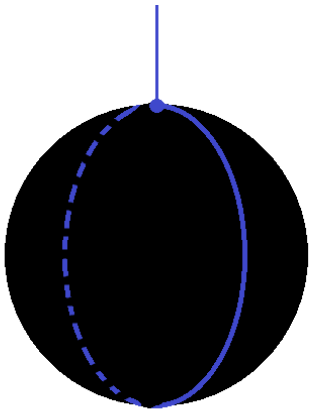

*Figure 4.128: fishing line configuration used for steel sphere.*

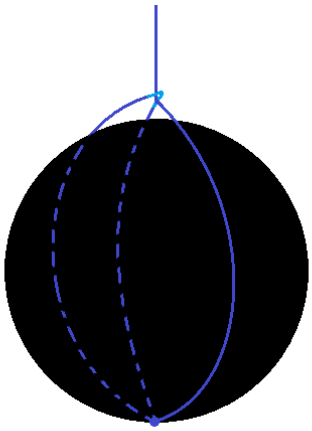

*Figure 4.129: fishing line configuration used for copper sphere.*

A 10-Volt peak to peak signal of 3 cycles was sent through the 500 kHz transducer pointed at the spheres. An echo was recorded for both spheres at two different orientations, 180 degrees apart. For the steel sphere the two orientations were similar as orientation one had one of the hemispheres created by the fishing line pointed at the transducer. Rotating this by 180 degrees gives an almost identical positioning of the fishing line around the sphere. As such there was no difference between the echoes recoded at the two positions. For the copper sphere however, one of the orientations had the single vertical fishing line pointed towards the transducer while position two had the two closer vertical fishing lines pointed at the transducer. The Figures below show how the fishing line was oriented, with the face depicted is the one facing the transducer. The Figure shows the first

orientation while the second orientation is a 180 degrees rotation about the x-axis from orientation 1, for both spheres.

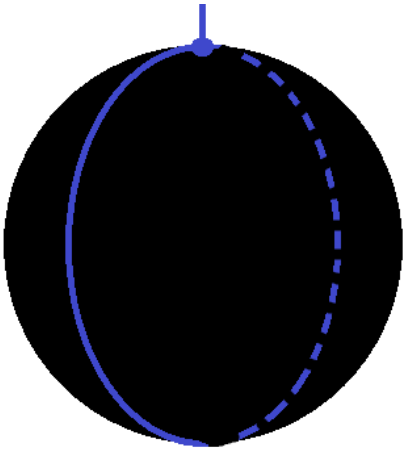

*Figure 4.130: suspended steel sphere viewed from transducer, orientation 1.*

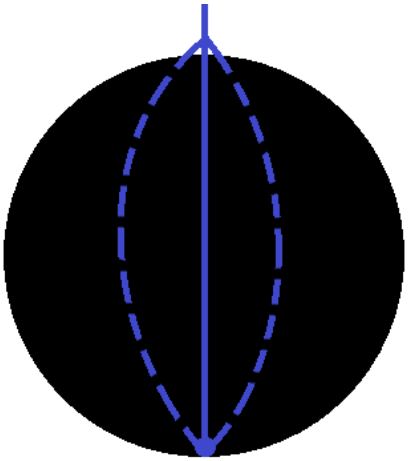

*Figure 4.131: Suspended copper sphere viewed from transducer, orientation 1.*

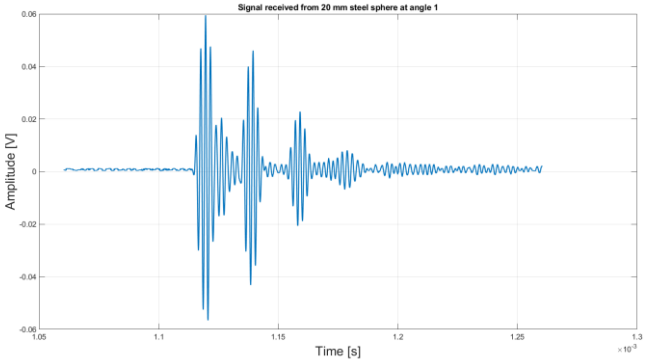


*Figure 4.132: Echo received from steel sphere orientation 1.*

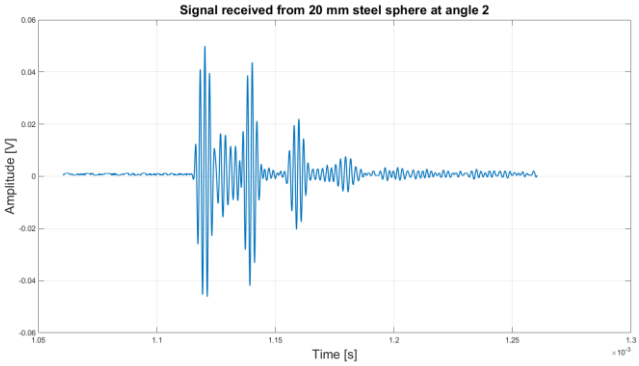


*Figure 4.133: Echo received from steel sphere orientation 2.*

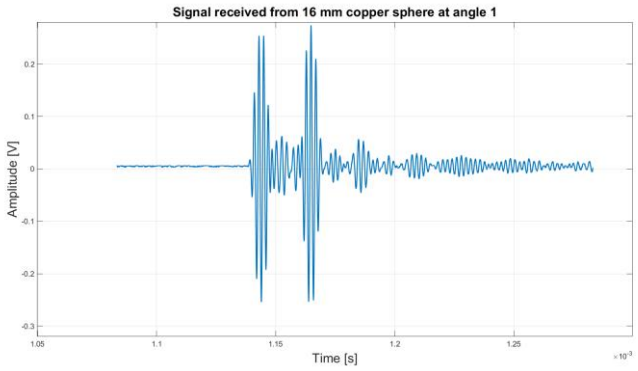


*Figure 4.134: Echo received from copper sphere at orientation 1.*

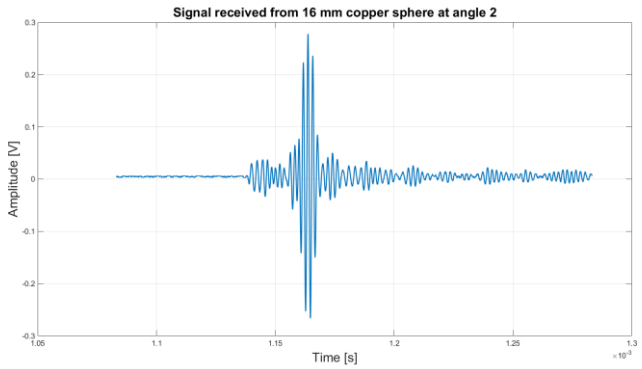


*Figure 4.135: Echo received from copper sphere at orientation 2.*

The echoes received by both spheres at both orientations are shown above in Figure 4.132-Figure 4.135. The amplitude of the first echo, the direct reflection is heavily impacted by the positioning of the fishing line relative to the incoming sound wave. The rest of the peaks in the echo, hypothesised to come from surface circumferential waves, seems unaffected by the fishing line placement. This is perhaps expected as the wave travels in the surface of the sphere and not in the water, but nothing conclusive can be drawn about this from this short experiment. The echoes received from the steel sphere are as expected very similar as the two positions are practically identical. The timings and amplitudes of the periodic peaks seem unaffected by the fishing line. The line is not on the front face and then doesn't seem to affect the direct echo. The fishing line also doesn't seem to affect the rest of the peaks. Similar to what was observed using the copper sphere.

# 5 Conclusion and further work

This chapter contains the conclusions drawn from the results of the calculations and experiments done in this thesis as well as suggestions for further work to be done on the subject.

## 5.1 Conclusion

In this thesis, a triangulation method for estimation of the echosounder two-way equivalent beam solid angle has been investigated and some its potential problems explored and discussed. The method shows promise in its ability to detect calibration sphere locations given a good set-up. The most important factors that play into the potential inaccuracy of the triangulation were found to be the area covered between the three transducers, meaning the further apart they are placed the lower the uncertainty of the targets position. Any uncertainty in the sound speed of the medium was seen to only affect the estimated distance to the target, the z-coordinate, and not the angle to the target, meaning its effect on the beam pattern and $\psi$-estimate should be minimal. The accuracy of the triangulation method was high under the conditions used in this study, only being of by a few mm at a range of 2 meters, high enough to achieve a good beam pattern and $\psi$-estimate.

The effects of bafflements on immersion transducers' directivity were seen to be a lowering of side lobe levels and a widening of the main lobe. To account for this when doing $\psi$-estimates, a parameter was introduced to the piston model estimate of the transducers beam pattern. This new parameter better models the beam pattern of baffled transducers helping to improve the estimate of $\psi$, compared to standard piston model beam pattern estimates. With enough high-accuracy triangulation measurements the target strengths of calibrations spheres at different locations can be found to map out the beam pattern of several transducers at once, not just the three used for triangulation. With these measurements it is possible to find a function to fit the transducers beam pattern and integrating over this function then gives an estimate of $\psi$ as shown in section 0. The estimated value for $\psi$ for the 500 kHz 25 mm diameter transducers used in this study were found, via the triangulation method to be around 0.008 sr depending on the exact methodology chosen, with little variation. This value concurs with both the simplified formula by Urick [19] and used by ICES [5], equation 4.34, and the theoretical value estimated using the piston model and the estimated derived from measuring the transducers' beam patterns via hydrophone. This suggest the method is accurate in the circumstances of this study and may be viable for scientific echosounder calibration.

In section 4.7 it was observed that when using calibration spheres at 500 kHz the 0.25 mm fishing line suspension configuration can significantly interfere with the reading of the sphere's target strength, interfering with any calibration hoped to be done. When the taut fishing line is suspended normal to the sound axis of the transducers used in this study the amplitude received from the fishing line is

significantly high compared to the signal received from the calibration sphere, making beam pattern and $\psi$-estimation using calibration spheres difficult due to severe and abrupt changes in the apparent target strength of the calibration spheres when suspended by fishing lines. This may also be an issue at lower frequencies, such as the ones used by scientific echosounders on research vessels, which include 333 kHz. Section 4.7 also includes the observed phenomenon of apparent circumferential surface waves around calibration spheres producing periodic echoes which could change the apparent target strength of the calibration sphere.

## 5.2 Further work

It is of interest to use data gathered by IMR during one of their routine calibrations to test out and further develop the triangulation methodology for two-way equivalent beam solid angle estimation, and investigate its practicality, viability and accuracy when implemented in situ. As well as test the methodology using other frequencies such as 18-333 kHz, as is used by IMR on their echosounders [20]. A good method for estimating the main lobe or the entire beam pattern from sphere calibrations in order to achieve an accurate estimate of $\psi$ is needed, as well as a framework for implementing triangulation and $\psi$-estimating into the on-ship calibrations.

Further investigation of the potential interference from fishing line suspension methods on calibration sphere echoes is needed, as in this study the suspension method used in combination with the frequency became problematic. This may or may not be the case as the fishing line in not normal to the sound axis during routine calibration, as well as the frequencies used being lower, this however needs to be investigated. Checking if these effects may affect calibrations done with such sphere suspension methods in the lower frequency bands should be explored. The circumferential surface waves that appear to be present on calibration spheres under the circumstances found in this study may need to be studied further as they also may interfere in target strength measurements of calibration spheres as the resulting, periodic echoes can interfere with the direct echo from the sphere.

# References


[1] A. O. P. R. J. K. F. E. T. a. H. N. P. Lunde, Power-budget and echo-integrator equations for fish abundence estimation, Fisken og Havet, Bergen, Norway: Institute of Marine Research, 2013.

[2] J. S. &. D. MacLennan, Fishieries Acoustics: Thoery and Practice, Blackwell Science Ltd., 2005.

[3] M. Lubis, Acoustic Systems (Split Beam Echo Sounder) to Determine Abundance of Fish in Marine Fisheries, 2017.

[4] C. F. &. N. P. D. Skerritt, Fine-scale acoustic telemetry as an offshore monitoring and research tool Recommended practice, 2015.

[5] D. B. L. B. M. B. E. B. K. C. D. D. R. Demer, Calibration of acoustic instruments. ICES Cooperative Research Report No., 2015.

[6] C. S. &. M. Clay, Acoustical Oceanography: Principles and Applications, New York: J. Wiley & Sons, 1977.

[7] P. M. M. &. K. U. Ingard, Theoretical acoustics, New York: McGraw-Hill, 1968.

[8] D. MacLennan, The Theory of Solid Spheres as Sonar Calibration Targets, Department of Agriculture and Fisheries for Scotland, 1981.

[9] L. K. &. A. Frey, Fundamentals of Acoustics, John Wiley & Sons, Inc., 2000.

[10] Kongsberg Maritime AS, Simrad ek80 wide band scientific echo sounder reference manual release 2.0.0, 2020.

[11] H. P. K. Gudmund Vestnes Kenneth G. Foote, Standard calibration of echo sounders and integrators with optimal copper spheres, Fiskeridirektoratets skrifter, Serie Havundersøkelser, 1983.

[12] R. Korneliussen, Interviewee, *Transducer positions on G.O. Sars.* [Intervju]. 2022.

[13] V. V. Ha, Separating blue whiting (Micromesistius poutassou Risso, 1826) from myctophid targets using multi-frequency methods., 2008.

[14] M. Parseval, “Memoire sur les series et sur l’integration complete d’une equation aux differences, Academie des Sciences, 1806.

[15] Tektrinox, «tek.com,» Tektrinox, [Internett]. Available: https://www.tek.com/en/support/faqs/how-does-scope-calculate-average-when-you-are-ave-mode. [Funnet June 2023].

[16] P. Technology, «picotech.com,» Pico Technology, [Internett]. Available: https://www.picotech.com/data-logger/pt-104/pt-104-manuals. [Funnet June 2023].

[17] P. L. M. V. E. Storheim, Diffraction Correction in Ultrasonic Fields for Measurements of Sound, University of Bergen, Department of Physics and Technology, 2011.

[18] A. Khimunin, Numerical Calculation of the Diffraction Corrections for the Precise Measurement of, Acustica, 1972.

[19] R. Urick, Priciples of Underwater Sound, 3rd edition, New York: McGraw-Hill, 1983.

[20] R. &. O. E. Korneliussen, Verified acoustic identification of Atlantic mackerel, ICES ASC 2004 Theme Session R: New developments in fisheries acoustic, 2004.

[21] X. Lurton, An Introduction to Underwater Acoustics, Springer, 2010.

[22] F. Q. M. Z. &. K. P. X. Li, Software emulation of TOA based ranging with UWB creeping wave around human body, 2016.

[23] A. A. &. S. Chamaani, Estimation of Target Circumferential Size by Backscattered Wave, 2019.

[24] L. G. &. R. S. W.M Telford, Applied Geophysics, Press syndicate of the University of Cambridge, 1990.

[25] P. Malischewsky, Comparison of approximated solutions for the phase velocity of Rayleigh waves (Comment on 'characterization of surface damage via surface acoustic waves'), Nanotechnology, 2005.

[26] O. o. m. f. T. 4. S. S. Steel, «https://www.matweb.com/,» [Internett]. Available: https://www.matweb.com/search/datasheet.aspx?MatGUID=76c67e3dbb45468d8a9268f543656402&ckck=1. [Funnet June 2023].

# Appendices

## A. MATLAB-scripts

### 1. FindSignalFFTAmplitude

```
% FindSignalFFTAmplitude   31.10.22
% Calculates and returns Amplitude of a given frequency in a signal

function [SignalFFTAmplitude] = FindSignalFFTAmplitude(WaveForm, Freq,
SampleRate)


i = 64;
L = i* length(WaveForm);

Y = fft(WaveForm,L);
f = SampleRate*(0:(L/2))/L;

P2 = abs(Y/L);
P1 = P2(1:L/2+1);
P1(2:end-1) = i*2*P1(2:end-1);
FreqIndex1 = find( f >= Freq, 1,  'First');
FreqIndex2 = find( f < Freq, 1,  'Last');
if abs(f(FreqIndex1)-Freq) < abs(f(FreqIndex2)-Freq)
    FreqIndex = FreqIndex1;
else
    FreqIndex = FreqIndex2;
end
plotIndex = find( f > 2*Freq, 1,  'First');
SignalFFTAmplitude = P1(FreqIndex);

end
```

### 2. ExtractSignalxCorr

```
% ExtractSignalxCorr
% Extracts and returns the steady-state part of a received signal using
% cross correlation with the transmitted signal


function [Signal,wfLength] = ExtractSignalxCorr(wf,wf_Input)

Samples = 200000;

[CorrelationStart,lags] = xcorr(wf,wf_Input,Samples/2);
[CorrelationEnd,lags] = xcorr(wf,flip(wf_Input),Samples/2);
```

```
maxCorrelationStart = find (abs(CorrelationStart) ==
max(abs(CorrelationStart)), 1, 'first');
maxCorrelationEnd = find(abs(CorrelationEnd) ==
max(abs(CorrelationEnd)), 1, 'first');

cut = 6500;

wfstart = maxCorrelationStart;
wfend = maxCorrelationEnd;

if wfend-wfstart > 3*cut
    wfstart = wfstart + cut;
    wfend = wfend - cut;
elseif wfend-wfstart < 0
    temp = wfstart;
    wfstart = wfend;
    wfend = temp;
elseif wfend-wfstart < cut
    wfstart = wfstart - cut;
    wfend = wfend + cut;
end

if length(wfend) == 0
    wfend= length(wf);
end

interval = wfstart:wfend;
WaveForm = wf(interval);

Signal = WaveForm;
wfLength = length(WaveForm);
end
```

### 3. PlotPistonModel

```
%PlotPistonModel
%Plots the beam pattern of a transducer by the ka-number and calculates the
%Psi by integrating over the beam pattern

clear H
clear v
clear thetaT
clear phiT

    ka = 26.44;
    y = 1;

     thetaT = [0:0.005:2*pi];
     phiT = [0.00000001:0.001:pi/2];

    %     Beam Pattern
        for i = 1:length(thetaT)
            for j = 1:length(phiT)
               v(i,j) = ka.*sin(phiT(j));
            end
```

```
        end

        H = abs(2*besselj(1, v)./v).^y;

        plot(H)

        Integrand = H.^4.*sin(phiT);

        %     Beam Pattern

        psi = trapz(thetaT,trapz(phiT,Integrand,2))
        plot(psi)
        q = cumtrapz(thetaT,cumtrapz(phiT,Integrand,2));
        plot(q)
```

4. MonteCarloSimulation

```
% MonteCarloSimulation
% Simulated the triangulation method and calculates its uncertainty via
% monte Carlo simulations

clear Px Py Pz

syms T1x T1y T1z T2x T2y T2z T3x T3y T3z Bx By Bz d1 d2 d3

tic

ES200 = [8.144,-0.799, 0]
EC150 = [8.579, -0.473, 0]-ES200
ES333 = [8.331,-0.740, 0]-ES200
ES120 = [8.177,-0.578, 0]-ES200
ES70 = [8.179,-0.275, 0]-ES200
ES18 = [7.703,-0.472, 0]-ES200
ES38 = [7.006,-0.472, 0]-ES200
ES200 = [8.144,-0.799, 0]-ES200



eq1 =  Bx^2 + By^2 + Bz^2 - d1^2 == 0;
eq2 = (Bx-T2x)^2 + (By-T2y)^2 + Bz^2 - d2^2 == 0;
eq3 = (Bx-T3x)^2 + (By-T3y)^2 + Bz^2 - d3^2 == 0;

S = solve(eq1,eq2,eq3,Bx,By,Bz);

% MONTE CARLO SIMULATION %

T1 = ES200;
T2 = ES70;
T3 = ES18;
B = [0,0,20];

c = 1500;

t1 = sqrt((T1(1)-B(1))^2+(T1(2)-B(2))^2+(T1(3)-B(3))^2)/c;
t2 = sqrt((T2(1)-B(1))^2+(T2(2)-B(2))^2+(T2(3)-B(3))^2)/c;
t3 = sqrt((T3(1)-B(1))^2+(T3(2)-B(2))^2+(T3(3)-B(3))^2)/c;
```

```
% Uncertainty %

uT= 0.001;
ut= 0.000001;
uc= 1;

StartTime = datetime
n=10000;
for i=1:n
    T1xU= T1(1) +normrnd(0,uT);
    T1yU= T1(2) +normrnd(0,uT);
    T1zU= T1(3) +normrnd(0,uT);

    T2xU= T2(1) +normrnd(0,uT);
    T2yU= T2(2) +normrnd(0,uT);
    T2zU= T2(3) +normrnd(0,uT);

    T3xU= T3(1) +normrnd(0,uT);
    T3yU= T3(2) +normrnd(0,uT);
    T3zU= T3(3) +normrnd(0,uT);

    t1U= t1 +normrnd(0,ut);
    t2U= t2 +normrnd(0,ut);
    t3U= t3 +normrnd(0,ut);

    cU= c +normrnd(0,uc);

    tempX =
double(subs(S.Bx(2),{T1x,T1y,T1z,T2x,T2y,T2z,T3x,T3y,T3z,d1,d2,d3},{T1xU,T1
yU,T1zU,T2xU,T2yU,T2zU,T3xU,T3yU,T3zU,t1U*cU,t2U*cU,t3U*cU}));
    tempY =
double(subs(S.By(2),{T1x,T1y,T1z,T2x,T2y,T2z,T3x,T3y,T3z,d1,d2,d3},{T1xU,T1
yU,T1zU,T2xU,T2yU,T2zU,T3xU,T3yU,T3zU,t1U*cU,t2U*cU,t3U*cU}));
    tempZ =
double(subs(S.Bz(2),{T1x,T1y,T1z,T2x,T2y,T2z,T3x,T3y,T3z,d1,d2,d3},{T1xU,T1
yU,T1zU,T2xU,T2yU,T2zU,T3xU,T3yU,T3zU,t1U*cU,t2U*cU,t3U*cU}));

    if isreal(tempX) & isreal(tempY) & isreal(tempZ)
        Px(i) = tempX;
        Py(i) = tempY;
        Pz(i) = tempZ;
    end

    if mod(i,100) == 0
        disp([num2str(100*i/n),' % processed'])
        Duration = datetime - StartTime;
        disp('Estimated finish time: ')
        disp(StartTime + (Duration/i)*n)
    end
end

%PLOTTING the result
[muhat,sigmahat]=normfit(Px);
Pxmin=muhat-2*sigmahat;
Pxmax=muhat+2*sigmahat;
text1=sprintf('%.4f +- %.4f\n',muhat,sigmahat);
text2=sprintf('(%.4f,%.4f) \n95 percent interval',Pxmin,Pxmax);
textTotal=sprintf('%s%s',text1,text2);
```

```
Figure;
title("Bx")
histfit(Px,50)
text(Pxmax,n/15,textTotal,'HorizontalAlignment','center')
xlabel('X');

%PLOTTING the result
[muhat,sigmahat]=normfit(Py);
Pymin=muhat-2*sigmahat;
Pymax=muhat+2*sigmahat;
text1=sprintf('%.4f +- %.4f\n',muhat,sigmahat);
text2=sprintf('(%.4f,%.4f) \n95 percent interval',Pymin,Pymax);
textTotal=sprintf('%s%s',text1,text2);

Figure;
title("By")
histfit(Py,50)
text(Pymax,n/15,textTotal,'HorizontalAlignment','center')
xlabel('Y');

%PLOTTING the result
[muhat,sigmahat]=normfit(Pz);
Pzmin=muhat-2*sigmahat;
Pzmax=muhat+2*sigmahat;
text1=sprintf('%.4f +- %.4f\n',muhat,sigmahat);
text2=sprintf('(%.4f,%.4f) \n95 percent interval',Pzmin,Pzmax);
textTotal=sprintf('%s%s',text1,text2);

Figure;
title("Bz")
histfit(abs(Pz),50)
text(Pzmax,n/15,textTotal,'HorizontalAlignment','center')
xlabel('Z');
```

## 5. Triangulation

```
% Triangulation
% triangulates the target position goven the locators and distaances
syms T1x T1y T1z T2x T2y T2z T3x T3y T3z Bx By Bz d1 d2 d3

T1x = 0;
T1y = 0;
T1z = 0;
%
% T2x = fittedmodelT2X.b;
% T2y = fittedmodelT2Y.b;
T2z = 0;
%
% T3x = fittedmodelT3X.b;
% T3y = fittedmodelT3Y.b;
T3z = 0;


% d1 = T1DistancesSphere(x,y) - ts_sphere*C;
```

```
% d2 = T2DistancesSphere(x,y) - ts_sphere*C;
% d3 = T3DistancesSphere(x,y) - ts_sphere*C;

BT.x = PointsListZ(x);
BT.y = PointsListY(y);
BT.z = 0;

eq1 = (Bx-T1x)^2+(By-T1y)^2+(Bz-T1z)^2-d1^2 == 0;
eq2 = (Bx-T2x)^2+(By-T2y)^2+(Bz-T2z)^2-d2^2 == 0;
eq3 = (Bx-T3x)^2+(By-T3y)^2+(Bz-T3z)^2-d3^2 == 0;

S_simple = solve(eq1,eq2,eq3,Bx,By,Bz);

 digits(5);
 B.x = double(vpa(S.Bx(1)));
 B.y = double(vpa(S.By(1)));
 B.z = double(vpa(S.Bz(1)));
```

### 6. EnvelopeMethod

```
% EnvelopeMethod
% Return detected start of signal by envelope method
wf = wf - mean(wf);

startThreshold = 0.10;
endThreshold = 0.10;
peakThreshold = 0.75;

wfmaxpeak = find( abs(wf) == max(abs(wf)), 1,  'First');

WavePartStart = find( x < x(wfmaxpeak)-1.5*(cycles*(1/freq)), 1,  'Last');
WavePartEnd = find( x < x(wfmaxpeak)+1.5*(cycles*(1/freq)), 1,  'Last');
WavePart =  wf(WavePartStart:WavePartEnd);

[yupper,ylower] = envelope(WavePart,800,'rms');

wfpeak1 = find( abs(WavePart) > max(abs(WavePart))*peakThreshold, 1,
'First');
wfpeak2 = find( abs(WavePart) > max(abs(WavePart))*peakThreshold, 1,
'Last');

wfstart = find( yupper(1:wfpeak1) < max(abs(WavePart))*startThreshold, 1,
'Last')+WavePartStart;
wfend = find( yupper(wfpeak2:length(yupper)) <
max(abs(WavePart))*endThreshold, 1,  'First')+wfpeak2+WavePartStart;
if length(wfend) == 0
    wfend= length(wf);
end
WaveForm = wf(wfstart:wfend);

index = wfstart;
Distance = x(index)*c
```